POLITECNICO DI TORINO

Department of Aerospace and Mechanics Engineering

Master's degree in Aerospace Engineering

Master's Thesis

Innovative Techniques for Spacecraft Separation Assurance and Debris Collision Avoidance

Supervisors:

Roberto Sabatini

Manuela Battipede

Candidate

Federico Cairola

April 2020

Acknowledgement

My sincere thanks go firstly to Prof. R. Sabatini and Prof. M. Battipede for allowing me to attend to this significant international experience.

I'd also especially like to thank Alex Gardi and Sam Hilton for all their patience, their expertise, their precious suggestions and for assisting me in the research of the final project at RMIT University of Melbourne.

Lastly, sincere thanks go to my parents that gave me this opportunity and to my friends for having supported and put up with me in these periods.

Table of Contents

Abstract

This thesis presents a sensor-orientated approach to on-orbit position uncertainty generation and quantification for both ground-based and space-based surveillance applications. A mathematical framework based on the least squares formulation is developed to exploit real-time navigation measurements and tracking observables to provide a sound methodology that supports separation assurance and collision avoidance among Resident Space Objects (RSO). In line with the envisioned Space Situational Awareness (SSA) evolutions, the method aims to represent the navigation and tracking errors in the form of an uncertainty volume that accurately depicts the size, shape, and orientation. Both radar sensor and Passive optical sensor (Coupled Charged Device (CCD)) have been used in order to understand and compare the performance limitations that each sensor present. Simulation case studies are then conducted to verify under which sensors performance the method meets Gaussian assumptions, with a greater view to the implications that uncertainty has on the cyber-physical architecture evolutions and Cognitive Human-Machine Systems required for Space Situational Awareness and the development of a comprehensive Space Traffic Management framework.

1. Introduction

The ever-increasing number of Resident Space Objects (RSO) is strongly highlighting the need for an evolution from traditional Space Situational Awareness (SSA) capabilities towards Space Domain Awareness (SDA) [1, 2]. Analogous to its atmospheric counterpart (i.e., Air Domain Awareness) SDA aims to elevate current SSA capabilities through the dissemination of confidence-building measures, necessary to reliably estimate the future states of RSO's with the aim of optimal coordination and accommodation in a future Space Traffic Management (STM) system. Confidence-building measures ideally encapsulate the functional characteristics of an RSO (e.g., shape and size), and, when possible, mission objectives and planned operational activities of active spacecraft. Even so, an increase alone in the available data will not solve the current issues of RSO ambiguity and collision avoidance subjectivity – contextualizing information must be used together with transparent and traceable Time and Space Position Information (TSPI) reflective of sensor performance. Cooperative RSO equipped with TSPI enabling systems such as GNSS and data sharing capabilities equivalent to Automatic Dependent Surveillance Broadcast (ASD-B) system will be an important aspect in managing uncertainty in the on-orbit environment. Nonetheless, due to the inherently high threat of space debris, it is imperative that the notion of transparent and traceable TSPI information extends to classification of non-cooperative RSOs. In most cases, the position of large orbiting object (>10 cm) can be predicted with reasonable uncertainty, based upon data accrued by the SSA Space Surveillance and Tracking (SST) segment and other non-government owned ground-based sensors (**Table 1**).

Ground-Based System	Devices	Description	Location
AN/FPS-85	UHF Phased-array radar0	Maximum peak power: 30 MW, it can detect 1.0 m^2objects in geosynchronous orbits	Florida, USA
Globus II	X-Band mono-pulse radar with 27m parabolic dish antenna	Track spacecraft of all type up to range of 4,000 Km	Vardo, Norway
ZEISS Telescope	1 m-diameter telescope, FOV of about 0.7º	can detect and track near-GEO objects up to magnitudes of +19 to +21 (down to 10–15 cm in size)	Tenerife, Spain
NASA-LMT	3 m (9.8 ft) aperture liquid-mirror telescope	Detection threshold of 17.5 mag, can detect objects > 3cm at distance of several thousand kilometers	Cloudcroft, New Mexico

Table 1. Overview of Space Surveillance and Tracking (SST) ground-based systems

Although ground-based systems will continue to be a vital aspect in filling the SST role, the feasibility of Space-Based Space Surveillance (SBSS) is being explored to monitor the Low Earth Orbit (LEO) [3] and Geosynchronous Orbit (GEO) regions [4,5], due to the advantage of persistent coverage of smaller sized RSOs (<10cm) elusive to traditional ground-based systems. Understandably spaceborne tracking of RSOs is not a trivial matter [6,7] – effective coverage of the space environment will require constellations of SBS platforms each under

complex tasking regimes to overcome performance and physical constraints [8]. Given that true collisions are a rare space event, the cost of platforms devoted to debris detection may exceed their benefit given that there would be minimal power available for mission-oriented payloads. This is especially the case for spaceborne radar due to the higher power requirements associated with this sensor. For future SBSS platforms to be commercially and economically viable, it is imperative that a low size weight, power, and cost (SWaP-C) approach must be taken. Regardless of the sensor suite chosen, SBSS platforms will be subject to dynamic positional errors from onboard TSPI/Navigation systems, in contrast to traditional ground-based systems that perform observations from accurately surveyed locations. As such, there is a strong case for analysis on the effect of initial RSO position estimation based on both navigation and tracking system errors. Nevertheless, in both ground-based and SBSS applications, a sensor-focused approach must be taken to establish an unambiguous initial estimate of RSO uncertainty.

In the context of SSA, realistic orbital uncertainty directly underpins the effectiveness of operational activities that include the following: RSO Orbit determination, data or track association/correlation, maneuver detection, the computation of the probability of collision for conjunction assessment and sensor management [9,10]. Within the SSA/STM research community, Sensor Management is comprised of Sensor Tasking (ST) and Sensor scheduling (S2). ST is defined as the generation of a set of tasks that a sensor or sensor network is intended to accomplish. On the other hand, Sensor Scheduling (S2) refers to the specific decisions involved in the tasks, to include the exact definition of when and where a sensor is to be used. ST and S2 are typically the constituting elements of an optimal control problem to dynamically assign the available sensor resources (ST) to accomplish specific SSA tasks (S2) [10].

Most importantly, these processes require the knowledge of how the uncertainty of RSOs will propagate over time subject to orbital dynamics and perturbations from residual atmospheric drag, solar radiation pressure, non-spherical Earth, and other celestial bodies. Largely, Orbital uncertainty propagation methodologies can be grouped under either Linear and Non-Linear Methods [11]. Typical Non-Linear methods include Unscented Transformations, Polynomial Chaos Expansions, and Fokker Plank Methods. Undoubtedly, these methods can capture well the non-linear growth of RSO uncertainty subject to orbital dynamics, however, can be computationally burdening due to the high dimensionality of the problem especially for longer propagation periods. The mathematical derivation of these methods is beyond the scope of this thesis, the reader is referred to reference [11]. A popular alternative is to construct a linearized model of the dynamics so that the uncertainty about an RSO can be propagated in a computational efficient manner. However, linearized propagation methods are not without shortcomings -which if not explicitly quantified have significant implications on the realism of subsequent analysis made based on the estimated uncertainty. Uncertainty quantification is defined as follows: *'The process of determining the various sources of errors and uncertainties, properly characterizing these errors and uncertainties, and the roll up of these in the prediction of the quantities of interest"*[10]. In the context of linearized uncertainty propagation methods, two fundamental assumptions are made:

- A linearized model sufficiently approximates the dynamics of neighboring trajectories with respect to a nominal trajectory.
- The uncertainty can be completely characterized by a Gaussian probability distribution.

To quantify the uncertainty, we are interested in testing the uncertainty realism, which under Gaussian assumptions (linear), coincides with covariance realism – the characterization (size, shape, and orientation) of the (gaussian) uncertainty of the RSO in question. Various covariance realism tests and metrics have been used to assess realism with a primary focus on determining the length of Gaussian validity, i.e., the amount of time (commonly described in orbital periods) a linearized uncertainty propagation method can be used to confidently and accurately describe the estimated position uncertainty of an RSO. Nonetheless, by reiteration of the above assumption, linear propagation methods are only valid if the initial RSO uncertainty (input) is in fact Gaussian. This presents the necessary case of applying covariance realism testing to the sensor level with the aim of quantifying tracking and navigation system performance characteristics that support, or not, a linearized (Gaussian) method to describe initial RSO position uncertainty. By taking a sensor level perspective to model tracking and navigation system uncertainty, this thesis addresses three SST representative case studies: a traditional ground-based radar, a proposed Millimetre Wave (MMW) Space-Borne Radar (SBR) and a Space-Based passive Optical Sensor for the tracking of space debris aboard larger spacecraft platforms such as the International Space Station (ISS) and future space transportation vehicles [6,12].

2. Literature review

2.1 History of debris environment

The population of objects in orbit around the Earth has dramatically increased in the past decade. In April 2005, the National Aeronautics and Space Administration (NASA) performed its first collision avoidance maneuver on a robotic spacecraft (Terra satellite). Two years later, the Chinese satellite Fengyun-1C was voluntarily destroyed, causing the largest increase in debris in space history (3,000 objects larger than 10 cm). On February 10th 2009, the collision between operational communication satellite Iridium 33 and retired Russian communication satellite Cosmos 2251 generated 2,000 debris larger than 10 cm and thousands smaller pieces at an altitude of 800 km. The effects of these collision can be observed in the step changes in **Figure 1**.

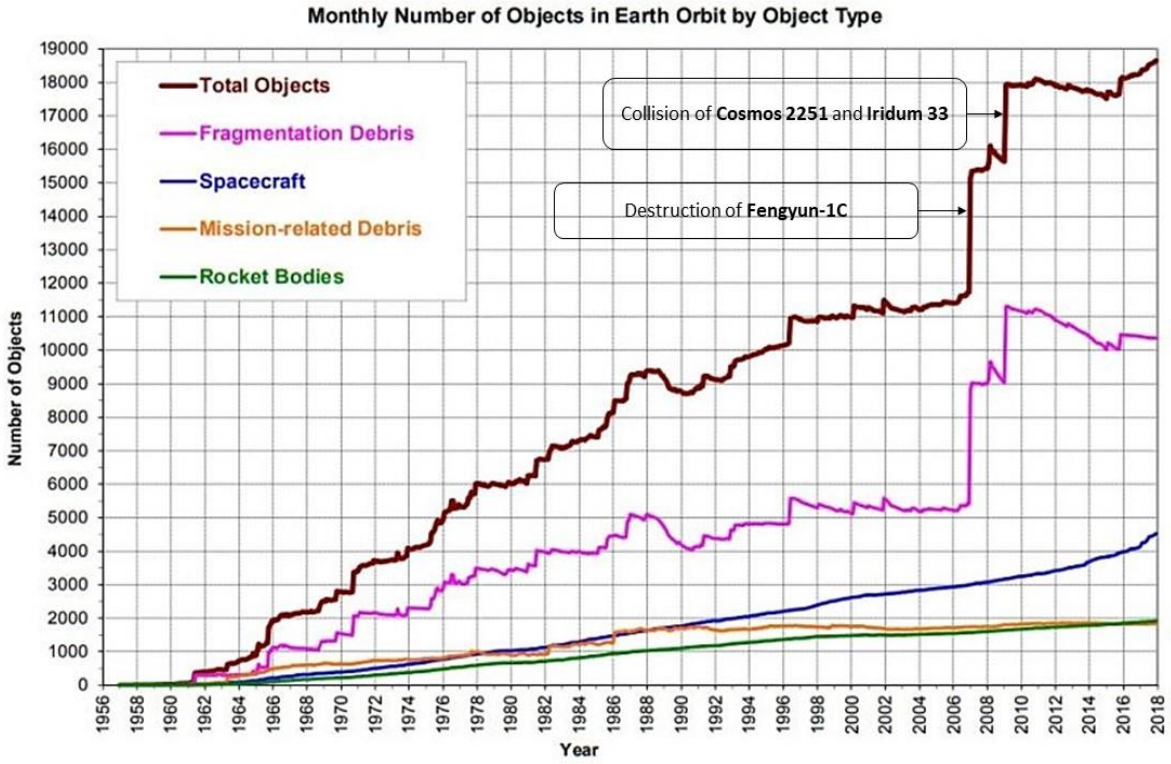

Figure 1: Monthly number of objects in the earth orbit cataloged by the US Space Surveillance Network (SSN), organized by object type

It is now quite common that the International Space Station (ISS) needs to be moved to avoid collisions. In 2015, four collision avoidance maneuvers and one "shelter-in-Soyuz" procedure were performed by the ISS [36, 37]. The "shelter-in-Soyuz" procedure is a safety protocol that requires the three astronauts on-board to seek emergency shelter in the Soyuz capsule, docked to the space station, to prepare for a getaway. ESA astronaut Tim Peake

took a photo, **figure 2**, from inside the International Space Station cupola in 2016, showing a 7 mm-diameter circular chip gouged out by the impact from a tiny piece of space debris, possibly a paint flake or small metal fragment no bigger than a few thousandths of a millimeter across. The background just shows the inky blackness of space.

Figure 2: ESA FONT

Beyond 4 km/s, depending on the materials, an impact will lead to a complete breakup and melting of the projectile, and an ejection of crater material to a depth of typically 2–5 times the diameter of the projectile.
In hypervelocity impacts, the projectile velocity exceeds the speed of sound within the target material. The resulting shockwave that propagates across the material is reflected by the surfaces of the target. The superimposition of progressing and reflected waves can lead to local stress levels that exceed the material's strength, thus causing cracks and the separation of spalls at significant velocities. With decreasing target thickness, the effects will range from cratering, via internal cracks, to spall detachment to, finally, clear-hole perforations.
ESA's space projects use damage assessment tools in combination with debris and meteoroid environment models to predict potential damage from hypervelocity impacts, and to define effective protection measures through shielding and design.
The **figure 3** shows the damage that a spherical object with 1.2 cm diameter causes with an impact velocity of 6.8 km/s on a metallic layer

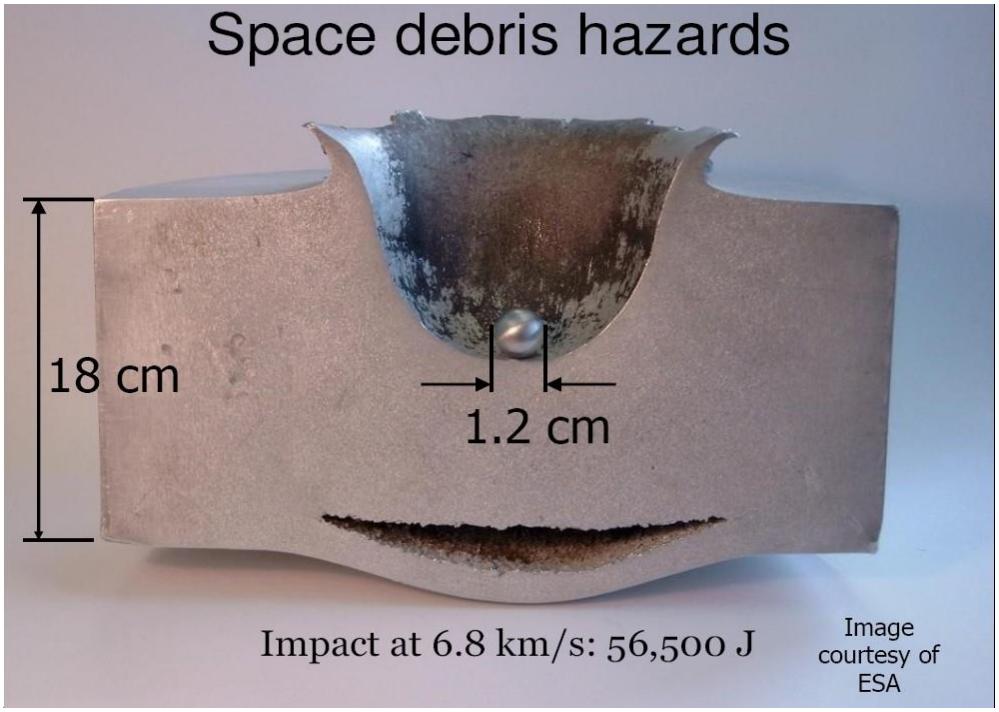

Figure 3: Space debris damage [ESA font]

Space debris environment in number

There are currently 34,000 objects orbiting the Earth that are at least 10 cm wide. Among them, more than 5,000 are spacecraft (1,950 are still operational), 22,300 are number of debris objects regularly tracked by Space Surveillance Network (SSN) and maintained in their catalogue (some of these resulted from the Iridium 33 collision with Cosmos 2251 and the destruction of Fengyun-1C). In addition to these relatively big objects, it is estimated that an extra 900,000 objects larger than 1 cm and 128 million objects larger than 1 mm are in orbit. Even submillimiter objects represent a threat for humans and satellites because of the very high speed that orbiting objects have relative to each other: the average relative velocity of satellites orbiting at a Low Earth Orbit (LEO) is 10 km/s and the average relative velocity of satellites orbiting at the Geosynchronous Earth Orbit (GEO) is 0.5 km/s. The **table 2** shows the number of resident space objects (RSO) updated in February 2020

Type of object	Number of Object
Number of rocket launches since the start of the space age in 1957	About 5560
Number of satellites these rocket launches have placed into Earth orbit	About 5500
Number of these still in space	About 2300
Number of debris object regularly tracked by SSN and maintain in their catalogue	About 22300
Estimated number of break-ups, explosions, collisions or anomalous events resulting in fragmentation	More than 500
Total mass of all space objects in Earth orbit	More than 8800 tonnes
Number of debris objects estimated to be in orbit > 10 cm	34 000
Number of debris objects estimated to be in orbit from 1 cm to 10 cm	900 000
Number of debris objects estimated to be in orbit from 1 mm to 1 cm	128 million

Table 2: Resident Space Object data [ESA, February 2020]

The term Resident Space Object includes different type of object that could be, for example, an operational spacecraft or a rocket body piece or a debris with an unknown origin. The **figure 4** shows the evolutions of the RSO number in all orbit underling the difference own nature, described in **Table 3**.

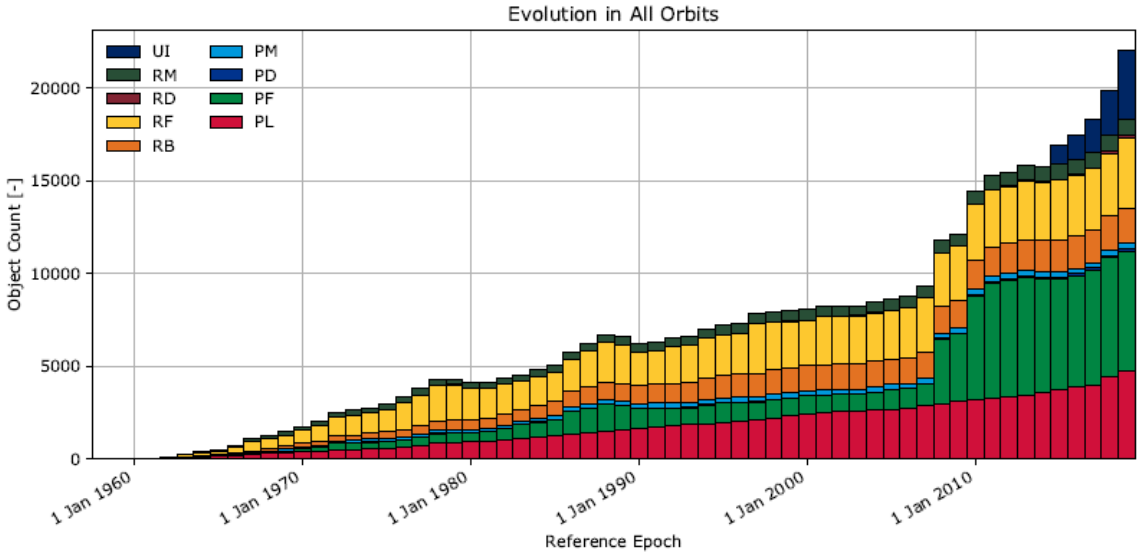

Evolution of number of objects.

Figure 4: Evolution of space environment in term of number and type of RSO

Type	Description
PL	Payload
PF	Payload Fragmentation Debris
PD	Payload Debris
PM	Payload Mission Related Object
RB	Rocket Body
RF	Rocket Fragmentation Debris
RD	Rocket Debris
RM	Rocket Mission Related Object
UI	Unidentified

Table 3: Object Classification

The figure highlights that an important percentage of the number of the RSO derive from a collision.

Collision probabilities with large orbiting objects (>10 cm) can be predicted with reasonable uncertainties, based upon data accrued by SSN and other sensor such the European Space Agency's Optical Ground Station, allowing spacecraft (S/C) to maneuver, reducing the probability of collision. However, the same cannot be said for smaller objects which have less, lower fidelity tracking data, or no tracking data from ground-based sensors. With the

increasing number of small objects in orbit improved debris detection, coupled with predictive modeling is essential to reduce collision probabilities. Collisions with small untracked debris are responsible to cause many anomalies and continuous degradation (e.g. degraded solar cells) of satellites performance.
If we want to express the space debris collision in everyday terms, we can use the kinetic energy equation and we observe that:

- A 2 mm space debris fragment colliding at 10 km/s is like being hit with a cricket ball at 100 km/hour
- A 10 mm fragment at the same speed is like being hit by a large motorbike at 100 km/hour
- A 10 cm RSO fragment at 7 km/s has the same kinetic energy of 6 Kg TNT

Passive techniques, like shielding, are used against smaller debris or against meteoroids that cannot be tracked either [43]. For example, the ISS is shielded to resist debris smaller than 1.4 cm but there are over 1200 objects with diameters greater than 1.4 cm in orbits crossing the ISS orbit and some part of S/C, like solar panels or optical aperture, are hard to shield.
The **figure 5** shows the number of fragmentation events per event cause:

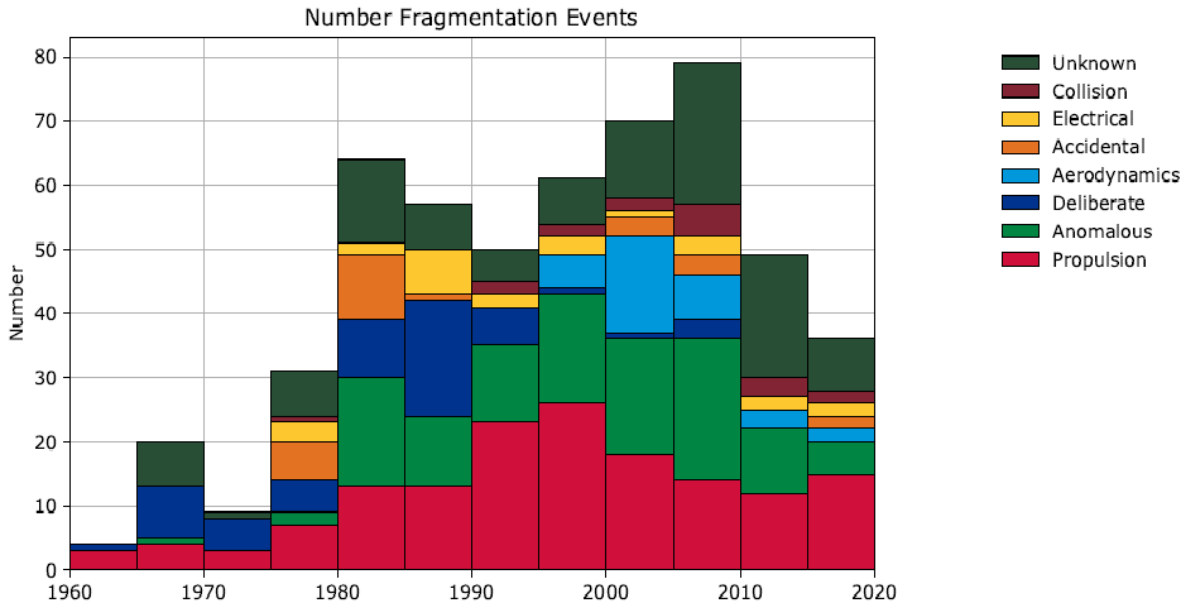

Figure 5: Absolute number of fragmentation event per event cause

A detailed analysis indicates that the predicted catastrophic collisions and the resulting population increase are nonuniform throughout LEO. About 60% of all catastrophic collisions occur between 900-1000 km altitudes. The **figures 6** and **7** underline the concentration of the LEO object in term of Perigee altitude and inclination of the orbit.

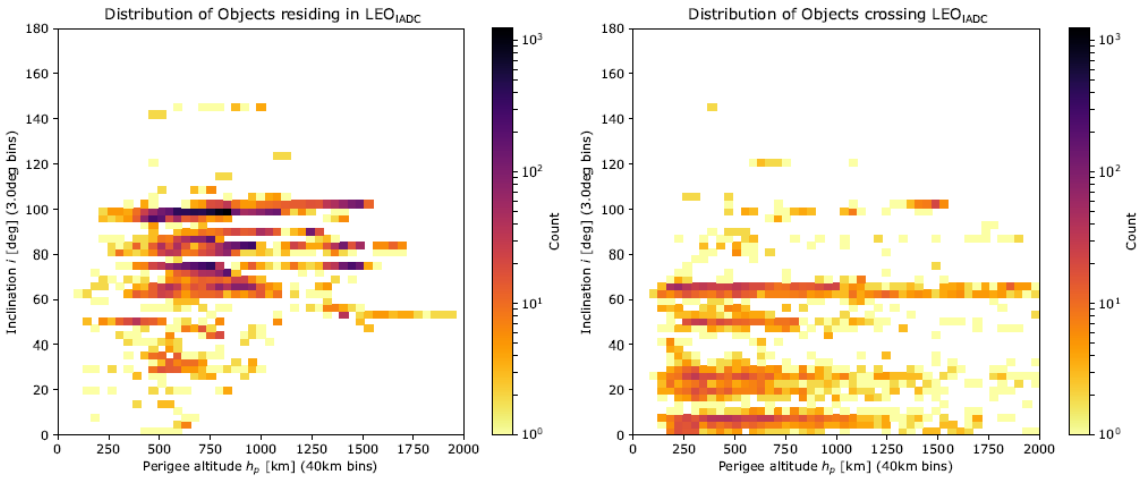

(a) Distribution of objects residing in LEO.

(b) Distribution of objects crossing LEO.

Figure 6: Concentration of RSO in term of Number of objects in LEO

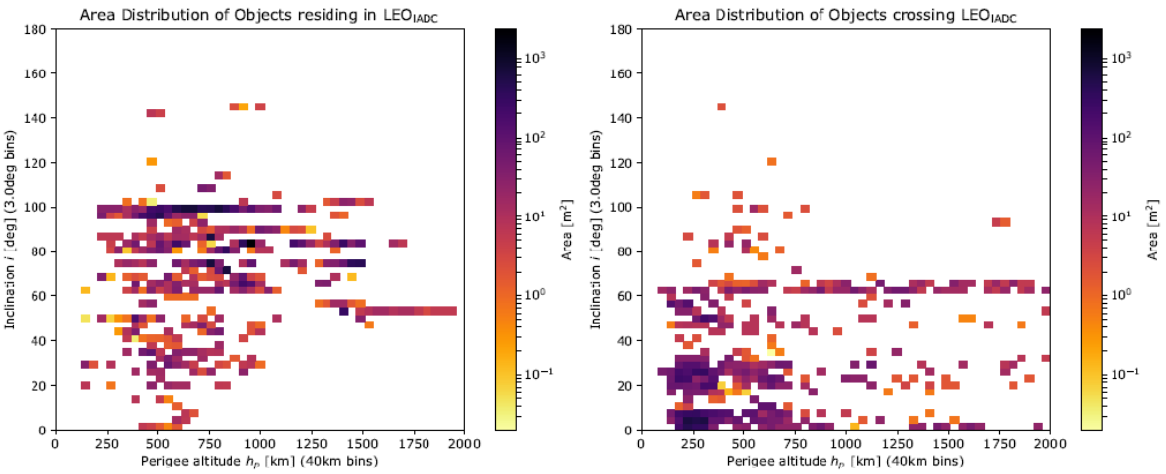

(a) Area distribution of objects residing in LEO.

(b) Area distribution of objects crossing LEO.

Figure 7: Concentration of RSO in term of Area Distribution in LEO

The current debris population in the LEO region has reached the point where the environment is unstable and collisions will become the most dominant debris-generating mechanism in the future. Even without new launches, collisions will continue to occur in the LEO environment over the next 200 years, primarily driven by the high collision activities in the region and will force the debris population to increase, as shown in **figure 8**.

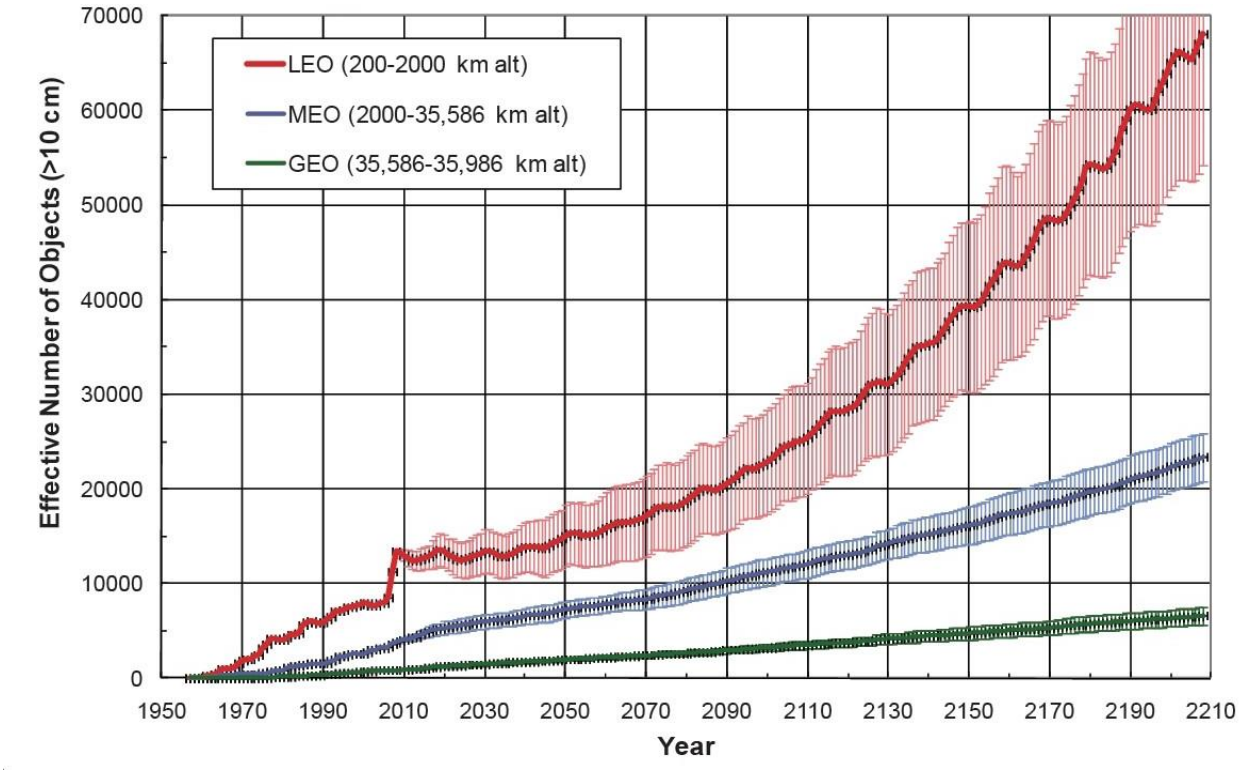

Figure 8: Projected amount of RSO resulting from the Kessler Syndrome if spacecraft is stopped for the next 200 years (Image: NASA)

This population growth is due to higher spatial densities, larger and more massive rocket bodies and spacecraft with near-polar inclinations. The number of objects 10 cm and larger triples in 200 years, leading to a factor of 10 increase in collisional probabilities among objects in this region. In reality, the situation will undoubtedly be worse because spacecraft and their orbital stages will continue to be launched.

Another concern is that debris stay in orbit for a very long time. Due to friction with the atmosphere, debris at relatively low altitude (under 700 km) re-enter the atmosphere, but sometimes only after decades. However, objects at higher altitude, particularly in GEO orbits, never re-enter the atmosphere and therefore, since launches continue, they accumulate with time. The GEO orbit regime is widely used for telecommunications and Earth observations, as well as space science. If no orbit maintenance maneuver is performed on a GEO satellite, gravitational perturbations from the Sun and the Moon make its inclination 2 oscillate around the Equator with an amplitude of 15 degrees. This can pose a threat for operational GEO satellites that orbit at the Equator as the inactive satellites drift back through the GEO belt. A solution is to increase the altitude by a few hundred km at the end of the spacecraft life, moving the satellite into a "graveyard orbit".

The figure shows the evolution of the number of objects since the first satellite was launched in 1957. The **figure 9** shows RSO orbiting not only in LEO and includes also RSO in GEO, underlining where the debris concentration is focus.

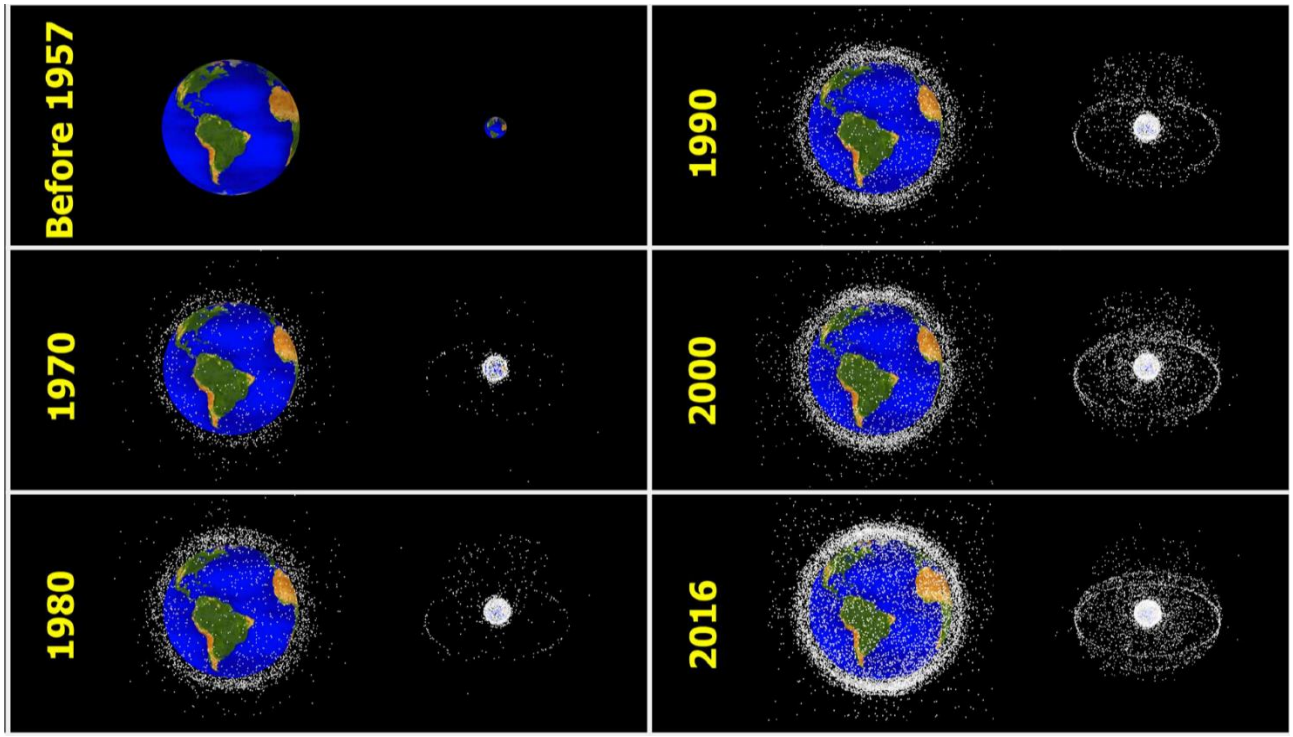

Figure 9: Evolution of the number of tracked objects since the first satellite in orbit in 1957. In each panel, the Earth on the left shows debris in LEO orbits, and the Earth on the right shows debris in GEO orbits

The dots represent space objects in LEO and GEO orbits [36]. Note that only tracked objects cataloged in the Space Surveillance Network are shown, so a large number of small debris (< 10 cm) are not represented. The number of objects has been increasing dramatically over the last few decades: debris keep accumulating in orbit, dangerously increasing the probability of collision with operational satellites. Separation assurance and Collision avoidance requires the knowledge of the position and velocity of all objects in orbit. Occasionally, satellite mission operators can keep track of their satellites with good accuracy using Global Positioning System (GPS) data, but the trajectories of all the other orbiting objects are much harder to follow. For this reason, Space Situational Awareness (SSA) and Space Surveillance Network (SSN) are becoming a primary area of interest for ESA and NASA respectively.

2.2 Space Situational Awareness

The term Space Situational Awareness (SSA) refers to the ability to view, understand and predict the physical location of natural and manmade objects in orbit around the Earth, with the objective of real-time surveillance and collision analysis on a limited basis. SSA has become a prominent concern for both military and commercial systems, largely due to increasing of space assets. Two organizations support the SSA process worldwide: Joint Space Operations Center (JSpOC) and the Space Data Association (SDA). SDA, an international organization of satellite operators working to, in part, enhance the "accuracy and timeliness of collision warning notifications", was established for satellite operators to share the most up-to-date satellite data [44]. JSpOC is currently the single 24/7 global provider used in collision avoidance due to the accuracy and timeliness of the available information [45] and it coordinates the input from various sensor around the world. In order to describe the RSO population (catalogued and not yet catalogued population), mathematical models have been developed, as will be described in **Section 2.2.2**. The SSA system can be divided in two different sub-system, as described in the **figure 10**:

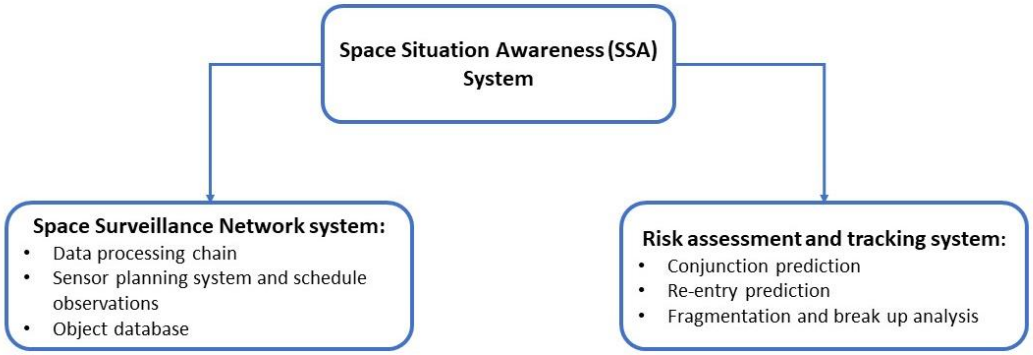

Figure 10: Space Situation Awareness System

As described in the previous figure, effective SSA requires constant surveillance and tracking of the space environment, a task traditionally performed by a network of ground-based observation facilities known as the Space Surveillance Network (SSN), owned and operated by the US Department of Defence (DoD). SSN (and in general all space surveillance systems) have to make the following actions:

- Detects new man-made objects in space
- Produces a running catalog of man-made space objects
- Determines which country is responsible for an orbiting or reentering space object
- Charts the present position of space objects and plots their anticipated trajectories
- Predicts when and where a space object will reenter the Earth's atmosphere

The United States Space Command SSN is composed of ground and space-based sensor systems, as shown in **figure 11**, whose charter is to track human-made resident space

objects. These data are compiled daily into Keplerian element sets and distributed to the user community via NASA Goddard Space Flight Center's Orbital Information Group. All the un-classified spacecraft currently in orbit are cataloged by the United States Space Command in the Two-Line Element (TLE) catalog.

Two Line Elements is a format for distributing orbital elements data considering all objects orbiting around Earth (both operative satellites and debris) cataloged by North American Aerospace Defense (NORAD) Command, a joint organization of Canada and US that provides aerospace warning and air sovereignty. The orbits of the TLE catalogue objects are maintained thanks to the observations performed by the US Space Surveillance Network (SSN). With 75.7%, the vast majority of catalogue objects reside in the LEO region. Another 8.7% of the catalogue objects are in or near the GEO ring. The remainder of the catalogue mainly belongs to the MEO region. The limiting size of the objects included in the catalog (due to limitations in sensors power and in observation and data processing procedures) is about 3 to 10 cm below a few thousands km of altitude and about 0.5 - 1 m in higher orbits (up to the geostationary ones).

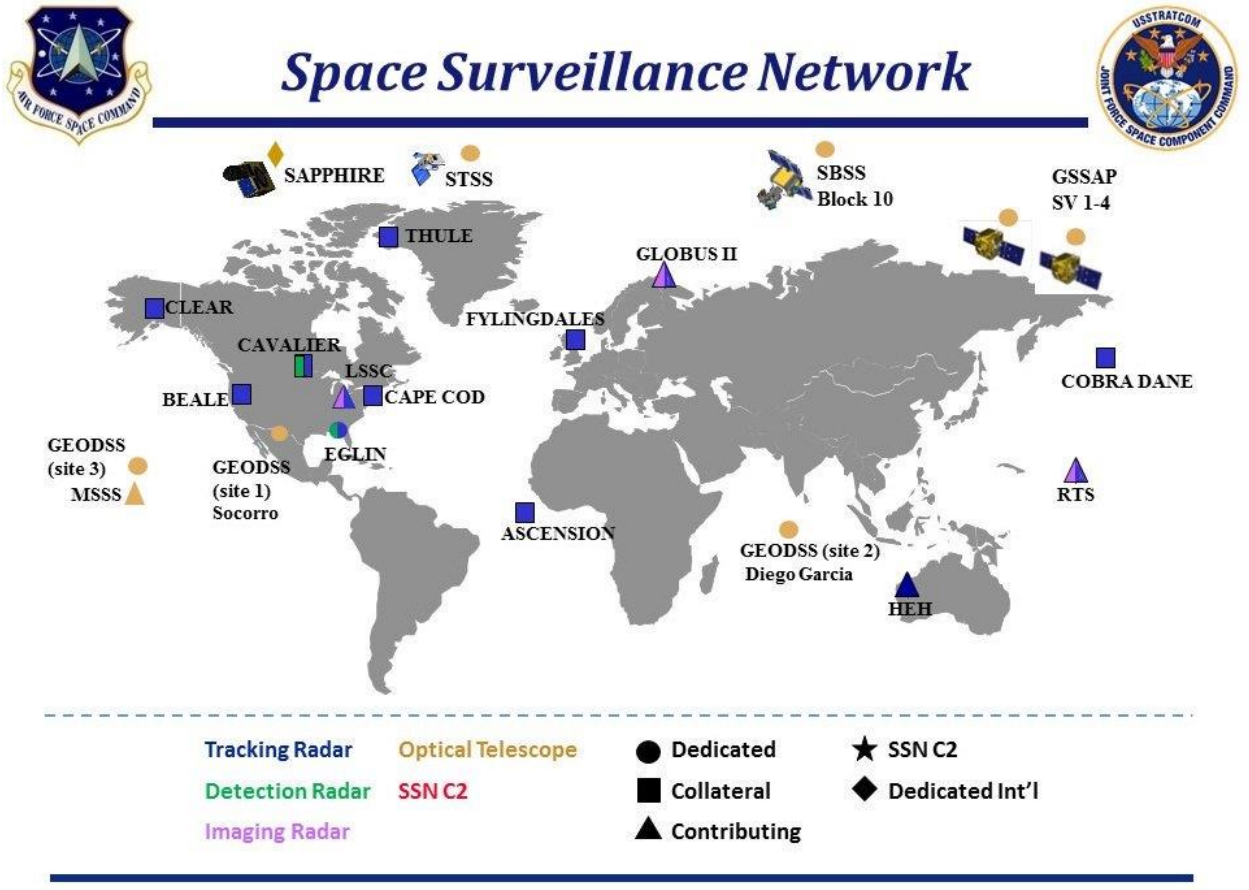

Figure 11: Space Surveillance Network with ground sensors

Albeit, ground based radar, laser and telescope systems will continue to provide a vital role in providing situational awareness of the space environment, however the feasibility of conducting space-borne measurements has been identified [5, 46]. This is credit of onboard

sensors ability to offer greater performances in terms of accuracy, larger field of view and weather independency allowing space-borne measurements to provide a wider set of useful observations [47]. Further, space-based observation systems are not subject to the scattering, diffraction, turbulences and aberrations that exist within the atmosphere [48].
Thus, the strengths of Space-Based Space Surveillance (SBSS) for SSA and space debris observations are:

- Full longitudinal GEO belt coverage with one sensor enabling catalogue generation and maintenance
- Tracking in all orbital regions (LEO, MEO, GTO, Molniya, NEOs) for orbit refinements
- Vicinity to LEO small debris enables in-situ measurements
- No restrictions by weather, atmosphere and day/night cycle, hence operational robustness
- High astrometric accuracy (no atmospheric seeing, diffraction limited design possible)
- No geographical and -political restrictions

The use of radar sensors to provide space-borne measurements has been explored in the past, however due to challenges associated with size & power consumption, there has been a shift in research towards optical based systems. Technological advancements in optical sensor principles (*e.g.* Coupled Charged Device (CCD) [46], complementary metal–oxide–semiconductor (CMOS), photon counting sensors [47,49]) have significantly increased optical detection performance, demonstrating the ability to track a 3 cm diameter object at a 3000 km range [47,50]. Nevertheless, orbital estimation via optical tracking is a difficult task due to the relatively limited field of view the sensors offer and the subsequent extremely short observation arc. To address this problem, the use of multi-spacecraft approach has been proposed [47]. This concept uses a formation of coordinated spacecraft to work in synergy and compile tracking and estimation data to obtain more accurate and complete situational awareness.

2.2.1 SSA at European Space Agency (ESA)

The Space Situational Awareness (SSA) is an initiative of ESA created in 2008 [51]. SSA is defined as a comprehensive knowledge, understanding and maintained awareness of:

- the population of space objects
- the space environment
- the existing threats and risks

As described in reference [71], the overall aim of the SSA is to support the European independent utilization of and access to space for research or services, through providing timely and quality data, information, services regarding the environment, the threats and the sustainable exploitation of the outer space surrounding our planet Earth. While some European optical and radar facilities exist for tracking and imaging space objects, Europe

has no systematic, operational capability for space surveillance, and is therefore strongly dependent on external information, mainly from the US.
The SSA programme will, ultimately, enable Europe to autonomously detect, predict and assess the risk to life and property due to remnant man-made space objects, re-entries, in-orbit explosions and release events, in-orbit collisions, disruption of missions and satellite-based service capabilities, potential impacts of Near Earth Objects, and the effects of space weather phenomena on space and ground-based infrastructure. Space-based systems have become indispensable to many services critical to Europe's economies and governmental functions, including those related to security. Despite of recent progress in implementing space debris mitigation measures [2] the frequency of in-orbit fragmentation events is still significant, as shown in **figure 5**. Studies finds that while considering only those events which resulted in more than 50% of the fragments having an orbital lifetime greater than 20 years, one still obtains a yearly rate of about 3.4 breakups as the average of the last 10 years.
The SSA programme is active in three main areas [51]:

- Space Surveillance and Tracking of objects in Earth orbit (SST): comprising active and inactive satellites, discarded launch stages and fragmentation debris that orbit the Earth.
- Monitoring Space Weather (SWE): comprising particles and radiation coming from the Sun that can affect communications, navigation systems and other networks in space and on the ground
- Watching for Near-Earth Objects (NEO): comprising natural objects that can potentially impact Earth and cause damage and assessing their impact risk and potential mitigation measures

The first aspect, the survey and tracking of space debris in the SSA program, is the context of this thesis. The central aim of SST is to provide an independent ability to acquire prompt and precise information regarding objects orbiting the Earth. Using this data, a wide range of services will be provided, such as warning of potential collisions between these objects or alerting when and where debris re-enters the Earth's atmosphere. This data will be stored in a catalogue, made available to SSA customers across Europe.
SST can be summarized as follows:

- full coverage of LEO (Low-Earth orbit (below 2000 km altitude)), GEO (Geostationary Earth orbit) and near-circular MEO (Medium Earth orbit) orbits
- autonomous build-up and maintenance of a catalogue of all observable space objects
- detection, tracking, orbit determination, target correlation, and physical characterization for objects in LEO, MEO and GEO with a reliability and sensitivity matching the one of the US Space Surveillance Network (SSN)
- estimation of orbit maneuvers
- detection of on-orbit break-up events and correlation with the source object

The SSA-SST Space Surveillance Test and Validation Center (SSTC) is located at ESA/ESAC, Spain. Some main elements are required to ensure that the SST segment can meet critical customer requirements and provide reliable operational services:

- A data catalogue. The core of the SST Segment is the catalogue; this contains information on everything that has been detected in orbit. In order to produce this

catalogue, it is necessary to: reconstruct an orbit from the data that is produced by the sensors (orbit determination); check to see if this object has already been seen and is already in the catalogue (correlation); and monitor the data in the catalogue so that sensors can be tasked to update the information when needed.

- A network of sensors to accurately detect objects orbiting the Earth. These sensors are usually either optical or radar systems. They are divided into two groups: surveillance or tracking.
  a) Surveillance sensors perform the routine task of ensuring that data in the tracking catalogue is accurate and up-to-date. They can observe multiple objects simultaneously and continually add to the quality of the data in the catalogue.
  b) Tracking sensors are used when very high-precision data are needed about a specific object. This happens, for example, if it is predicted that this object will collide with an operational satellite.

2.2.2 Modeling the orbital debris environment

In order to describe the spatial distribution of the debris population (catalogued and not yet catalogued population), mathematical models have been developed. Models are used to take the information obtained by measurements and turn them into useful estimates of the debris population.

As described in reference [71], the idea is to put together as accurate a picture of the past, present, and future environments as possible. Future projections are linked to human activities, launch rates and explosion rates.

Heavy-duty modeling tools have been developed to answer these types of questions. The modeling tools require informations on historical launch and explosion behavior, they propagate debris orbits, describe the orbital behavior of breakup clouds, and compute rates of accidental collisions and their effects on the environment.

Most models take the cataloged population as a basis and add fragments from known breakups in the micron to 50 cm size regime to account for the incompleteness of the catalogue. For sizes larger than 50 cm, the breakup model parameters are calibrated such that the theoretical population fits the catalogued population. For the size range between 1 mm and 50 cm, however, observational data are sparse and the uncertainties in the models increase considerably with decreasing object size. However, validation of the models in the size range from a few millimetres to 50 cm can be achieved with special ground-based measurement campaigns using high performance radar facilities or with space-based measurements. When a new explosion or a new collision happens in the space debris environment, debris models have some problems about their efficiency.

The two more important software tools are the MASTER-2009 (Meteoroid and Space Debris Terrestrial Environment Reference) and NASA Orbital Debris Engineering Model (ORDEM 2010), respectively the ESA and NASA reference software tools which describe the earth's debris environment.

2.3 Uncertainty in the orbital environment

The precise knowledge of a RSO's position and velocity is and will continue to be an increasingly important factor for the future space traffic management programs. These estimations are provided by non-cooperative and cooperative systems. Cooperative systems rely on state estimates from on-board navigation systems (e.g. GNSS, IMU) and on their proactive exchange with all other vehicles in potential collision course. Non-cooperative surveillance is generally provided by tracking systems such as ground- and space-based radar or electro-optical systems, which do not require response by the tracked object. These systems are subject to errors that are a function of physical phenomenon or from the mathematical extrapolation itself. Navigation and tracking errors are the differences between the measured states and the actual states of the space vehicle. Also attitude and timing error are relevant but at this stage they won't consider. Errors can particularly arise from either within the reference coordinate system, from effects such as precession and polar motion or from errors specific to the position measurement such as clock accuracy, and atmospheric effects (ionospheric and tropospheric refraction) [11]. Every sensor has, therefore, an accuracy and this lead to have a measurement error that affects the sensor performance. **Tables 4 – 8** illustrate the performance of common spacecraft navigation and ground tracking related systems.

Spaceborne attitude sensor(s) performance	Accuracy [mrad]	Limitations
Sun Sensor	0.2-200	
Star Tracker	0.005-0.3	Angular Rotation, Sun, Earth and Moon stray light
Earth Horizon Sensor	1-20	Accuracy is limited by the horizon uncertainty. Applicable to LEO spacecraft

Table 4: Spaceborne attitude sensors(s) performance

Spaceborne Inertial Sensors	Accuracy	Limitations
Single-axis gyroscope	Angular random walk: 0.035–1 [μ rads /s]	Subject to short and long term bias instability
Linear accelerometer	20–400 μm/s2	Subject to short and long term bias instability

Table 5: Spaceborne inertial Sensor(s) performance

GNSS Sensor	Accuracy (3σ)		
	Radial (R)	In- Track (S)	Cross Track (W)
GPS	20 m	13 m	7.3 m

Table 6: Reference spaceborne GNSS performance

Ground Station Radar	Min. size range Threshold	Altitude Range (Km)
Haystack (US)	1 cm	350 to 2000
HAX (US)	1 cm	350 to 2000
Goldstone (US)	2 mm to 2 cm	300 to 3200
Cobra Dane (US)	4 cm	500 to 2300
Tira (ESA)	1 cm	1000
EISCAT (ESA)	2 cm	500 to 1500
Graves (ESA)	10 cm	LEO

Table 7. Characteristics of the important radar in the world

Telescope	Min size range / magnitude threshold	Region of survey
LMT (US)	1-5 cm / 24 mag	LEO
Zimerwald (ESA)	19 mag	GEO
MCAT (US)	1 cm	LEO
Tenerife (ESA)	10-20 cm / 21 mag	GEO

Table 8. Characteristics of the important telescope in the world

Representation of measurement errors is a key aspect in current orbital coordination and deconfliction operations.

Moreover, modelling errors occur from discrepancies in the orbital dynamic model. Errors included in the dynamic model are classified as the differences between the nominal model parameters and the real model parameters, which can be further categorized as rather gravitational or non-gravitational in nature:

- gravitational parameters include mass of the Earth, geopotential coefficients, solid Earth and ocean tide perturbations, mass and position of the Moon and planets, as well as general relativistic perturbations.
- Drag (due to atmospheric density), solar and Earth radiation pressure, magnetic perturbations and spacecraft thrusting (actuating errors) are the non-gravitational accelerations required for consideration in orbital modelling [11]

The general analytical expressions for these perturbations will provide in **Section 2.5**.

To understand and analyze the RSO position in an inertial reference frame it will be necessary relate different type of measurement error, as described in the following section

2.3.1 Unified sensor-centric approach

Considering the prospective certification requirements for non-segregated Unmanned Aircraft Systems (UAS) operations in all classes of airspace, an unified approach for multi-platform Separation Assurance (SA) and Sense and Avoid (SAA) was proposed [53]. This computationally inexpensive method allows to efficiently and effectively combine the measurement errors related to various navigation and tracking systems and to determine a combined avoidance volume that's position, shape, size and evolution can be computed in real-time [53]. As described in Ref. [73], The unified approach accounts for navigation and tracking measurements as well as relative dynamics and maneuvrability and can adapt to both cooperative and non-cooperative encounters by considering the position, velocity and attitude uncertainties of both tracked and host platforms as well as their statistical correlation:

- A non-cooperative scenario in the orbital environment is defined as the encounter between a host spacecraft and space debris or potentially an uncooperative spacecraft (tracked by non-cooperative means), where only the host spacecraft has the ability to prevent a potential collision.
- A cooperative scenario is defined as when all potentially colliding RSO have the means to exchange position information and when possible perform de-confliction maneuvers.

This sensor-centric approach has clear applicability to the orbital domain, where deconfliction processes have long relied on a simplified representation of measurement uncertainty.
In this thesis only a non-cooperative scenario will be analyzed by using, first, a Millimetre Wave (MMW) Space-Borne Radar (SBR) and then a passive Optical Space-Based Surveillance multi-platform system

2.4 Study of accuracy sensors

This thesis will be focus on analyze the sensor performance such as radar and electro optical sensors. As described before, it is necessary create an error model for analyze the sensor performance that will allow us to quantify the RSO position uncertainty.

2.4.1 Radar Error Model

The SNR (Signal to Noise Ratio) of the radar is a key measure of its performance, which is defined as the ratio of signal power to noise power at the output of the radar receiver.

$$SNR = \frac{P_r}{P_n} = \frac{PG_t\sigma A_r\tau}{(4\pi)^2 R^4 kFT_0 L} \quad (1)$$

Where:
G_t: Radar transmit antenna gain (power ratio)
P: Peak transmitted power [W]
A_r: Radar receive antenna effective aperture area [m^2]
σ: Target radar cross-section (RCS) [m^2]
R: Range from radar to target [m]
F: Noise figure of the receiver subsystem
L: Radar system losses
T_0: Standard Temperature [290 K]
k: Boltzmann's constant [$1.38064852 \times 10^{-23}\ m^2\text{Kg}\ s^{-2}K^{-1}$]
τ: Radar pulse duration [sec]
Target state vector information is measured relative to the radar site in a spherical coordinate system in range, elevation and azimuth ($r_{RDR}, \eta_{RDR}, \epsilon_{RDR}$ respectively). The measurements in each of the elements are prone to specific error sources that include the following [27]:

$${\sigma_{r_{RDR}}}^2 = \sigma_{RN}^2 + \sigma_{RF}^2 + \sigma_{RB}^2 \quad (2)$$

where σ_{RN} is an SNR dependent random range measurement error, which can be calculated as:

$$\sigma_{RN} = \frac{c}{2B\sqrt{2(\text{SNR})}} \quad (3)$$

Where: B is waveform bandwidth, c is the speed of light and signal to noise ratio (SNR). σ_{RF} is a random measurement error having fixed standard deviation, due to noise sources in the latter stages of the radar receiver. σ_{RB} is a range bias error associated with the radar calibration and measurement process. We assume the Zero-mean condition, so. σ_{RB} and σ_{RF} are equal to zero.
Radar angular measurements are commonly made using monopulse receive antennas that provide a difference pattern characterized by a deep null on boresight. The difference pattern formed by these beams may be used to measure target angular position with a single signal transmission. The measurement accuracy in each angular coordinate is characterized by the RMS of the SNR dependent random angular measurement error, angular bias, and

random measurement error. As with the range error, we assume angular bias and random measurement error to be 0 under the Zero-mean condition

$$\sigma_{\epsilon_{RDR}}{}^2 = \sigma_{AN_\epsilon}^2 + \sigma_{AF_\epsilon}^2 + \sigma_{AB_\epsilon}^2 \quad (4)$$

$$\sigma_{\eta_{RDR}}{}^2 = \sigma_{AN_\eta}^2 + \sigma_{AF_\eta}^2 + \sigma_{AB_\eta}^2 \quad (5)$$

As with the range errors, the SNR dependent error dominates the radar angle error:

$$\sigma_{AN} = \frac{\vartheta}{k_m\sqrt{2(SNR)}} \quad (6)$$

Where: ϑ is the radar beamwidth in the angular coordinates and k_m is the monopulse pattern difference slope.

2.4.2 Passive Optical Sensor Error Model

The utilization of radar technology has been proposed in the past. Its on-board implementation requires considerable expenditure in terms of power consumption, spacecraft size and mass with limited benefits in terms of performance [38]. Therefore, the utilization of optical sensors appears to be a viable solution for this kind of missions. Such sensors can use different working principles (CCD, CMOS or photon counting sensors [39]) and their accuracy on the debris detection is currently improving thanks to recent advancements. Other studies show that the debris detection is also possible by exploiting Star Tracker (ST) [40]. The use of STs is passive: the incoming solar radiation is reflected by debris particles back to space to be recorded by optical system. As shown in **figure 12**, RSO will appear as tracks in images and it can easily be identified against point-like stars.

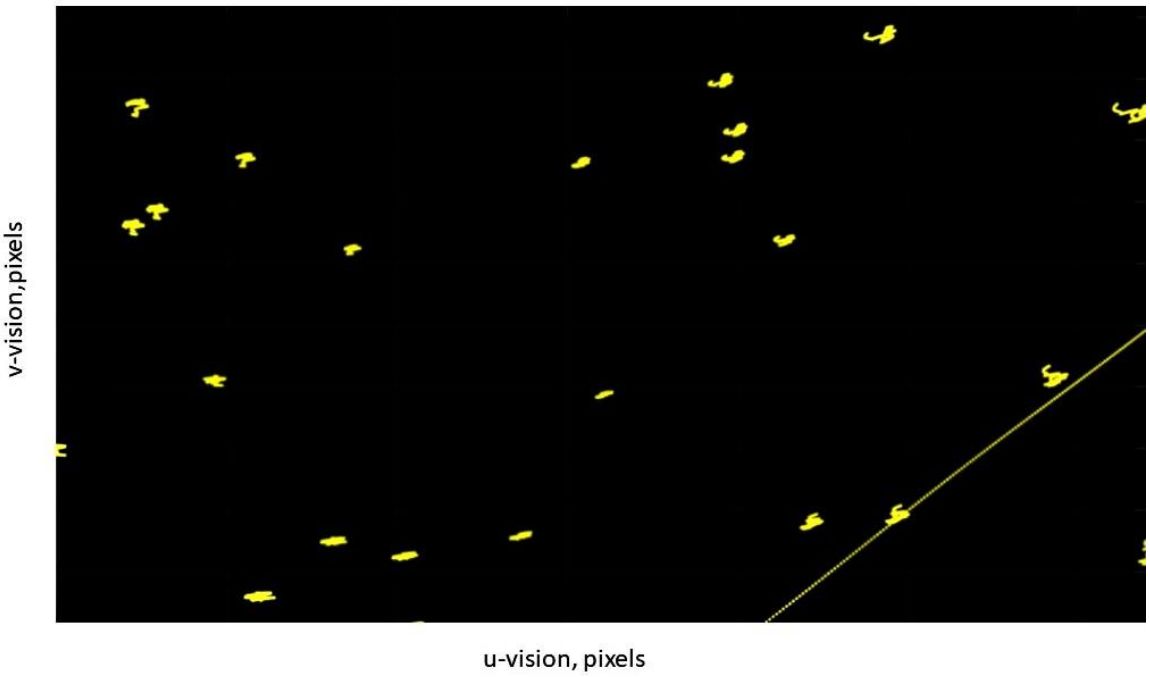

Figure 12: Camera view of the stars background and the streak due to the debris motion

A fixed background of stars is used as a reference coordinate system for detecting the relative motion of space debris by using either long exposure shot or multiple shot by the camera. It is worth noting that the main prerequisite for allowing this kind of detection is to maintain the orientation of the camera subsystem. The onboard camera is modeled using the central-projection model. **Figure 13** shows the camera coordinate frame, the real and the projected points into the image plane, which is located at a focal distance f far from the camera origin.

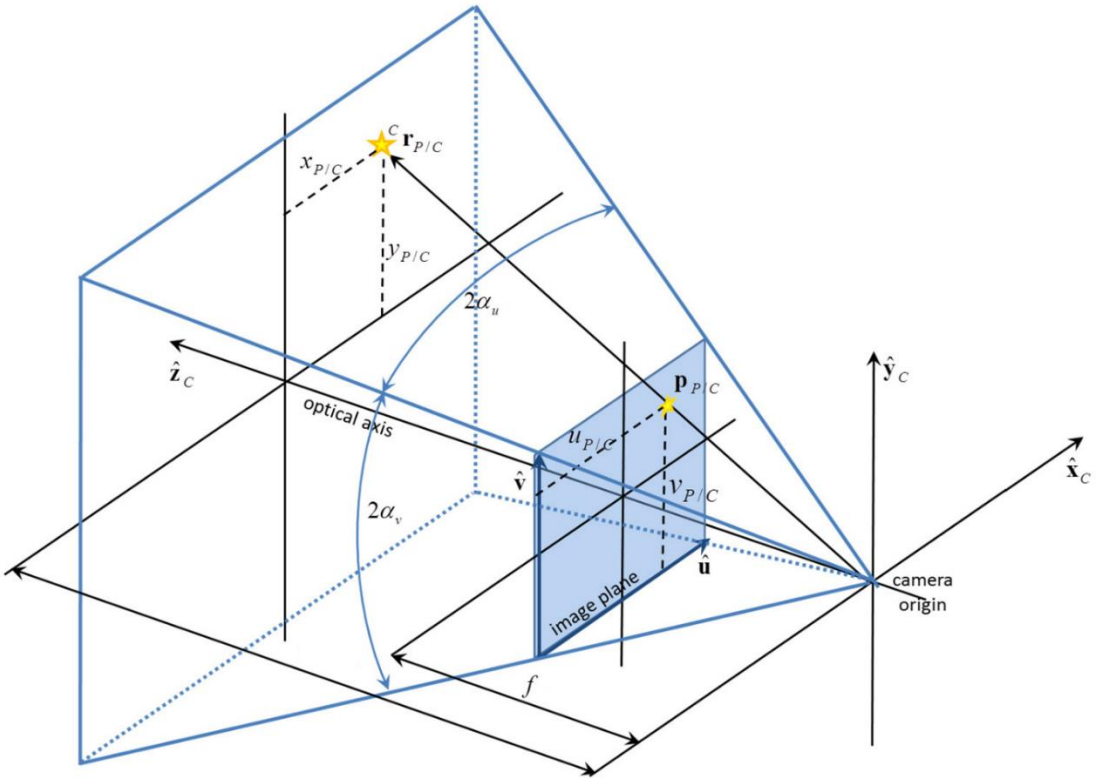

Figure 13: Camera coordinate frame, image plane and image formation geometry

The number of pixels of the image plane depends on the characteristics of the camera system, and they are expressed in terms of N_u x N_v number of pixels. This implies that an object will be visible only if it is inside the field of view of the camera. Defined by the two angles:

$$\alpha_u = \frac{N_u \rho_u}{2\,f}$$
$$\alpha_v = \frac{N_v \rho_v}{2\,f} \qquad (7)$$

Where ρ_u and ρ_v are the width and the height of each pixel.

Optical sensor properties

The radar technology is characterized by decreasing of the signal which is function of the inverse of the fourth power of the distance. The optical observations have an advantage on radar observations because the signal to noise ratio (SNR) for an optical observation is proportional to:

$$SNR \approx \frac{a^2 D^2}{R^2} \tag{8}$$

Where a is the diameter of the object, D is the diameter of the photo collecting area in the telescope and R is the sensor-debris distance (range). This means that the minimum observable diameter a is the inversely proportional to the range, for the same diameter D of the telescope.

Hence, a key parameter is the minimum size of detectable RSO a_{min} [57] determined by:

$$a_{min} = \left[\frac{4hc\sigma RFv}{q\eta\lambda\mu\pi\alpha D P_0}\right]^{1/2} \tag{9}$$

Where:

h=6.63x10^{-34} J is the Planck's constant, **c**= 3x10^8 m/s is the speed of light, $\boldsymbol{\eta}$ is the quantum efficiency, $\boldsymbol{\lambda}$ is the wavelength, **q** is the A/D conversion factor, **R** is the range, $\boldsymbol{\alpha}$ is the albedo, $\boldsymbol{P_0} \approx 1400\, W/m^2$ is the solar constant, **D** is the lens diameter, **F** is the focal length of the lens, $\boldsymbol{v}$ is the RSOs relative velocity projected into the array plane, $\boldsymbol{\sigma}$ is the noise of the detector and **μ** is the CCD array pixel size.

Figure 14 shows the results of the calculating maximum detectable RSO size as a function of the particle velocity v and the range R. Calculations were carried out for Star Tracker having the following characteristics:

D =70 mm, **F** = 40 mm, **μ** = 13.5 μm

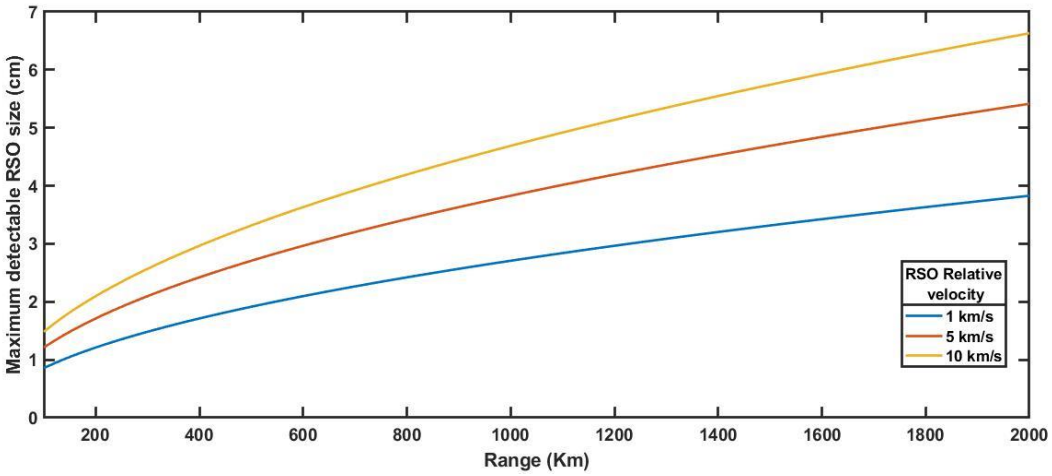

Figure 14: Maximum detectable RSO size vs Range

It is fundamental to understand SSA requirements in order to find what parameters are more important and develop some observation strategies.

RSO observations by using optical sensor have also other limitations:

- RSO that are in the Earth's shadow cannot be seen by the sensor. The illumination of an object is determined by whether or not it is in the Earth's shadow. Given the sun vector **s** and **r** the vector position of the object, two conditions have to be satisfied:

$$\mathbf{r} \cdot \mathbf{s} > \mathbf{0}$$
$$\| \mathbf{s} \, x \, \mathbf{r} \| \leq R_e \tag{10}$$

Where R_e is the radius of the Earth

- The RSO brightness is a key element to define whether or no the object will be observable by optical sensor. The visual magnitude of RSOs (M_v) behave different from stellar objects and change in intensity with changes in RSO attitude and observing geometry. As shown in **figure 15**, the phase angle ϕ, defined as the angle between the vector from the observer to the RSO and the RSO's Sun vector, is responsible for large changes in the apparent visual magnitude of an RSO.

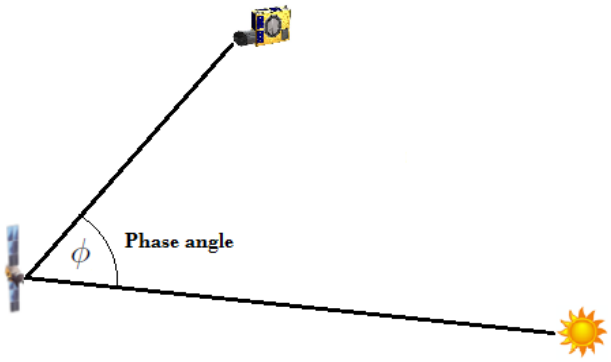

Figure 15: Solar phase angle defined [63]

The phase function F(ϕ) is given by:

$$\mathrm{F}(\phi) = \frac{2}{3\pi^2}[(\pi - \phi)cos(\phi) + sin(\phi)] \tag{11}$$

Assuming a spherical RSO, the visual magnitude can be estimated by [63]:

$$M_v = M_{Sun} - 2.5 \log_{10}\left(\frac{\rho A \mathrm{F}(\phi)}{R^2}\right) \tag{12}$$

Where: M_{Sun}= -26.74, ϱ is the albedo of the object, A is the cross-sectional area and R is the range.

Figure 16 shows how the visual magnitude of an RSO varies as a function of its phase angle. This relationship is approximately linear. As no direct model is available for either a given RSO's attitude or its reflectivity then, in general, an RSO is brightest when the phase angle is at minimum. In this configuration a maximal amount of sunlight is then reflected to the observer.

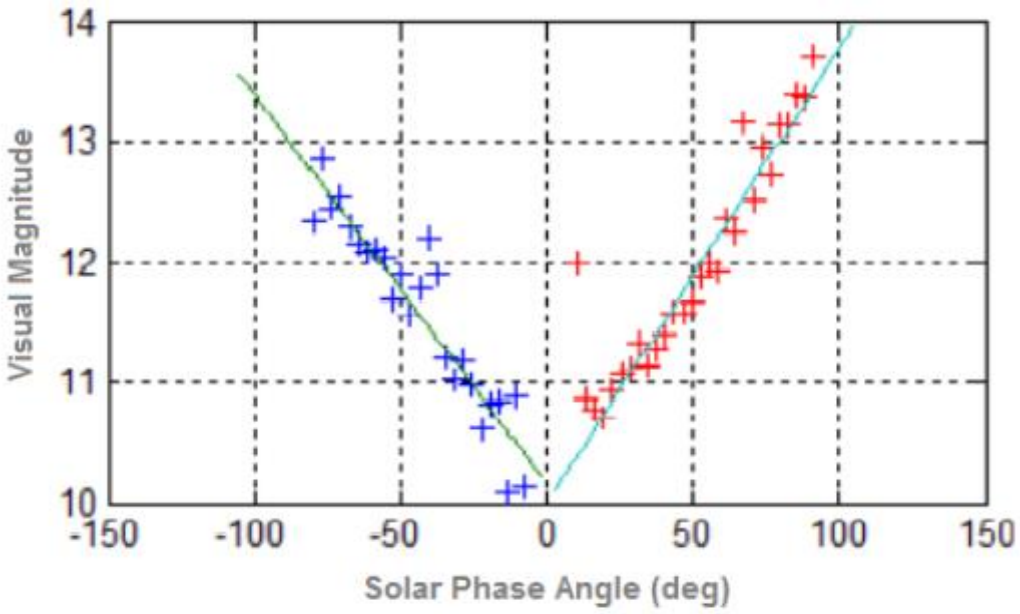

Figure 16: Visual Magnitude vs Solar Phase Angle (ϕ) [63]

The SNR equation, using the visual magnitude, can be written as:

$$SNR = 1.274 \frac{10^{10-M_v}}{\sqrt{1.274\ x\ 10^{10-M_v}\ +\ 817.772\ x\ N}} \quad (13)$$

Where N is the noise (intended as the sum of the different source contributions)

The SNR values characterizes the quality of a measurement and determines the ultimate performance of the system

- The size of debris must be fit with the detecting capacity of the telescope. We need to compare the real size of the object and the limiting size of debris that the telescope can be detect.

Errors and noise

The existence of errors and noise in the system are inevitable. The sources of error in tracking can be divided into two primary classes: static and dynamics errors. The first class covers all errors related to static measurement, which includes errors occurring while using the tracking system in a static way and errors during calibrating the system. In contrast to static errors, dynamic errors are caused by end-to-end system delays when parts of the tracking system are moving. Dynamics errors are not covered by this thesis. The class of static errors can again be split into two different groups of errors [69, 70]:

- *Systematic errors*, also called *biased* errors, are repeatable which means when doing the same measurement several times the error will remain the same
- *Random noise*, this type of error is not repeatable. Noise in sensor input is inevitable with any measurement system. For this reason, noise cannot be corrected with calibration, but their effect can be reduced. For example, readout noise of the sensor can be reduced by selecting the appropriate mode of operation of the device reading out with a lower frequency.

2.4.2.1 Error Model of Systematic Errors

The factors that affect the results of the RSO tracking include the position error of principal point, error of focal length, inclination of the image plane and lens distortion. Therefore, it is necessary to establish a calibration model for above the parameter errors and analyze error model [64]. Doing this, we will use a Star Tracker model as passive optical sensor.
The optical system of the star tracker is presented in **Figure 17**. The Star Tracker is a high-accuracy attitude measurement device, but it can be used for RSO tracking and detection. $OX_SY_SZ_S$ denotes the Star Tracker coordinate system without the image plane displacement error.

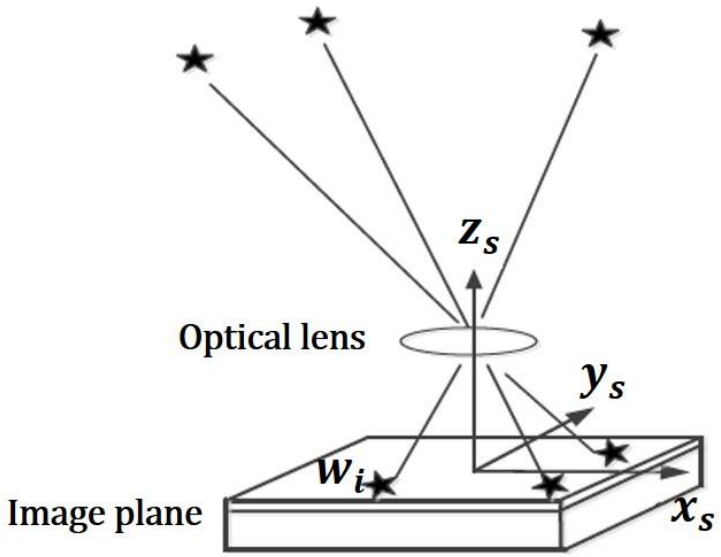

Figure 17: Star Tracker Ideal Imaging Model

For any Star/RSO image point (x_d, y_d) in the image plane exist a direction vector in the inertial coordinate system I that can be expressed as:

$$\boldsymbol{V_i} = \begin{bmatrix} cos\alpha\ cos\delta \\ sin\alpha\ cos\delta \\ sin\delta \end{bmatrix} = \begin{bmatrix} v_1 \\ v_2 \\ v_3 \end{bmatrix} \tag{14}$$

Where α and δ are the azimuth and elevation angles
The temperature difference in orbit will generate displacement errors and distortion of the optical system. The displacement errors mainly include the principal point drift, rotation and tilt. The schematic diagram of the image plane is shown in **figure 18**. $O''X_dY_dZ_d$ denotes the optical sensor coordinate system with the main point drift, the focal length error and the image plane tilt-rotary error, and (x_d, y_d) denotes the RSO image point in the plane $O''X_dY_dZ_d$.

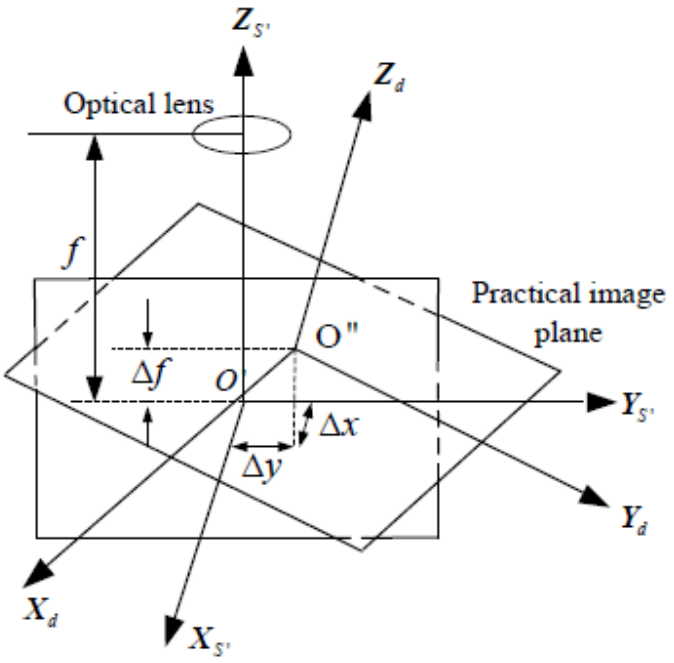

Figure 18: The diagram of the image plane displacement error

The rotation angles of $O''X_dY_dZ_d$ relative to $O'X_{s'}Y_{s'}Z_{s'}$ are successively φ, θ and ψ. These angles denote the image-plane rotary and tilt angles of the optical system. $C_{O'O''}$ denote the attitude transformation matrix:

$$C_{O'O''} = \begin{bmatrix} cos\theta cos\varphi - sin\theta sin\psi sin\varphi & cos\psi cos\varphi + sin\theta cos\psi sin\varphi & -cos\theta sin\varphi \\ -cos\theta sin\psi & cos\theta cos\psi & sin\theta \\ cos\theta cos\varphi - sin\theta sin\psi sin\varphi & cos\theta cos\varphi - sin\theta sin\psi sin\varphi & cos\theta cos\varphi \end{bmatrix} \quad (15)$$

Lens distortion

Lens distortion are also one of the main measurement errors of star tracker sensors. The common distortion model is the Brown-Conrady model proposed by Brown in 1966 [68]. As shown in **figure 19**, the model is divided into the radial and tangential distortion.

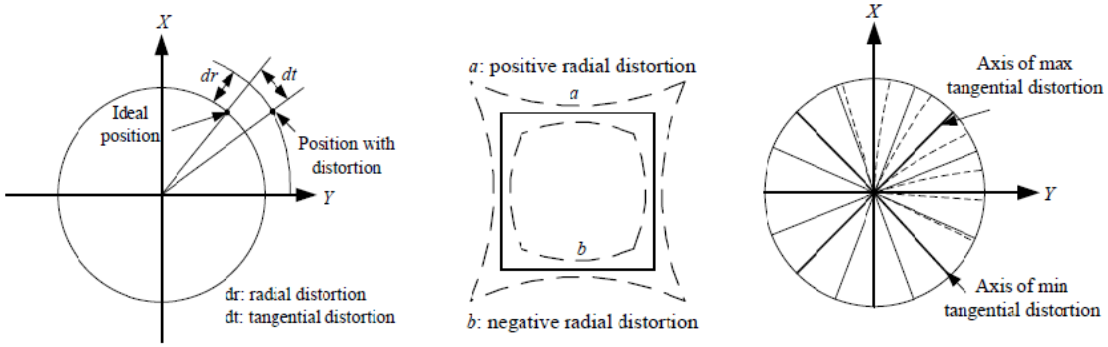

Figure 19: (a) Radial and tangential distortions; (b) Effect of radial distortion; (c) Effect of tangential distortion [64].

The relationship between the imaging point with the distortion and without the distortion can be expressed as:

$$\begin{aligned} x_d &= x'_d - \delta_{x_d}(\hat{x}_d, \hat{y}_d) \\ y_d &= y'_d - \delta_{y_d}(\hat{x}_d, \hat{y}_d) \end{aligned} \tag{16}$$

(x'_d, y'_d) denote the actual measurement coordinates of the RSO image point, and $(x_d\ , y_d\ )$ denote the coordinates without the optical system distortions. $(\delta_{x_d},\ \delta_{y_d})$ denote the combination of the radial and the tangential distortion model and can be estimated by $(\hat{x}_d, \hat{y}_d)$ that are the estimated values of (x_d, y_d). For doing this, the assumption that the image plane without lens distortion is similar to the plane with lens distortion is necessary.

Thus, δ_{x_d} and δ_{y_d} can be written as:

$$\begin{aligned} \delta_{\hat{x}_d}(\hat{x}_d, \hat{y}_d) &= 3\mu_1 {\hat{x}_d}^2 + 2\mu_2 \hat{x}_d \hat{y}_d + \mu_1 {\hat{y}_d}^2 + \lambda_1 \hat{x}_d({\hat{x}_d}^2 + {\hat{y}_d}^2) \\ \delta_{\hat{y}_d}(\hat{x}_d, \hat{y}_d) &= 3\mu_2 {\hat{x}_d}^2 + 2\mu_1 \hat{x}_d \hat{y}_d + \mu_2 {\hat{y}_d}^2 + \lambda_1 \hat{y}_d({\hat{x}_d}^2 + {\hat{y}_d}^2) \end{aligned} \tag{17}$$

Where: μ_1, μ_2 are the tangential distortion coefficient, λ_1 is the radial distortion coefficient, $(\hat{x}_d, \hat{y}_d)$ are the estimated values of (x_d, y_d).

According to the previous analysis, the following equation is obtained:

$$\boldsymbol{V_i} = C_{IO'} C_{O'O''} \frac{1}{\sqrt{\left(x'_d - \delta_{\hat{x}_d} - \Delta x\right)^2 + \left(y'_d - \delta_{\hat{y}_d} - \Delta y\right)^2 + (f + \Delta f)^2}} \begin{bmatrix} -(x'_d - \delta_{\hat{x}_d} - \Delta x) \\ -(y'_d - \delta_{\hat{y}_d} - \Delta y) \\ f + \Delta f \end{bmatrix} \tag{18}$$

Let: $C_{IO'} C_{O'O''} = \begin{bmatrix} c_{11} & c_{12} & c_{13} \\ c_{21} & c_{22} & c_{23} \\ c_{31} & c_{32} & c_{33} \end{bmatrix}$

$\boldsymbol{V_i}$ denotes the object direction vector in the inertial coordinate system, C_{IO}, is the attitude transformation matrix where I is the Inertial reference frame.

According to **equations 17** and **18**, we obtain Equation:

$$\begin{aligned} \mathrm{x}'_\mathrm{d} &= -(f + \Delta f).\frac{\mathrm{c}_{11}v_1 + \mathrm{c}_{12}v_2 + \mathrm{c}_{13}v_3}{\mathrm{c}_{31}v_1 + \mathrm{c}_{32}v_2 + \mathrm{c}_{33}v_3} + 3\mu_1 {\hat{x}_d}^2 + 2\mu_2 \hat{x}_d \hat{y}_d + \mu_1 {\hat{y}_d}^2 + \lambda_1 \hat{x}_d\left({\hat{x}_d}^2 + {\hat{y}_d}^2\right) + \Delta x \\ \mathrm{y}'_\mathrm{d} &= -(f + \Delta f).\frac{\mathrm{c}_{21}v_1 + \mathrm{c}_{22}v_2 + \mathrm{c}_{23}v_3}{\mathrm{c}_{31}v_1 + \mathrm{c}_{32}v_2 + \mathrm{c}_{33}v_3} + 3\mu_2 {\hat{x}_d}^2 + 2\mu_1 \hat{x}_d \hat{y}_d + \mu_2 {\hat{y}_d}^2 + \lambda_1 \hat{y}_d({\hat{x}_d}^2 + {\hat{y}_d}^2) + \Delta y \end{aligned} \tag{19}$$

Equation 19 is the systematic error model which is related to $\Delta x,\ \Delta y,\ \Delta f, \lambda_1, \mu_1, \mu_2,$ $\mathrm{c}_{11}, \mathrm{c}_{12}, \mathrm{c}_{13}, \mathrm{c}_{21}, \mathrm{c}_{22}, \mathrm{c}_{23}, \mathrm{c}_{31}, \mathrm{c}_{32}, \mathrm{c}_{33}$.

2.4.2.2 Random Noise

In sense of tracking this will cause randomly changing gray values in the image plane, which then causes errors in estimation of the 2D position of the object which then again cause errors when solving the 2D-to-3D pose estimation problem. The line-of-sight (LOS) uncertainty consists primarily of small mechanical excursions in the optical sensor which cannot be calibrated out, caused by thermal expansion and launch effect. The main effect of the noise is a tremble of the visual features in the image plane. The variances of the errors can be expressed in pixel. With growing distance the LOS effect grows, which results in a greater error of the triangulated position. They are fundamentally unavoidable, but their effect can be significantly reduced:

- The effect of shot noise decreases with the increase of exposure time
- The effect of random dark signal component cane be reduced by cooling the sensor
- Readout noise of the sensor can be reduced by selecting the appropriate mode of operation of the device

2.5 Orbital Mechanics and perturbation

Newton's law of universal gravitation describes the physics that allow satellites to be put into orbit. Essentially, the satellites are in freefall towards the earth but moving fast enough parallel to the curvature of the earth that they never hit the ground. An orbit is described by an ellipse on a plane through the earth's center of gravity. It is characterized by six orbital elements, described in **table 9**

Element	Symbol	Description
Semi-major axis	**a**	Shape of elliptic orbit
Eccentricity	**e**	Shape of elliptic orbit
Inclination	**i**	Orientation of the orbital plane
Right ascension of the ascending node (RAAN)	**Ω**	Orientation of the orbital plane
Argument of perigee	**ω**	Orientation of the orbital plane
Mean anomaly at epoch	**ν**	Position in orbit at specific time

Table 9: Six orbital element

The equation that governs the motion of the satellite/RSO relative to the Earth is given by the two bodies problem. This second order differential equation doesn't take into account the perturbation forces that a resident space object is subject in orbit but it can be used in different situations.

2.5.1 Perturbation Forces

When predicting short-term evolution of orbital motion in proximity of a relatively large gravitational attractor, the simplified two body problem is sufficient; however, when estimating long-term orbital evolution, the effect of perturbation must be taken into account. Orbital perturbations in proximity of Earth can be classified in the three following categories:

- Perturbations due to the presence of the other large celestial bodies but mainly Moon and Sun ($\ddot{\vec{r}}_{LS}$)
- Perturbation due to the Earth not being a perfect point-mass ($\ddot{\vec{r}}_{G}$)
- Perturbations due to non-gravitational sources like Residual atmospheric drag ($\ddot{\vec{r}}_{D}$) and Solar radiation pressure ($\ddot{\vec{r}}_{RP}$)

The total perturbation in proximity of Earth is then simply summed into the two-body problem using the Cowell formulation:

$$\ddot{\vec{r}} = \ddot{\vec{r}}_{2B} + \ddot{\vec{r}}_{G} + \ddot{\vec{r}}_{D} + \ddot{\vec{r}}_{LS} + \ddot{\vec{r}}_{RP} \tag{20}$$

$$\ddot{\vec{r}}_{2B} = -\frac{\mu \vec{r}}{r^3} \tag{21}$$

Where: $\boldsymbol{\mu}$: Gravitational parameter, $\vec{\boldsymbol{r}}$: Vector from the center of the Earth to the object, $\boldsymbol{r}$: Magnitude of the vector

$$\ddot{\vec{r}}_G = \left(\frac{\partial V}{\partial \vec{r}}\right)^T \tag{22}$$

$$V = \frac{\mu}{r}\left(\sum_{n=2}^{n_{max}}\left(\frac{a_e}{r}\right)^n \sum_{m=0}^{n} P_{nm}(sin(\varphi)[\quad cos(m\lambda) + S_{nm}sin(m\lambda)]\right) \tag{23}$$

Where: $\boldsymbol{a_e}$**:** Mean equatorial radius of the Earth**,** $\boldsymbol{P_{nm}}$**:** Legendre polynomials**,** $\boldsymbol{\varphi}$ and $\boldsymbol{\lambda}$ **:** latitude and longitude of sub-point**;** $\boldsymbol{P_{nm}}$ and $\boldsymbol{S_{nm}}$**:** Constant called spherical harmonics whose values depends on the Earth model selected

$$\ddot{\vec{r}}_D = -\frac{1}{2}\frac{C_d A}{m}\rho \vec{v}_a v_a \tag{24}$$

Where**:** $\boldsymbol{C_d}$**:** Coefficient of Drag**,** **A:** Frontal area of the object**,** **m:** Mass of the object**,** $\boldsymbol{\rho}$**:** Local atmospheric density**,** $\vec{\boldsymbol{v}}_{\boldsymbol{a}}$**:** Vector velocity of the object relative to the atmosphe**re.**

$$\ddot{\vec{r}}_{LS} = -\mu_m\left(\frac{\vec{r}_{mb}}{|\vec{r}_{mb}|^3} + \frac{\vec{r}_{em}}{|\vec{r}_{em}|^3}\right) - \mu_s\left(\frac{\vec{r}_{sb}}{|\vec{r}_{sb}|^3} + \frac{\vec{r}_{es}}{|\vec{r}_{es}|^3}\right) \tag{25}$$

Where: $\boldsymbol{\mu_m}$**:** Gravitational constant of the Moon, $\boldsymbol{\mu_s}$: Gravitational constant of the Sun, $\vec{\boldsymbol{r}}_{\boldsymbol{mb}}$: Position vector from Moon to S/C, $\vec{\boldsymbol{r}}_{\boldsymbol{sb}}$: Position vector from Sun to S/C; $\vec{\boldsymbol{r}}_{\boldsymbol{em}}$: Position vector from Earth to Moon; $\vec{\boldsymbol{r}}_{\boldsymbol{es}}$: Position vector from Earth to Sun

$$\ddot{\vec{r}}_{RP} = \Gamma \frac{\vec{r}_{sb}}{|\vec{r}_{sb}|^3} \tag{26}$$

Where: $\boldsymbol{\Gamma}$**:** Solar radiation pressure coefficient

The **figure 20** shows the influence of the perturbations force for a spacecraft orbiting in LEO.

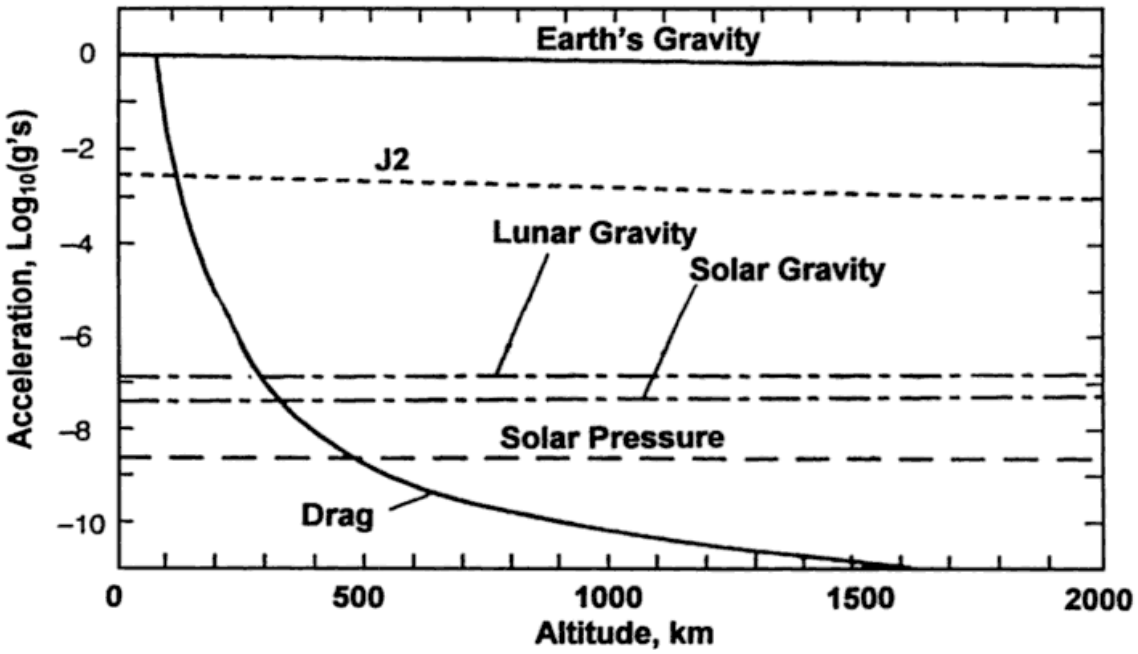

Figure 20: Perturbations effect vs altitude

2.5.2 Effects of the Earth's oblateness

The earth is an oblate spheroid, lacking the perfect symmetry of a sphere (A basketball can be made an oblate spheroid by sitting on it.). This lack of symmetry means that the force of gravity on an orbiting body is not directed towards the center of the Earth. Whereas the gravitational field of a perfectly spherical planet depends only on the distance from its center, oblateness causes a variation also with latitude, that is, the angular distance from the equator (or pole). This is called a zonal variation. The dimensionless parameter which quantifies the major effects of oblateness on orbits is J_2, the second zonal harmonic. J_2 is not a universal constant and each planet has its own
value. This generates a perturbing acceleration $\mathbf{p}$ that can be resolved into three components: the radial $\mathbf{p}_r$, the trasverse $\mathbf{p}_\perp$ and the normal $\mathbf{p}_h$.
The mainly effects of this perturbing acceleration are the time variation of the right ascension and the change of the argument of perigee [66]
The average rate of precession of the node line can be expressed by the equation:

$$\dot{\Omega} = -\left[\frac{3}{2}\frac{\sqrt{\mu}\, J_2\, R^2}{(1-\ e^2)^2 a^{\frac{7}{2}}}\right]\cos(\mathbf{i}) \tag{27}$$

Observe that if $0< \mathbf{i} <90°$ then $\dot{\Omega} < 0$. That is, for posigrade orbits, the node line drifts westward. Since the right ascension of the node continuously decreases, this phenomenon is called regression of the nodes. If $90°< \mathbf{i} <180°$ we see that $\dot{\Omega} >0$. The node line of retrograde orbits therefore advances eastward. For the polar orbit ($\mathbf{i} = 90°$) the node line is stationary. In a similar fashion the time rate of change of the argument of perigee is found to be:

$$\dot{\omega} = -\left[\frac{3}{2}\frac{\sqrt{\mu}\, J_2\, R^2}{(1-\ e^2)^2 a^{\frac{7}{2}}}\right]\left(\frac{5}{2}\sin^2(\mathbf{i}) - 2\right) \tag{28}$$

Figure 21 is a plot of **Equations 27** and **28** for several low-earth orbits. The effect of oblateness on both $\dot{\Omega}$ and $\dot{\omega}$ is greatest at low inclinations, for which the orbit is near the equatorial bulge for longer portions of each revolution.

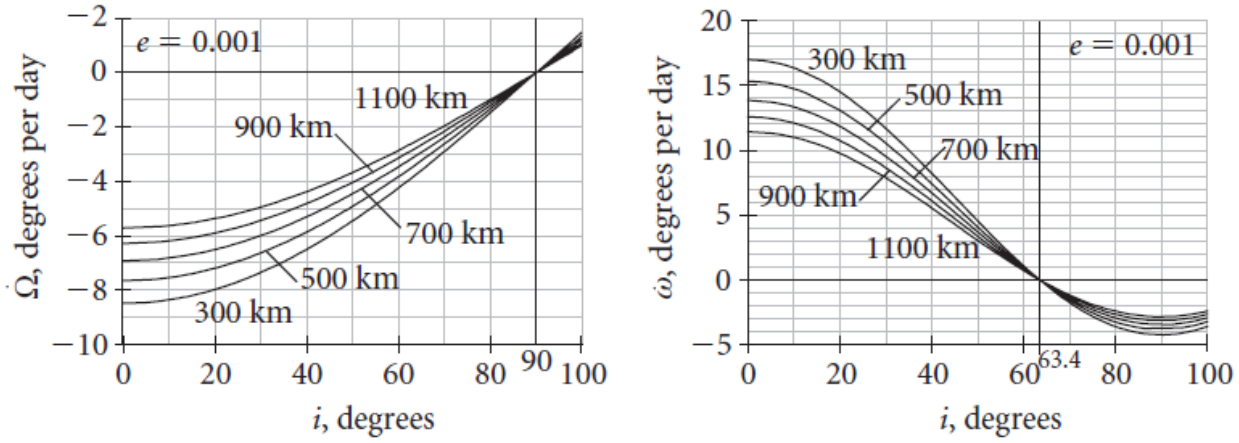

Figure 21: Regression of the node and advance of perigee for nearly circular orbits [66]

As described in ref. [66], The effect of orbit inclination on node regression and advance of perigee is taken advantage of for two very important types of orbits. Sun-synchronous orbits are those whose orbital plane makes a constant angle α with the radial from the sun, as illustrated in **Figure 22**. For that to occur, the orbital plane must rotate in inertial space with the angular velocity of the earth in its orbit around the sun, which is 360° per 365.26 days, or 0.9856° per day. With the orbital plane precessing eastward at this rate, the ascending node will lie at a fixed local time. In the illustration it happens to be 3 pm. During every orbit, the satellite sees any given swath of the planet under nearly the same conditions of daylight or darkness day after day. The satellite also has a constant perspective on the sun.

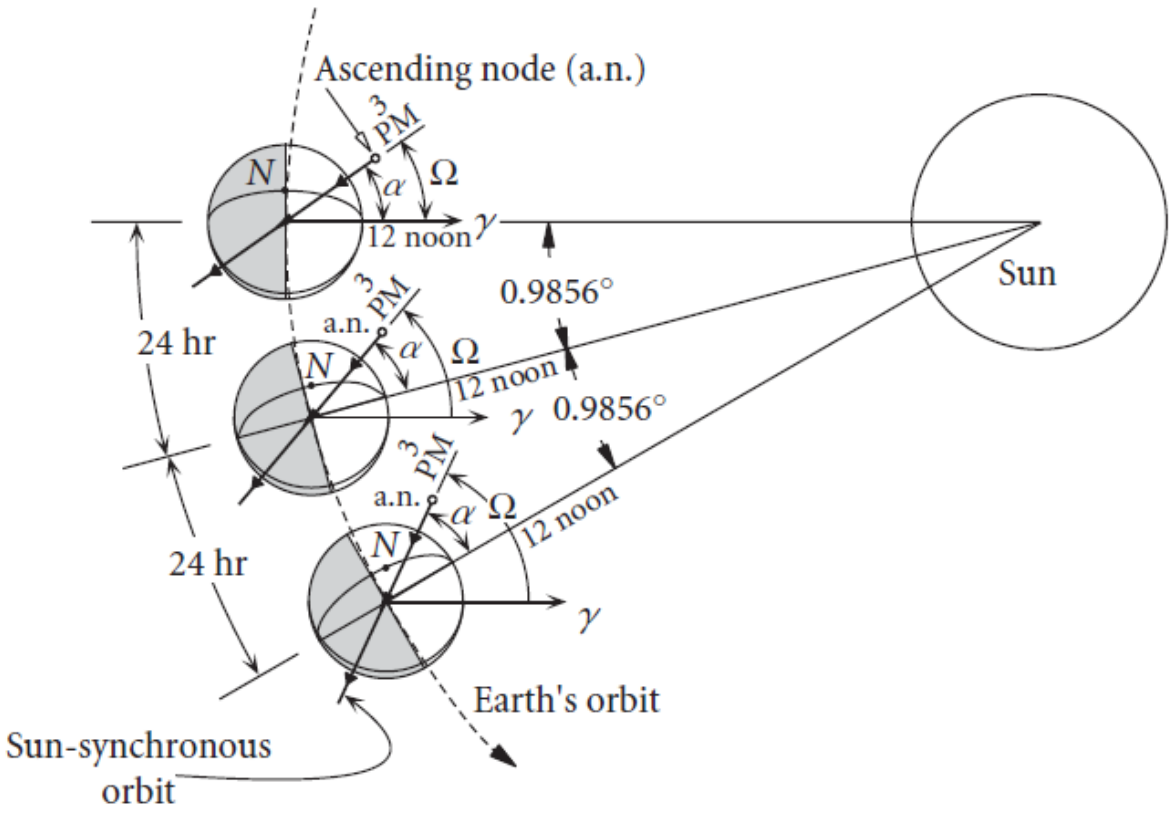

Figure 22: Sun-Synchronous Orbit [66]

2.6. Orbital uncertainty propagation methods

Orbit propagation begins with an estimation of a space object's state vector. State measurement(s) are given by ground or on-board surveillance and navigation systems, for which measurement uncertainties can be assumed to be Gaussian and described by a mean and covariance matrix or PDF, unless otherwise recommended. From this initial state measurement, the orbit is propagated using one of the various approaches, inflating the position uncertainty ellipsoid with respect to time until the next measurement, which is commonly dictated by the update rate or availability of the navigation and/or surveillance system.

The estimation of state can be seen as a convergent process that shrinks the volume of the ellipsoid at each observation epoch. Additionally, if any actuation is performed by the spacecraft the associated uncertainties should be included in the propagation at the time of maneuvre [11].

An intuitive and rigorous empirical technique to propagate uncertainties and to reconstruct a statistical distribution is to perform the well-known Monte Carlo simulation, which involves the perturbation of initial states and of the dynamic coefficients in all their possible combinations.

Nonetheless, conducting this approach with high fidelity is computationally expensive and can be deemed impractical in evaluating most collision scenarios.

A theoretical treatment of the stochastic uncertainty propagation in dynamic systems was attempted as early as 1914 and led to the Fokker-Plank Equation (FPE), which describe the evolution of the PDF in time for a problem that satisfies the Ito stochastic differential equation. This approach augments the original deterministic flight mechanics equations with statistical moments. Although extensive efforts were targeted at the development of a computationally efficient solution method for the FPE, the high dimensionality and the significant nonlinearities of rigid-body (6-DoF) orbital mechanics so far encumbered these efforts and forced to make extensive use of linearity and Gaussian statistics [54]. To overcome the challenges associated with the rigorous statistical treatment of nonlinearities and high-dimensionality, it is necessary to employ approximation methods. Lou and Yang [11] provide a comprehensive review on the available uncertainty propagation methods for spaceflight mechanics. Their ontology is recaptured in **Figure 23**.

Of these, linear methods provide the user with a convenient approach as only the mean position and covariance matrix need to be propagated when the following assumptions are taken [11]:

1. A linearized model sufficiently approximates the dynamics of neighbouring trajectories with respect to a nominal trajectory
2. The uncertainty can be completely characterized by a Gaussian probability distribution.

The dynamics can then be linearized via local or statistical means under the well-known Linear Covariance analysis (LinCov) and CADET [55, 56] techniques, respectively.

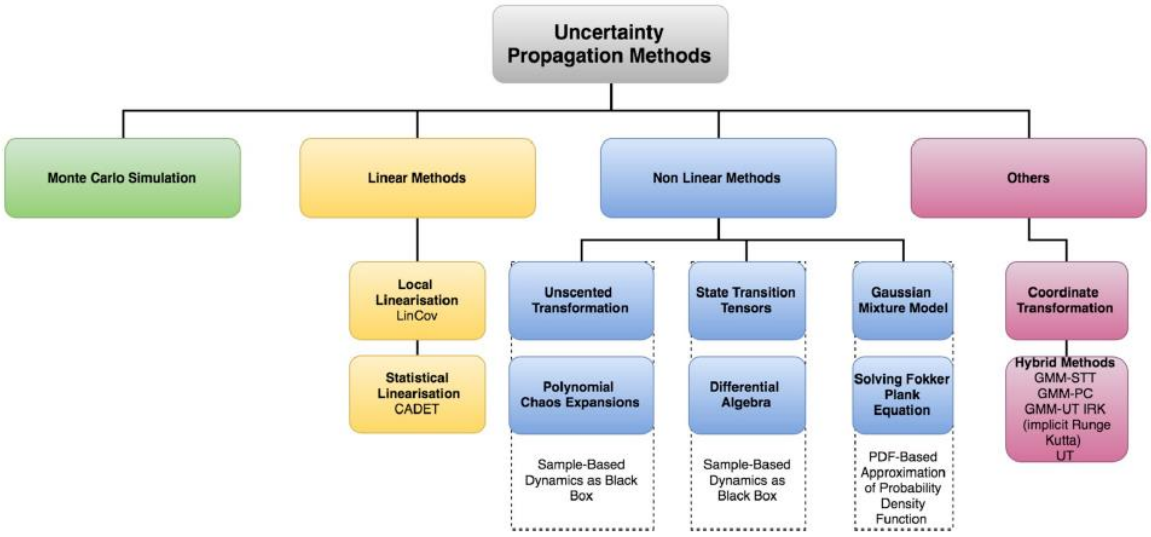

Figure 23: Ontology of uncertainty propagation methods [1]

2.6.1 Linear Orbital Propagation

Linear Covariance Analysis (LinCov) is a class of statistical analysis techniques to produce an accurate statistical portrayal of estimation errors and to assess the impact of neglecting to estimate on the accuracy of the state estimate. The basic operation of the LinCov analysis is as follow:

- Load idealized reference trajectory $\bar{x}$(t)
- Initialize augmented covariance matrix P_0 based on initial uncertainties
- Propagate covariance matrix using the expression:

$$P_i = \boldsymbol{\phi}(t, t_0)\, P_{i-1} \boldsymbol{\phi}(t, t_0)^{\boldsymbol{T}} \tag{29}$$

where $\boldsymbol{\phi}(t, t_0)$ is state transition matrix calculated using Markley's method [57].

Markley's method uses two states, one at t_{k-1} time and the other at the t_k time and calculates the transition matrix between them by using μ, J_2, Δt and two state vectors.

Markley's method consists of making one approximation for the transition matrix of the state vector based on the Taylor series expansion for short intervals of propagation, Δt. This method can be used by any kind of orbit and the equations are simple and easily implemented.

The state transition's differential equation is defined by:

$$\frac{d\boldsymbol{\phi}(t, t_0)}{dt} = \begin{bmatrix} 0 & \mathbf{I} \\ \boldsymbol{G}(t) & 0 \end{bmatrix} \boldsymbol{\phi}(t, t_0) \tag{30}$$

Where $\boldsymbol{\phi}(t, t_0)$ is state transition matrix at time t, $\boldsymbol{G}(t) \equiv \partial \mathbf{a}(\mathbf{r},t)/\, \partial \mathbf{r} \equiv$ the gradient matrix, $\mathbf{r} = (x\ y\ z)^T$ $\mathbf{v} = (\dot{x}\ \dot{y}\ \dot{z})^T$ are the Cartesian state at the instant t, $\mathbf{a}(\mathbf{r},t)$ is the accelerations of the satellite.

Developing $\boldsymbol{\phi}(t, t_0)$ in Taylor's series at $t = t_0$ the transition matrix of the position and velocity obtained after some simplifications is given by:

$$\boldsymbol{\phi}(t, t_0) \approx \begin{bmatrix} \boldsymbol{\phi}_{rr} & \boldsymbol{\phi}_{rv} \\ \boldsymbol{\phi}_{vr} & \boldsymbol{\phi}_{vv} \end{bmatrix} \tag{31}$$

Where:

$$\begin{aligned} \boldsymbol{\phi}_{rr} &\equiv \mathrm{I} + (2G_0 + G)\,\frac{(\Delta \mathrm{t})^2}{6} \\ \boldsymbol{\phi}_{rv} &\equiv \mathrm{I}\,\Delta \mathrm{t} + (G_0 + G)\,\frac{(\Delta \mathrm{t})^3}{12} \\ \boldsymbol{\phi}_{vr} &\equiv (G_0 + G)\,\frac{(\Delta \mathrm{t})}{2} \\ \boldsymbol{\phi}_{rv} &\equiv \mathrm{I} + (G_0 + 2G)\,\frac{(\Delta \mathrm{t})^2}{6} \end{aligned} \tag{32}$$

And $\Delta \mathrm{t} = \mathrm{t} - t_0$, $G_0 \equiv G(t_0)$

The **G** gradient matrix including only the central force and the J_2 is given by:

$$\mathbf{G}(\mathrm{t}) = \partial \mathbf{a}(\mathbf{r}, t)/\,\partial \mathbf{r} = \begin{bmatrix} \frac{\partial a_x}{\partial x} & \frac{\partial a_x}{\partial y} & \frac{\partial a_x}{\partial z} \\ \frac{\partial a_y}{\partial x} & \frac{\partial a_y}{\partial y} & \frac{\partial a_y}{\partial z} \\ \frac{\partial a_z}{\partial x} & \frac{\partial a_z}{\partial y} & \frac{\partial a_z}{\partial z} \end{bmatrix} \tag{33}$$

2.7 STM framework and regulatory environment

The development of STM system will require the implementation of policy, rules and regulations, standards, guidelines.
This task that will not be accomplished without significant legal and political barriers. In any case, policy related decisions will have significant influence on chosen technology and operational framework employed in a STM system. The technology domain acts to provide an STM system with Space Situational Awareness (SSA), which at a minimum, will enable an acceptable level of space-flight safety. This requires the necessary integration of products and services, applications, computing platforms, data sensors and other related technological aspects that together curtail the risks associated with existing and projected increase of orbital traffic. How these SSA related tools are controlled and maintained will be subject to the systematic steps, activities and actions defined within the operational domain. Evidently, the level of autonomy that will exist in executing these processes and procedures will be dictated by the complexity of required decisions and the effectiveness of Human Machine Interaction (HMI) within the operational environment. Decisions made within the policy domain shall capitalize on historical lessons, proven research, technical considerations, and operational limitations and time-lines [58]
The "*outer space treaty*" developed by the United States, United Kingdom, and the Soviet Union provides the basis of an STM framework. Comprised of 17 articles, the treaty addresses fundamental concerns including the non-ownership of orbits and appropriation of space (Articles I, II), operator responsibilities in situations of distress (Article V) and damage liabilities from in space accidents (Article VII) among others. Although foundational, the Outer Space Treaty at present does not provide the necessary framework to assign space traffic management functions to new international decision-making STM authorities [59]. To accommodate such an aspect, it has been recommended that the treaty should be amended to establish a standing international organization for STM, equivalent to ICAO and related atmospheric traffic standards and services [59]. Nevertheless, fast-forward 50 years and the problematic scenarios associated with the absence of a central STM authority are now becoming increasingly tangible.

2.7.1 Space Debris Mitigation problem

In 1995 NASA was the first space agency in the world to issue a comprehensive set of orbital debris mitigation guidelines. Two years later, the U.S. Government developed a set of "*Orbital Debris Mitigation Standard Practices*" based on the NASA guidelines. Other countries and organizations, including Japan, France, Russia, and the European Space Agency (ESA), have followed suit with their own orbital debris mitigation guidelines. In fact, in February 1999, ESA issued a Space Debris Mitigation Handbook, followed by a draft Space Debris Safety and Mitigation Standard in 2000. In 2002, after a multi-year effort, the Inter-Agency Space Debris Coordination Committee (IADC), comprised of the space agencies of 10 countries (ASI, CNES, CNSA, CSA, DLR, ESA, ISRO, JAXA, KARI, NASA,

ROSCOSMOS, SSAU, and UKSA) adopted a consensus set of guidelines designed to mitigate the growth of the orbital debris population.
In February 2007, the Scientific and Technical Subcommittee (STSC) of the United Nations' Committee on the Peaceful Uses of Outer Space (COPUOS) completed a multi-year work plan with the adoption of a consensus set of space debris mitigation guidelines based on the IADC guidelines. The guidelines were accepted by the COPUOS in June 2007 and endorsed by the General Assembly of the United Nations in late 2007.
The information contained in these documents address the specific hazard(s) present during each operational phase (launch, re-entry, on-orbit). The launch and re-entry phases are principally concerned with range safety which is addressed by Standard 321-07 "Common Risk Criteria Standards for National Test Ranges". Standard 321-07 also extends to the on-orbit environment where separation and collision probability requirements are provided. Moreover, the on-orbit phase is subject to the irrefutably hazardous space-debris environment, with increasing concerns of initiating an irreversible, cascading debris generating process widely recognised as Kessler syndrome [61, 62]. By 2009, the intentional destruction of the Chinese weather satellite Fengyun-1C in 2007, along with the accidental collision between Iridium 33 and Cosmos 2251 in 2009, greatly increased the amount of debris in LEO. As a result, the likelihood that active spacecraft would collide with orbital debris increased significantly. The **figure 24** underlines the importance of the mitigation guidelines, showing the uncertainty of RSO number without mitigation actions

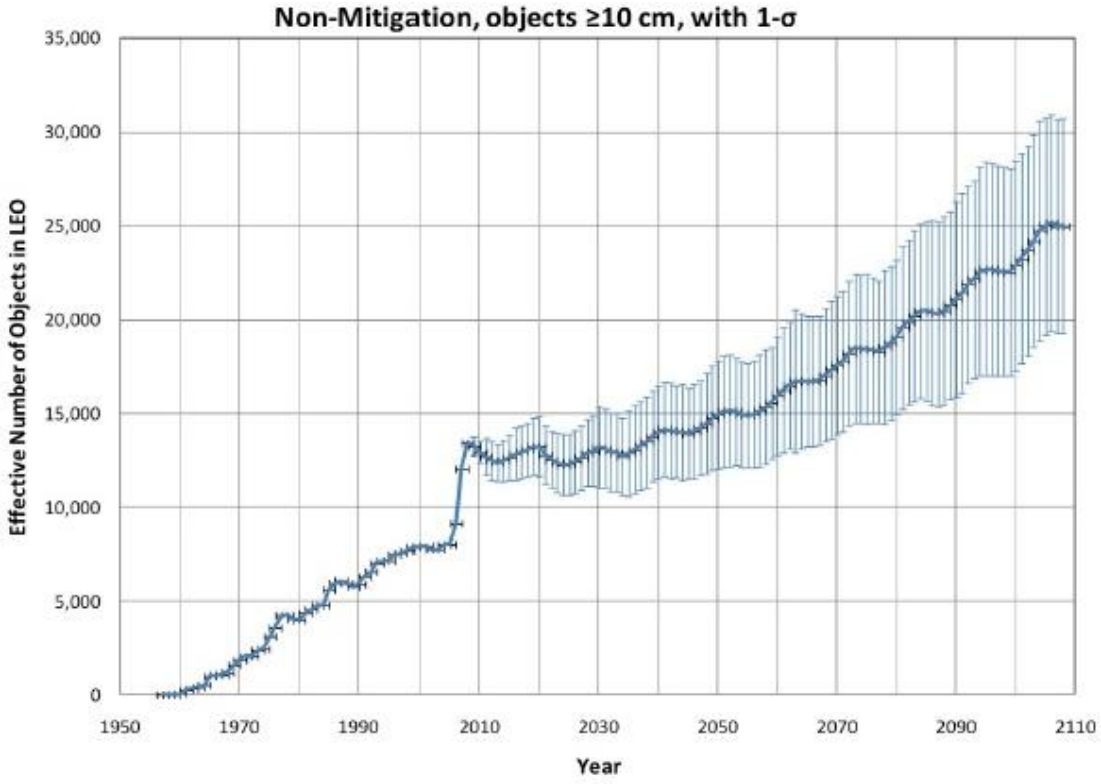

Figure 24: 2009 projection of orbital debris in LEO [Credit NASA]

2.7.1.1 Space Debris Mitigation Guidelines

Founded on the common findings and recommendations produced by several international and national agencies such as NASA, DLR, JAXA, ESA, AIAA, the IADC "Space Debris Mitigation Guidelines" have been developed as a comprehensive reference on recommended orbital debris mitigation strategies [60]. Focusing specifically on the following aspects, the IADC aims to provide guidance across all operational phases (launch, mission and disposal) of spacecraft and launch vehicle orbital stage:

1. Limitation of debris released during normal operations
2. Minimization of the potential for break-ups during operational phases
3. Limitation the probability of accidental collision in orbit
4. Avoid intentional destruction and other harmful activities
5. Minimization the potential for post-mission breaks-up resulting from stored energy
6. Limitation of the long-term presence of spacecraft and launch vehicle orbital stage in the LEO and GEO region after the end of their mission

Figure 25 illustrates the IADC framework, highlighting common causes of orbital debris and recommended mitigation practices across both operational and end of mission phases. Distinction is also made between the typical categories of space debris associated with different causes.

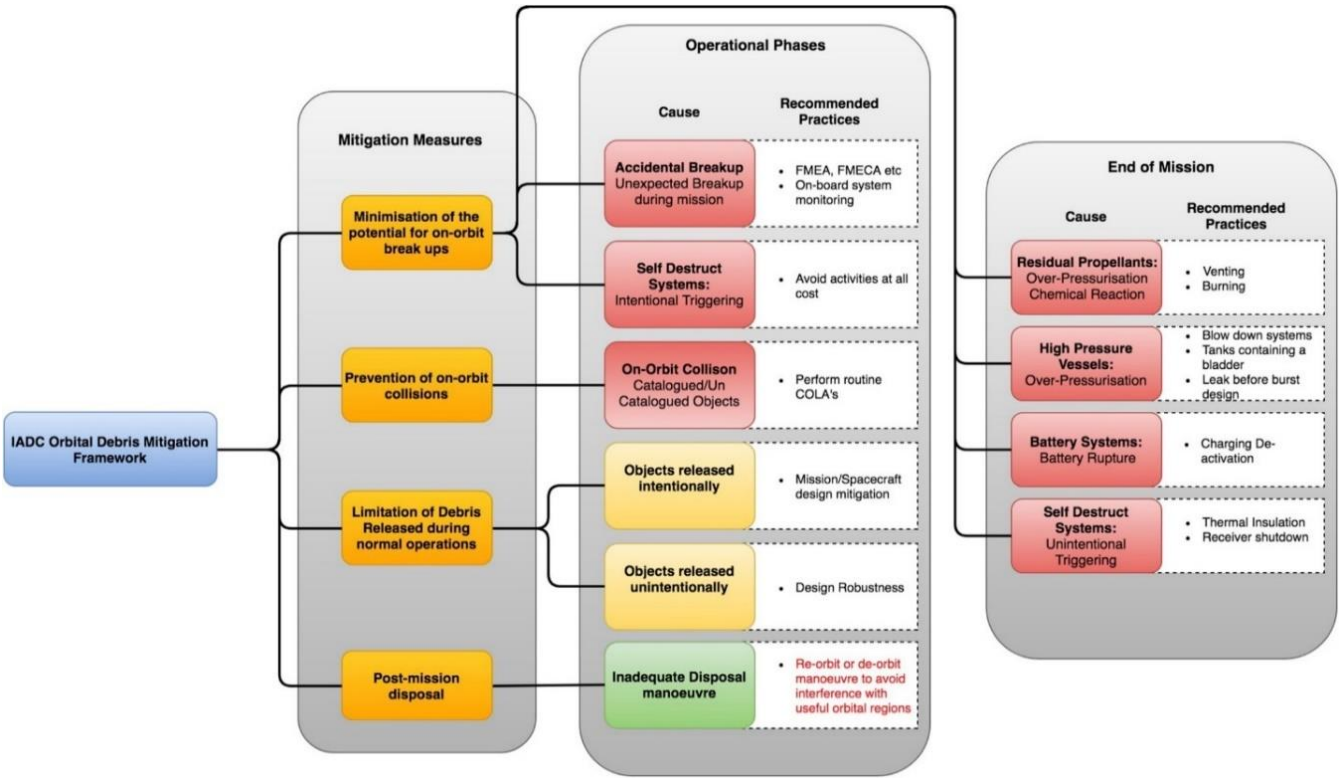

Figure 25: IADC orbital debris mitigation framework. Mission-related debris, fragments and spacecraft/rocket bodies are designated yellow, red and green respectively.

3. Models and Tools

We outline here a mathematical framework to combine tracking and navigation uncertainty with the aim providing a rigorous methodology to describe and analyse the position uncertainty of a tracked RSO from different platforms, subject to navigation errors if we consider a Space-Based Surveillance (SBS) platform. We define a "Navigation" coordinate system from which measurements from the space-based or the ground-based are made within.

Radar and then Passive optical error models for the Tracking model are developed. Instead representative values of navigation (NAV) performance are selected from documented on-orbit GPS performance. To represent the uncertainty in a convenient and common reference frame coordinate transformations are required.

Attention is then turned to methods to assess the "realism" of the uncertainty under Gaussian assumptions using two common approaches - the Average Mahalanobis Distance (AMD) statistic metric and Cramer–von Mises (CVM) test. A Monte-Carlo framework is then presented to obtain the required Empirical Distribution of both tracking and navigation uncertainty. The quantification of the total uncertainty, in a common reference frame, at the sensor level and an analysis of the tracking limitations to uphold uncertainty realism assumptions are the results of this model [72].

The flowchart in **Figure 26** shows the framework of the proposed model

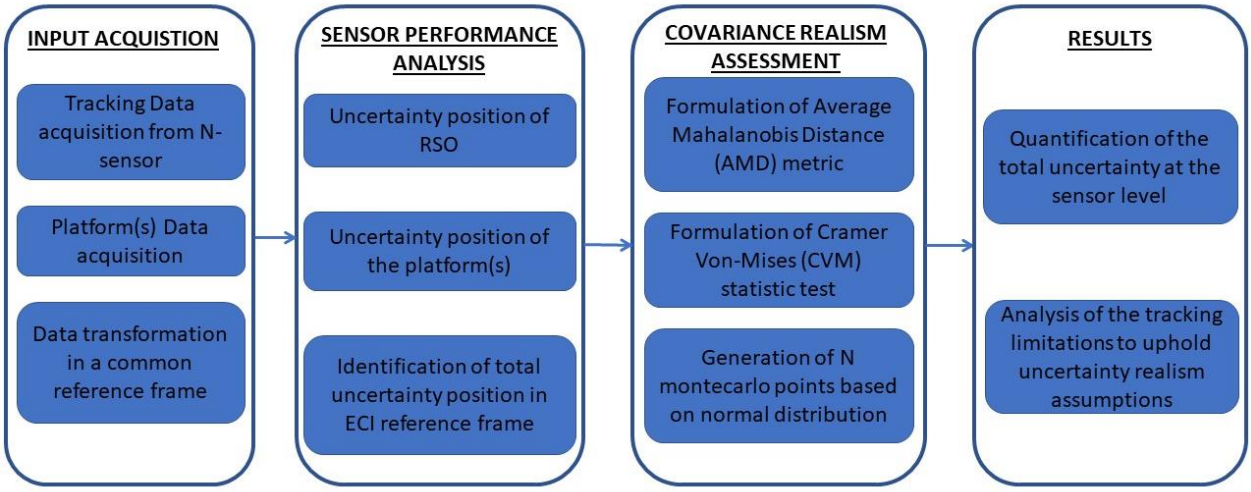

Figure 26: Proposed Approach flowchart and associated processes

3.1. Uncertainty Quantification using Radar system

The target state vector information is measured relative to the radar site in a spherical coordinate system in range, elevation and azimuth ($r_{RDR}, \eta_{RDR}, \epsilon_{RDR}$ respectively) as shown in **Figure 27 a**

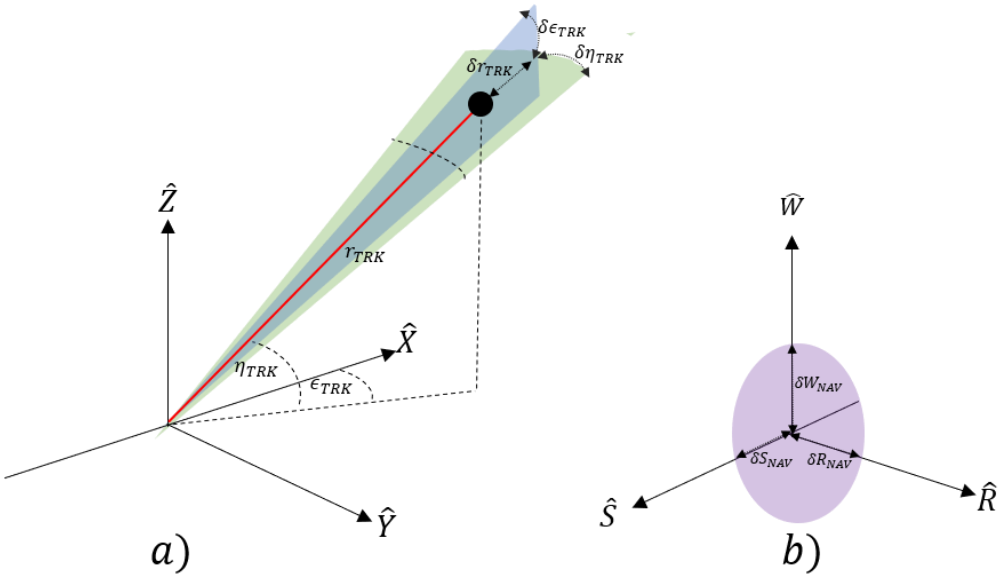

Figure 27: Generic Tracking (a) and Navigation (b) RSW coordinate systems detailing corresponding error geometry.

The RSW satellite coordinate system is chosen to express position uncertainty of RSO. At the time of observation, we assume that the nominal spacecraft position (SP) is centered at the origin of the RSW axis. The Radial (R) axis always points from the earth centre along the radius vector towards the satellite. The S-Axis is pointed tangentially to the track's direction, where, in the case of elliptical orbits, it is only parallel to the velocity vector at apogee and perigee. The W (cross-track) axis is normal to the orbital plane and completes the right-hand triad (**Figure 27b**). The coordinate system can then be constructed through the following unit vector approach [28]:

$$\widehat{\boldsymbol{R}} = \frac{R_{ECI}}{|R_{ECI}|} \tag{34}$$

$$\widehat{\boldsymbol{W}} = \frac{R_{ECI} \times V_{ECI}}{|R_{ECI} \times V_{ECI}|} \tag{35}$$

$$\widehat{\boldsymbol{S}} = \widehat{\boldsymbol{W}} \times \widehat{\boldsymbol{R}} \tag{36}$$

The transfer matrix(s) between the RSW and ECI coordinate systems is then following:

$$M_{RSW \to ECI} = \left[\widehat{\boldsymbol{R}}\,\widehat{\boldsymbol{S}}\,\widehat{\boldsymbol{W}}\right] \quad M_{ECI \to RSW} = \left[\widehat{\boldsymbol{R}}\,\widehat{\boldsymbol{S}}\,\widehat{\boldsymbol{W}}\right]^T \tag{37) (38}$$

Positional errors from the on-board navigation system are then expressed as deviations, $\delta \boldsymbol{X_{NAV}}$, from the origin of the axis, defined as the difference between the true state, $\boldsymbol{X_{NAV}}$, and the nominal state $\bar{\boldsymbol{X}}_{\boldsymbol{NAV}}$ under the zero mean

$$\delta \boldsymbol{X_{NAV}} = \boldsymbol{X_{NAV}} - \bar{\boldsymbol{X}}_{\boldsymbol{NAV}} \tag{39}$$

$$\boldsymbol{X_{NAV}} = \begin{bmatrix} R_T \\ S_T \\ W_T \end{bmatrix}, \bar{\boldsymbol{X}}_{\boldsymbol{NAV}} = \begin{bmatrix} R_N \\ S_N \\ W_N \end{bmatrix} \tag{40}$$

Navigation uncertainty is assumed to be Gaussian, and can then be expressed in terms of covariance, where the assumption of zero main is made:

$$Q_{NAV}{}^{RSW} = E\left[\delta \boldsymbol{X_{NAV}} \delta \boldsymbol{X_{NAV}}^T\right] = \begin{bmatrix} \sigma_{R_{NAV}}{}^2 & 0 & 0 \\ 0 & \sigma_{S_{NAV}}{}^2 & 0 \\ 0 & 0 & \sigma_{W_{NAV}}{}^2 \end{bmatrix} \tag{41}$$

Similarly, tracking measurement errors are expressed as measurement deviations in the spherical dimension, $\delta \boldsymbol{X_{TRK}}$, defined as the difference between the true state, $\boldsymbol{X_{TRK}}$, and the nominal state $\bar{\boldsymbol{X}}_{\boldsymbol{TRK}}$ of the RSO [29].

$$\delta \boldsymbol{X_{TRK}} = \boldsymbol{X_{TRK}} - \bar{\boldsymbol{X}}_{\boldsymbol{TRK}} \tag{42}$$

$$\boldsymbol{X_{TRK}} = \begin{bmatrix} r_T \\ \epsilon_T \\ \eta_T \end{bmatrix}, \bar{\boldsymbol{X}}_{\boldsymbol{TRK}} = \begin{bmatrix} r_N \\ \epsilon_N \\ \eta_N \end{bmatrix} \tag{43}$$

The tracking error of the radar is then expressed in terms of covariance:

$$Q_{TRK}{}_{SPH}^{RDR} = E\left[\delta \boldsymbol{X_{TRK}} \delta \boldsymbol{X_{TRK}}^T\right] = \begin{bmatrix} \sigma_{r_{TRK}}{}^2 & 0 & 0 \\ 0 & \sigma_{\epsilon_{TRK}}{}^2 & 0 \\ 0 & 0 & \sigma_{\eta_{TRK}}{}^2 \end{bmatrix} \tag{44}$$

To combine NAV & TRK uncertainty from the spacecraft and tracked RSO both covariance matrices must belong to the same coordinate frame. In this case, a transformation from the spherical to the Cartesian system must be performed. Position and velocity measurements (and uncertainty) should be expressed in a reference frame that is most convenient to the user, where in this case a Cartesian Earth-Centered Inertial (ECI) frame is chosen. As such, the navigation covariance matrix must be transformed to the Cartesian Earth-Centred inertial (ECI) frame. As this is a linear process (cartesian to cartesian), a simple coordinate transformation can be applied to the covariance matrix. Following the derivation of the RSW to ECI transformation matrix previously described we can write:

$$Q_{NAV}{}_{CART}^{ECI} = M_{RSW \to ECI}\, Q_{NAV}{}_{CART}^{RSW} \cdot M_{RSW \to ECI}{}^T \tag{45}$$

$$Q_{NAV}{}_{CART}^{ECI} = \begin{bmatrix} \sigma_{x_{NAV}}{}^2 & \sigma_{xy_{NAV}} & \sigma_{xz_{NAV}} \\ & \sigma_{y_{NAV}}{}^2 & \sigma_{yz_{NAV}} \\ sym & & \sigma_{z_{NAV}}{}^2 \end{bmatrix} \tag{46}$$

In contrast, the tracking covariance matrix is expressed in a spherical coordinate system within the radar frame. This requires both a transformation from spherical to Cartesian system and then a translation to the ECI frame. As the transformation between these systems is nonlinear, a basic coordinate transformation is not sufficient, and mathematical tools such the Jacobian of the spherical to Cartesian transformation matrix must be calculated to linearize the process. The spherical to Cartesian Jacobian (D) is expressed as the following, where c, s and represent the cosine and sine of the radar angular measurements.

$$D = \begin{bmatrix} -\,\mathrm{c}\,\epsilon_{TRK}\,\mathrm{c}\,\eta_{TRK} & r_{TRK}\,\mathrm{c}\,\epsilon_{TRK}\,\mathrm{s}\,\eta_{TRK} & r_{TRK}\,\mathrm{s}\,\epsilon_{TRK}\,\mathrm{c}\,\eta_{TRK} \\ \mathrm{c}\,\epsilon_{TRK}\,\mathrm{s}\,\eta_{TRK} & r_{TRK}\,\mathrm{c}\,\epsilon_{TRK}\,\mathrm{c}\,\eta_{TRK} & -r_{TRK}\,\mathrm{s}\,\epsilon_{TRK}\,\mathrm{s}\,\eta_{TRK} \\ \mathrm{s}\,\epsilon_{TRK} & 0 & r_{TRK}\,\mathrm{c}\,\epsilon_{TRK} \end{bmatrix} \tag{47}$$

The transformation from spherical tracking error matrix in Radar coordinate system to the Cartesian ECI is then given by the following:

$$Q_{TRK}{}_{CART}^{ECI} = (M_{RDR\to ECI} \cdot D) \cdot Q_{TRK}{}_{SPH}^{RDR} \cdot (M_{RDR\to ECI} \cdot D)^T \tag{48}$$

$$Q_{TRK}{}_{CART}^{ECI} = \begin{bmatrix} \sigma_{x_{TRK}}{}^2 & \sigma_{xy_{TRK}} & \sigma_{xz_{TRK}} \\ & \sigma_{y_{TRK}}{}^2 & \sigma_{yz_{TRK}} \\ sym & & \sigma_{z_{TRK}}{}^2 \end{bmatrix} \tag{49}$$

Where $M_{RDR\to ECI}$ is the transformation matrix from the chosen Radar (TRK) coordinate frame to the ECI frame. The covariance matrix of both the navigation and tracking can now be expressed geometrically as an ellipsoid centered about the nominal position in the ECI Frame. Due to the transformation and translations between the Radar Spherical and Cartesian coordinate systems to the ECI frames, the covariance terms within the error matrix (off-diagonal) are now non-zero. The geometric interpretation of Q_{TRK}^{ECI} now requires that the ellipsoid considers both the variances about the principal axis but also the rotation within the cardinal system (ECI).

The navigation and tracking errors are now expressed in a common ECI frame and can be summed together to express the total position uncertainty about the debris in the ECI frame. Measurements are uncorrelated, variance and covariance terms can be summed directly.

$$Q_{TOT} = Q_{TRK} + Q_{NAV} \tag{50}$$

$$Q_{TOT} = \begin{bmatrix} \sigma_x{}^2 & \sigma_{xy} & \sigma_{xz} \\ & \sigma_y{}^2 & \sigma_{yz} \\ sym & & \sigma_z{}^2 \end{bmatrix}^{ECI} \tag{51}$$

The total uncertainty matrix, Q_{TOT}, is now expressed as an ellipsoid centered about the nominal position of the RSO in the ECI Frame. **Figure 28** illustrates the concept of individual navigation and tracking volume and the resultant combined ellipsoid.

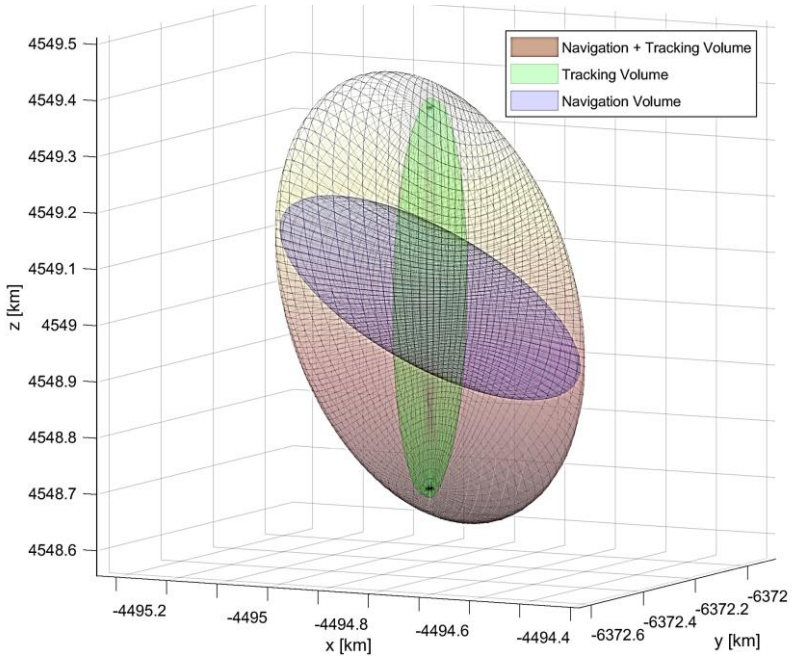

Figure 28: Illustration of navigation, tracking and total error volumes

We can obtain the same result by following the Gauss-Helmert method [27, 28] where the generic form consists in resolution of the following equation system:

$$\boldsymbol{F}(\boldsymbol{X}, \boldsymbol{l}) = \mathbf{0} \tag{52}$$

Where $\boldsymbol{X}, \hat{\boldsymbol{l}}$ are estimated parameters and observation vector respectively. The linearized form of the previous equation is:

$$\boldsymbol{A\delta} + \boldsymbol{Br} + \mathbf{w} = \mathbf{0} \tag{53}$$

Where $\boldsymbol{A} = \frac{\boldsymbol{\partial F}}{\boldsymbol{\partial \hat{X}}}$ and $\boldsymbol{B} = \frac{\boldsymbol{\partial F}}{\boldsymbol{\partial l}}$ are the matrix of partial derivates with respect to $\boldsymbol{X}$, $\boldsymbol{l}$ and $\mathbf{w}$ is the misclosure vector. $\boldsymbol{\delta}$ and $\boldsymbol{r}$, the parameters and observations correction vector respectively, are:

$$\begin{aligned} \widehat{\boldsymbol{\delta}} &= -(\boldsymbol{A^T M A})^{-1} \boldsymbol{A^T M w} \\ \hat{\boldsymbol{r}} &= -\boldsymbol{C_r B^T M}(\boldsymbol{A\delta} + \boldsymbol{w}) \end{aligned} \tag{54}$$

Where $\boldsymbol{M} = (\boldsymbol{BC_r B^T})^{-1}$ and $\boldsymbol{C_r}$ is the covariance matrix of the observations. We obtain the covariance matrix of parameters:

$$C_{NAV+TRK} = (\boldsymbol{A^T M A})^{-1} \tag{55}$$

In our case, equation (37) can be written as:

$$\boldsymbol{F}(\boldsymbol{X}, \hat{\boldsymbol{l}}) = \boldsymbol{X_D} - \boldsymbol{M_{RSW \rightarrow ECI} X_{TRK}} - \boldsymbol{R}_{ECI} = \mathbf{0} \tag{56}$$

Where:

$\boldsymbol{X_D} = \begin{bmatrix} X_D^{ECI} \\ Y_D^{ECI} \\ Z_D^{ECI} \end{bmatrix}$ and $\boldsymbol{R}_{ECI} = \begin{bmatrix} X_h^{ECI} \\ Y_h^{ECI} \\ Z_h^{ECI} \end{bmatrix}$ are the RSO and SBR (host) position in ECI frame

$\boldsymbol{X}_{TRK} = \begin{bmatrix} -r_{TRK} cos(\epsilon_{TRK}) cos(\eta_{TRK}) \\ r_{TRK} cos(\epsilon_{TRK}) sin(\eta_{TRK}) \\ r_{TRK} sin(\epsilon_{TRK}) \end{bmatrix}$ is the position of the target in RSW system.

$\boldsymbol{l} = [r_{TRK}, \epsilon_{TRK}, \eta_{TRK}, x_{NAV}, y_{NAV}, z_{NAV}]^{\boldsymbol{T}}$ is vector of estimated observations

$\boldsymbol{C_r}$= $\begin{bmatrix} \sigma_{r_{TRK}}^2 & & & & & \\ & \sigma_{\epsilon_{TRK}}^2 & & & & \\ & & \sigma_{\eta_{TRK}}^2 & & & \\ & & & {\sigma_{x_{NAV}}}^2 & & \\ & & & & {\sigma_{y_{NAV}}}^2 & \\ & & & & & {\sigma_{z_{NAV}}}^2 \end{bmatrix}$ is the covariance matrix of the observations

We assume that all observations are independent, so all non-diagonal values in the matrix $\boldsymbol{C_r}$ are equal to zero. Since $A_{(3\times3)} = \mathbb{1}$, the covariance matrix of estimated parameters is computed by:

$$\boldsymbol{C}_{NAV+TRK\,(3\times3)} = (\boldsymbol{BC_r B^T}) \tag{57}$$

By applying this method, we obtain a result identical to the initial formulation, confirming the validity of this approach.

From covariance matrix to ellipsoid

It is necessary to study how the covariance matrix represents the ellipsoid in 3D. This analysis This analysis allows us to understand how the single term of the covariance matrix influence the size and the orientation of the ellipsoid.
Using the framework of Principle Component Analysis (PCA), the relation between the covariance matrix, Q, and rotated ellipsoid in $\mathbb{R}^3$ is described by the following:

$$Q = \begin{bmatrix} \sigma_x^2 & \rho_{xy}\sigma_x\sigma_y & \rho_{xz}\sigma_x\sigma_z \\ \rho_{xy}\sigma_x\sigma_y & \sigma_y^2 & \rho_{yz}\sigma_y\sigma_z \\ \rho_{xz}\sigma_x\sigma_z & \rho_{yz}\sigma_y\sigma_z & \sigma_z^2 \end{bmatrix} \tag{58}$$

Where ρ is correlation coefficient given by:

$$\begin{aligned} \rho_{xy} &= \frac{cov(x,y)}{\sigma_x\sigma_y} \\ \rho_{xz} &= \frac{cov(x,z)}{\sigma_x\sigma_z} \\ \rho_{yz} &= \frac{cov(y,z)}{\sigma_y\sigma_z} \end{aligned} \tag{59}$$

Using the covariance matrix Q, the ellipsoid equation can be conveniently expressed as:

$$\vec{x}^T Q^{-1} \vec{x} = 1 \tag{60}$$

Where $\vec{x} = \{x\ y\ z\}^T$ is a vector of Cartesian coordinates. It is therefore necessary to calculate Q^{-1}:

$$Q^{-1} = \frac{1}{\rho}\begin{bmatrix} \frac{1-{\rho_{yz}}^2}{\sigma_x^2} & \frac{-\rho_{xy}+\rho_{yz}\rho_{xz}}{\sigma_x\sigma_y} & \frac{-\rho_{xz}+\rho_{yz}\rho_{xy}}{\sigma_x\sigma_z} \\ \frac{-\rho_{xy}+\rho_{yz}\rho_{xz}}{\sigma_x\sigma_y} & \frac{1-{\rho_{xz}}^2}{\sigma_y^2} & \frac{-\rho_{yz}+\rho_{xy}\rho_{xz}}{\sigma_y\sigma_z} \\ \frac{-\rho_{xz}+\rho_{yz}\rho_{xy}}{\sigma_x\sigma_z} & \frac{-\rho_{yz}+\rho_{xy}\rho_{xz}}{\sigma_y\sigma_z} & \frac{1-{\rho_{xy}}^2}{\sigma_z^2} \end{bmatrix} \tag{61}$$

Where $\rho = (1 + 2\rho_{xy}\rho_{xz}\rho_{yz} - {\rho_{yz}}^2 - {\rho_{xz}}^2 - {\rho_{xy}}^2)$. So, the rotated ellipsoid equation can finally be expressed as:

$$\begin{aligned} \frac{(1-{\rho_{yz}}^2)}{\sigma_x^2}x^2 + \frac{(1-{\rho_{xz}}^2)}{\sigma_y^2}y^2 + \frac{(1-{\rho_{xy}}^2)}{\sigma_z^2}z^2 - \frac{\rho_{xy}-\rho_{yz}\rho_{xz}}{\sigma_x\sigma_y}2xy \\ - \frac{\rho_{xz}-\rho_{yz}\rho_{xy}}{\sigma_x\sigma_z}2xz - \frac{\rho_{yz}-\rho_{xy}\rho_{xz}}{\sigma_y\sigma_z}2yz = \rho \end{aligned} \tag{62}$$

This expression illustrates the contribution of the individual terms of the covariance matrix to the overall ellipsoid shape and size. Concerning the covariance matrix Q itself, its properties are as follows:
Symmetric $Q = Q^T$
Definite positive: $\vec{x}^T Q^{-1} \vec{x} > 0$ for all $\vec{x}$ with $|\vec{x}| \neq 0$
Those two conditions allow to conclude that all eigenvalues λ_i are real and positive, and there exists an orthogonal matrix U of eigenvectors. Q is then written as the following decomposition:

$$Q = U\Lambda U^T \tag{63}$$

where,

$$\Lambda=\begin{bmatrix}\lambda_1 & \cdots & 0\\ \vdots & \ddots & \vdots\\ 0 & \cdots & \lambda_n\end{bmatrix} \tag{64}$$

So, the ellipsoid equation $\vec{x}^T Q^{-1}\vec{x} = 1$ is then:

$$(\vec{x}-\vec{c})^T R\, A^{-1}\, R^T(\vec{x}-\vec{c}) = 1 \tag{65}$$

Where, $\vec{x}$, is a vector of Cartesian coordinates about the nominal position (origin), $\vec{c}$, of the ellipsoid. *R* and *A* are respectively the rotation matrix and the diagonal eigenvalues matrix, each of which are derived from the specific error matrix (Q):

$$\vec{x} = \begin{bmatrix}x_{ECI}\\ y_{ECI}\\ z_{ECI}\end{bmatrix} \tag{66}$$

$$\vec{c} = \begin{bmatrix}x_{ECI_N}\\ y_{ECI_N}\\ z_{ECI_N}\end{bmatrix} \tag{67}$$

$$R = \begin{bmatrix}v_{(1,1)} & v_{(1,2)} & v_{(1,3)}\\ v_{(2,1)} & v_{(2,2)} & v_{(2,3)}\\ v_{(3,1)} & v_{(3,2)} & v_{(3,3)}\end{bmatrix} \tag{68}$$

$$A = \begin{bmatrix}\lambda_1 & 0 & 0\\ 0 & \lambda_2 & 0\\ 0 & 0 & \lambda_3\end{bmatrix} \tag{69}$$

The ellipsoid equation is then transformed to a spherical coordinate system where r, α, ε, are range, azimuth, elevation respectively. The equation can then be parametrized as a function of r to reduce information transfer between cooperative space-based and ground system infrastructure.

$$x = \begin{bmatrix}r\cdot\cos\,\alpha\cdot\cos\varepsilon\\ r\cdot\sin\,\alpha\cdot\cos\varepsilon\\ r\cdot\sin\,\varepsilon\end{bmatrix} \tag{70}$$

Given an angle pairs a corresponding radial distance (R) from the nominal position (centre of ellipse) is then calculated.

$$r^2\,[(\vec{x}-\vec{c})^T R\, A^{-1}R^T\,((\vec{x}-\vec{c}))] = 1$$
$$r\; = [((\vec{x}-\vec{c}))^T R A^{-1}\, R^T\,((\vec{x}-\vec{c}))]^{-\frac{1}{2}} \tag{71}$$

Where, $\alpha \in \{-180^\circ : 180^\circ\}, \varepsilon \in \{-90^\circ : 90^\circ\}$

3.2 Uncertainty Quantification using Optical Sensor

The detection of RSOs position by using passive optical sensors can be solved in two different ways:

- *Initial orbit determination* (IOD) problem: IOD can be solved using multiple observations provided by one single sensor at different times. Angles-only IOD short tracks is subject to large orbit uncertainties, if it is even possible due to the short tracks involved
- *Triangulation technique* with two or more passive, angles-only, optical sensors

In this thesis it will be applied the triangulation technique for the RSO position tracking: a proper formation of small and cooperative spacecraft work in synergy detecting and

tracking common targets. A single angles-only sensor does not provide range information. However, the use of two angles-only sensor allows one to use triangulation to determine range and the 3D RSO position. [65]. Two sensors are placed at known location (x, y, z) and are pointed in the direction of the object. For a focal plane array sensor, triangulation is performed by taking an image of the object for both sensors. The object location in each image is computed and the pointing angle to the object is determined. The pointing angles are usually azimuth and elevation, measured in the reference frame of the sensor platform. These informations will be transformed in a common reference frame.

In order to describe triangulation problem using two angles-only sensors, we need to define a common coordinate system for both sensors as shown in **figure 29**. The x- and y- axis form the horizontal plane and the z-axis pointing in the vertical direction. The azimuth angle (θ) is measured clockwise toward the positive x-axis from the positive y-axis. The elevation angle (φ) increases from 0 in the x-y plane to a maximum of 90° when pointing vertically. We define the horizontal range to target, r_i, as the distance between the x-y components of i^{th} sensor location and the x-y components of target location. The sensor separation angle θ_{Sep} is the angle measured from sensor one through the target to sensor two.

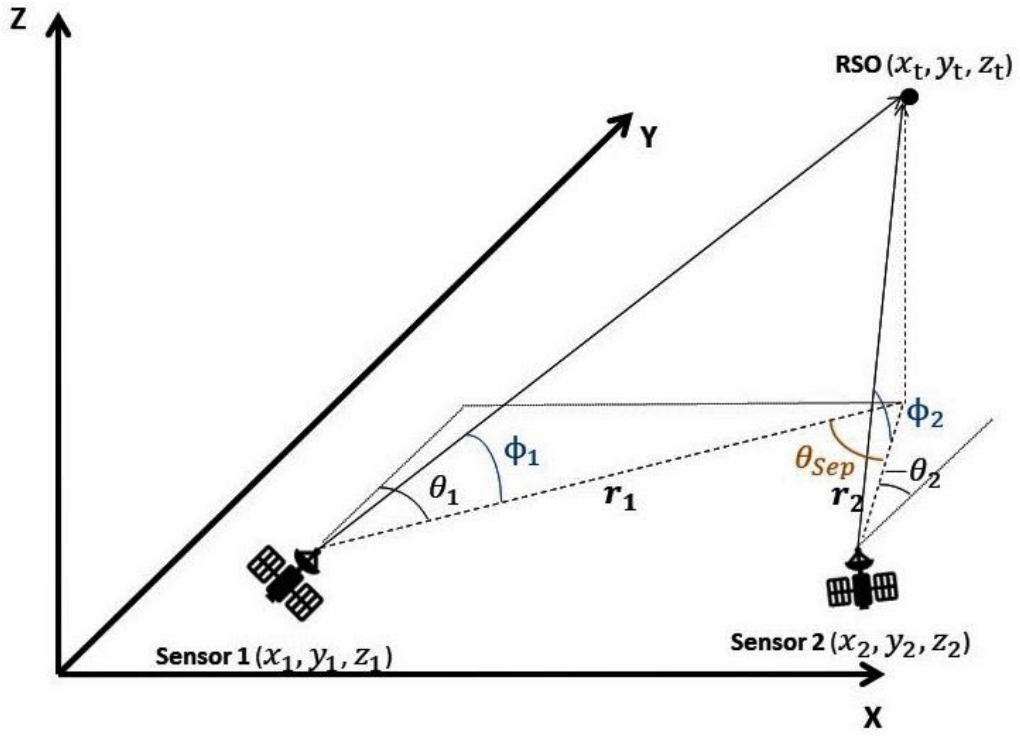

Figure 29: Coordinate system definition, showing target location and i^{th} sensor location

The sensor position and the LOS from the sensor to the target allow us to compute the 3D target location using 3 equation [65]:

$$x_t = \frac{x_2\, tan(\theta_1) - x_1\, tan(\theta_2) + (y_1 - y_2) tan(\theta_1) tan(\theta_2)}{tan(\theta_1) - tan(\theta_2)}$$
$$y_t = \frac{y_1\, tan(\theta_1) - y_2\, tan(\theta_2) + (x_2 - x_1)}{tan(\theta_1) - tan(\theta_2)} \quad (72)$$

$$r_i = \sqrt{(x_i - x_t)^2 + (y_i - y_t)^2}$$

$$z_t = \frac{r_1 tan(\varphi_1) + z_1 + r_2 tan(\varphi_2) + z_2}{2}$$

The uncertainty position of RSO, using multi-sensor platforms, is determined by the accuracy of sensor locations and sensor to target Line of Sight (LOS) knowledge. For each sensor, we need to know sensor location (x, y, z) and the LOS vector (azimuth θ and elevation φ). These five parameters have an error component depending on several other measurements. In order to relate measurement errors (σ_{pos1}, σ_{pos2}, $\sigma_{\theta 1}$, $\sigma_{\theta 2}$, $\sigma_{\varphi 1}$, $\sigma_{\varphi 2}$) to error in our final position (σ_x, σ_y, σ_z) we need to use a mathematic framework based on Gauss-Helmert method.

We define $\boldsymbol{l}$ and $\boldsymbol{X}$, vector of estimated observations and estimated parameters respectively:

$$\boldsymbol{l} = [x_1, y_1, z_1, \theta_1, \varphi_1, x_2, y_2, z_2, \theta_2, \varphi_2]^{\boldsymbol{T}}$$
$$\boldsymbol{X} = [x_t, y_t, z_t]^{\boldsymbol{T}} \quad (73)$$

Where:

- $(x_1, y_1, z_1, \theta_1, \varphi_1)$ and $(x_2, y_2, z_2, \theta_2, \varphi_2)$ are the five parameters of the first and the second sensor respectively
- (x_t, y_t, z_t) is the target position

We need to resolve the following equation:

$$\boldsymbol{F}(\boldsymbol{X}, \boldsymbol{l}) = \boldsymbol{0} \quad (74)$$

That, in this case, can be written:

$$\begin{cases} x_t - \dfrac{x_2\, tan(\theta_1) - x_1\, tan(\theta_2) + (y_1 - y_2) tan(\theta_1) tan(\theta_2)}{tan(\theta_1) - tan(\theta_2)} = 0 \\ y_t - \dfrac{y_1\, tan(\theta_1) - y_2\, tan(\theta_2) + (x_2 - x_1)}{tan(\theta_1) - tan(\theta_2)} = 0 \\ z_t - \dfrac{r_1 tan(\varphi_1) + z_1 + r_2 tan(\varphi_2) + z_2}{2} = 0 \end{cases} \quad (75)$$

The covariance matrix of the observation can be written:

$$\boldsymbol{C_r} = \begin{bmatrix} \sigma_{x_1}^2 & & & & & & & & & \\ & \sigma_{y_1}^2 & & & & & & & & \\ & & \sigma_{z_1}^2 & & & & & & & \\ & & & {\sigma_{\theta_1}}^2 & & & & & & \\ & & & & {\sigma_{\varphi_1}}^2 & & & & & \\ & & & & & \sigma_{x_2}^2 & & & & \\ & & & & & & \sigma_{y_2}^2 & & & \\ & & & & & & & \sigma_{z_2}^2 & & \\ & & & & & & & & {\sigma_{\theta_2}}^2 & \\ & & & & & & & & & {\sigma_{\varphi_2}}^2 \end{bmatrix} \quad (76)$$

We assume that all observations are independent, so all non-diagonal values in the matrix $\boldsymbol{C_r}$ are equal to zero. The covariance matrix of estimated parameters is computed by:

$$\boldsymbol{C}_{TOT\,(3\times3)} = (\boldsymbol{B}\boldsymbol{C_r}\boldsymbol{B^T}) \tag{77}$$

Where: $\boldsymbol{B} = \frac{\boldsymbol{\partial F}}{\boldsymbol{\partial l}}$ is the matrix of the partial derivates respect $\boldsymbol{l}$

3.3 Covariance Realism

Within the SSA/Astrodynamics community, the assessment of covariance realism (also known as covariance consistency) has been predominately focused upon identifying the point at which Gaussian assumptions in the propagation of orbital uncertainty breakdown. As discussed, this paper interested at applying this approach to the sensor level and in turn validating when gaussian assumptions of navigation and tracking error break down. In doing so, 2 commonly used statistical metrics and goodness of fit tests have been adopted. The Mahalanobis distance [30] provides a convenient metric for testing covariance realism, where a set of empirically generated points, $\boldsymbol{x}_{\mathrm{mc}}$, from the measurement model are tested to see if it corresponds to the gaussian distribution defined by a covariance matrix P centered about the truth state, $\boldsymbol{x}_{\mathrm{truth}}$, of the target. The squared Mahalanobis distance between the estimated orbit state and the truth target is defined as:

$$\mathcal{M}((\boldsymbol{x}_{\mathrm{mc}}, \boldsymbol{x}_{\mathrm{truth}}, \mathbf{P}) = (\boldsymbol{x}_{\mathrm{mc}} - \boldsymbol{x}_{\mathrm{truth}})^T \mathbf{P}^{-1} (\boldsymbol{x}_{\mathrm{mc}} - \boldsymbol{x}_{\mathrm{truth}}) \tag{78}$$

The expected value of $\mathcal{M}$ is n, where n is the dimension of the state vector $\boldsymbol{x}_{\mathrm{truth}}$, which in the case of a cartesian coordinate system corresponds to 3. As an uncertainty realism metric, one can consider the values of $\overline{\mathcal{M}}$, averaged over at each observation condition. Let $\mathcal{M}^{(i)}$ be the uncertainty realism metric computed in the i-th Monte Carlo trial. Let k be the total number of independent trials.

$$\overline{\mathcal{M}} = \frac{1}{nk} \sum_{i=1}^{k} \mathcal{M}^{(i)} \tag{79}$$

A stronger test for uncertainty realism is to consider the statistical distribution determined from the measurement model in the form of a physics-based Monte-Carlo simulation. As such, the second covariance realism metric test used is the Cramer–von Mises goodness of fit test statistic [9,10]. This test permits to verify the consistency of the sample and test how well the theoretical Gaussian distribution fits the empirical distribution. The Cramer–von Mises (CVM) test is based in a statistic of the type

$$Q_k = \int_{-\infty}^{+\infty} [F_n(x) - F^*(x)]^2 \varphi(F(x)) dF^*(x) \tag{80}$$

Where $F^*(x)$ is the cumulative distribution function (CDF) of the Mahalanobis distance $\mathcal{M}$ and $F_n(x)$ is the Empirical CDF of the AMD representing the n degree of freedom system being analyzed. Where the results are from a Monte Carlo simulation of the measurement

error model with N samples. Specializing to $\varphi(F(x)) = 1$, the CVM test is then calculated by:

$$Q_k = \frac{1}{12N}\sum_{i=1}^{N}\left[\frac{2i-1}{2N} - F(\mathcal{M}^{(i)})\right]^2 \tag{81}$$

Sorting the Mahalanobis squared distance of the samples, $\mathcal{M}^{(i)}$, from the smallest to largest, $F\left(\mathcal{M}^{(i)}\right)$ can be obtained by:

$$F\left(\mathcal{M}^{(i)}\right) = erf\left(\sqrt{\frac{\mathcal{M}^{(i)}}{2}}\right) - \sqrt{\frac{2\,\mathcal{M}^{(i)}}{\pi}}e^{-\frac{\mathcal{M}^{(i)}}{2}} \tag{82}$$

Given a significance level α, one can derive a two-sided 100(1- α)% confidence interval for the distribution $\overline{\mathcal{M}}(n)$. As with the averaged Mahalanobis distance (AMD), the acceptable degree of the CVM metric is determined by defining a confidence level. Table 10 outlines the acceptable ranges of the CVM and AMD for a commonly selected confidence level for measurement models of dimension 3.

	90%	**95%**	**99%**	**99.9%**
AMD	[0.9655,1.0457]	[0.9578,1.0534]	[0.9427,1.0685]	[0.9106,1.1006]
CVM	[0,0.3430]	[0,0.46136]	[0,0.74346]	[0,1.16204]

Table 10. Confidence interval for Cramer–von Mises (CVM) [12] and Mahalanobis Distance (MD) for ∞ samples.

As described the Squared Mahalanobis Distance Metric and the Cramer–von Mises distribution matching test require the generation of an Empirical Distribution. In doing so, a measurement model using the calculated uncertainty of the radar and tracking error models is constructed, generating N observation samples about the nominal measurement. Under the assumption that each measurement variable is independent (non-correlated):
The navigation Error contribution, (considered only for SBSS platform), is given by:

$$\begin{Bmatrix} R_N = \sigma_{R_{NAV}}N \\ S_N = \sigma_{S_{NAV}}N \\ W_N = \sigma_{W_{NAV}}N \end{Bmatrix} \tag{83}$$

The tracking contribution is given by:

$$\begin{Bmatrix} r_T = r_0 + \sigma_{r_{TRK}}N \\ \epsilon_T = \epsilon_0 + \sigma_{\epsilon_{TRK}}N \\ \eta_T = \eta_0 + \sigma_{\eta_{TRK}}N \end{Bmatrix} \tag{84}$$

The total uncertainty about the object when tracked from the space-based platform is then described by:

$$\begin{Bmatrix} R_T = R_N + r_T\ cos(\eta_T)\,cos(\epsilon_T) \\ S_T = S_N + r_T\ cos(\eta_T)\,sin(\epsilon_T) \\ W_T = W_H + r_T\ sin(\epsilon_T) \end{Bmatrix} \tag{85}$$

Under the assumption the position of observation is well known and therefore the error is negligible, the total uncertainty from the ground station is:

$$\begin{Bmatrix} S_T = r_T cos(\eta_T) cos(\epsilon_T) \\ E_T = r_T cos(\eta_T) sin(\epsilon_T) \\ Z_T = r_T sin(\epsilon_T) \end{Bmatrix} \quad (86)$$

4. Simulation and Verification

4.1 Ground-Based Tracking Scenario

The aim of the first case studies is to apply the above framework for the typical scenario of RSO tracking from a radar ground station for the practical purpose of identification and assessment of a potential collision with an operational spacecraft (**Figure 30**). Typically ground-based tracking stations utilize the South East Zenith Topocentric Horizon Coordinate frame (SEZ). The SEZ coordinate system is defined for a given longitude and latitude at a local sidereal time and rotates with the site where the local horizon forms the fundamental plane. The S axis points due South from the site, The E axis points East from the site and the Z axis (Zenith) points radially outward from the site along the site position vector from the ECI origin.

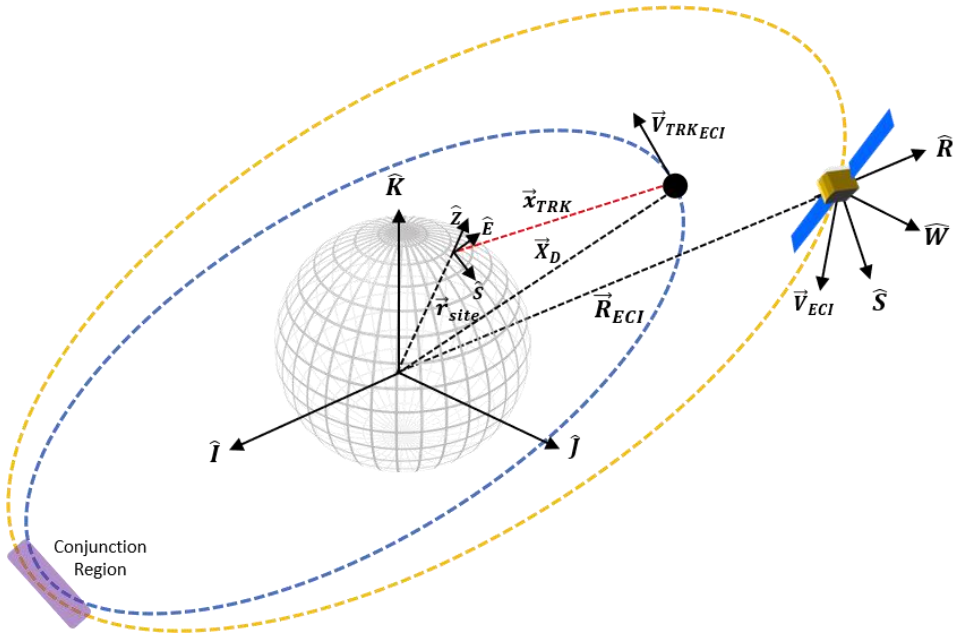

Figure 30. Illustration of ground-based tracking scenario and subsequent conjunction region with operational satellite.

The coordinate system is constructed using the site position vector, $\vec{r}_{SITE}$, in ECI frame:

$$\hat{\boldsymbol{Z}} = \frac{\vec{r}_{SITE}}{|\vec{r}_{SITE}|} \quad (87)$$

$$\hat{\boldsymbol{E}} = \hat{\boldsymbol{K}} \times \hat{\boldsymbol{Z}} \quad (88)$$

$$\hat{\boldsymbol{S}} = \hat{\boldsymbol{E}} \times \hat{\boldsymbol{Z}} \quad (89)$$

The transfer matrix between the RSW and ECI coordinate systems is then following:

$$M_{SEZ\rightarrow ECI} = \left[\widehat{\boldsymbol{S}}\ \widehat{\boldsymbol{E}}\ \widehat{\boldsymbol{Z}}\right] \tag{90}$$

Within the SEZ coordinate frame the tracked RSO range, azimuth and elevation (ρ, ϵ, η) and their derivates are measured where then by implementing the SITE-TRACK algorithm [28] the position $\vec{X}_{TRK}$ and the velocity $\vec{V}_{TRK}$ in the ECI frame can be determined.

$$\vec{X}_{TRK} = \vec{r}_{SITE} + M_{SEZ\rightarrow ECI}\begin{bmatrix}\rho cos(\eta)cos(\epsilon)\\ \rho\ cos(\eta)sin(\epsilon)\\ \rho\ sin(\eta)\end{bmatrix} \tag{91}$$

$$\vec{V}_{TRK} = M_{SEZ\rightarrow ECI}\ \vec{v}_{SEZ} + \vec{\omega}\ x\ \vec{X}_{TRK} \tag{92}$$

Where: $\vec{v}_{SEZ}$ is the velocity vector determined from observations at the site in SEZ coordinate frame and $\vec{\omega}$ is the Earth's rotation vector. Based on the calculated radar performance parameters using radar error equations (Equations (2), (4), (5)), it is then necessary to transform the TRK uncertainty $(\sigma_{r_{TRK}}, \sigma_{\epsilon_{TRK}}, \sigma_{\eta_{TRK}})$ into the ECI coordinate system, ${Q_{TRK}}_{CART}^{ECI}$ as described in Section 3.1. Assuming the velocity measurement error to be zero we obtain the following 3 × 3 Covariance matrix for each observation.

$${Q_{TRK}}_{CART}^{ECI} = (M_{SEZ\rightarrow ECI}\cdot D)\cdot {Q_{TRK}}_{SPH}^{SEZ}\cdot (M_{SEZ\rightarrow ECI}\cdot D)^T \tag{93}$$

$${Q_{TRK}}_{CART}^{ECI} = \begin{bmatrix}{\sigma_{x_{TRK}}}^2 & \sigma_{xy_{TRK}} & \sigma_{xz_{TRK}}\\ & {\sigma_{y_{TRK}}}^2 & \sigma_{yz_{TRK}}\\ sym & & {\sigma_{z_{TRK}}}^2\end{bmatrix} \tag{94}$$

Subject to a linearized propagation method, the dynamic evolution of the RSO uncertainty ${Q_{TRK}}_{CART}^{ECI}$ now be estimated. As this paper is focused on the sensor level analysis, the full derivation of this technique beyond scope and as such the reader is referred to [11] and [31] for this additional framework. As previously discussed, the propagation of uncertainty is a fundamental aspect of SSA, as it allows the determination of probability of collision between two RSO's if a close approach is predicted from each nominal RSO trajectory, a region known as the "Conjunction Region" is then defined. The covariance matrix's that describe the propagated position uncertainty of the tracked RSO $({Q'}_{TRK})$ and the spacecraft $({Q'}_{NAV})$ are then summed together and represented as an ellipsoid typically centered on the nominal position of the tracked (non-cooperative) RSO. Measurements are uncorrelated, variance and covariance terms can be summed directly [32].

$$Q_{TOT} = {Q'}_{TRK} + {Q'}_{NAV} \tag{95}$$

$$Q_{TOT} = \begin{bmatrix}{\sigma_x}^2 & \sigma_{xy} & \sigma_{xz}\\ & {\sigma_y}^2 & \sigma_{yz}\\ sym & & {\sigma_z}^2\end{bmatrix}^{ECI} \tag{96}$$

Following from reference REF Q_{TOT} now provides a convenient form to analyze the probability of collision between the tracked and operation RSO. **Figure 31** illustrates the concept of individual navigation and tracking uncertainty's volume and the resultant combined ellipsoid.

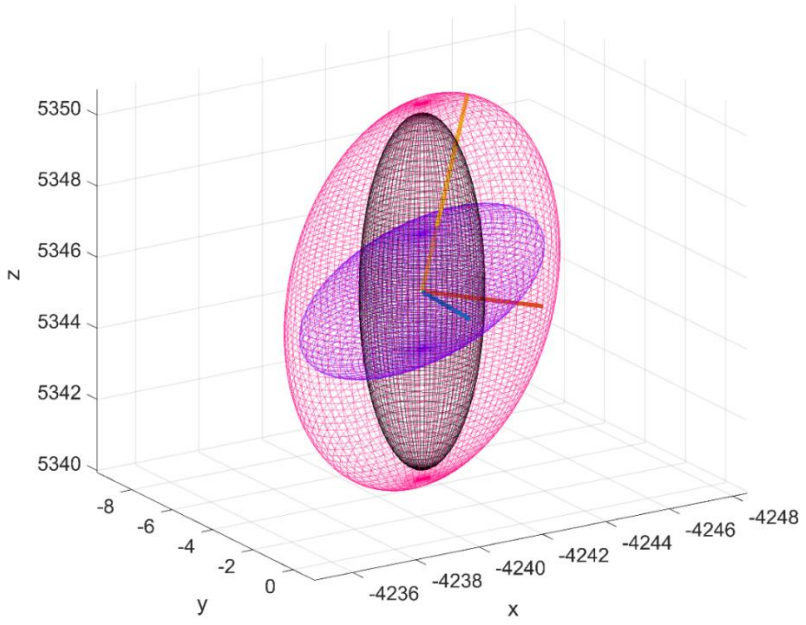

Figure 31. Conceptual illustration of navigation(purple) tracking(black), total uncertainty volume(magenta) and major(orange), semi-major(red) and minor axis (blue) of total uncertainty volume.

4.2 Space-Based Surveillance Scenario

Based on proposed MMW SBR systems and documented GPS system performance, we outline here a mathematical framework to combine tracking and navigation uncertainty with the aim providing a rigorous methodology to describe and analyze the position uncertainty of a tracked RSO from a SBSS Radar platform. As with the ground-based scenario, we focus on the case of representing uncertainty expressed in a common satellite coordinate system to a convenient Earth-Centred Inertial (ECI) reference frame as described in **Figure 32**.

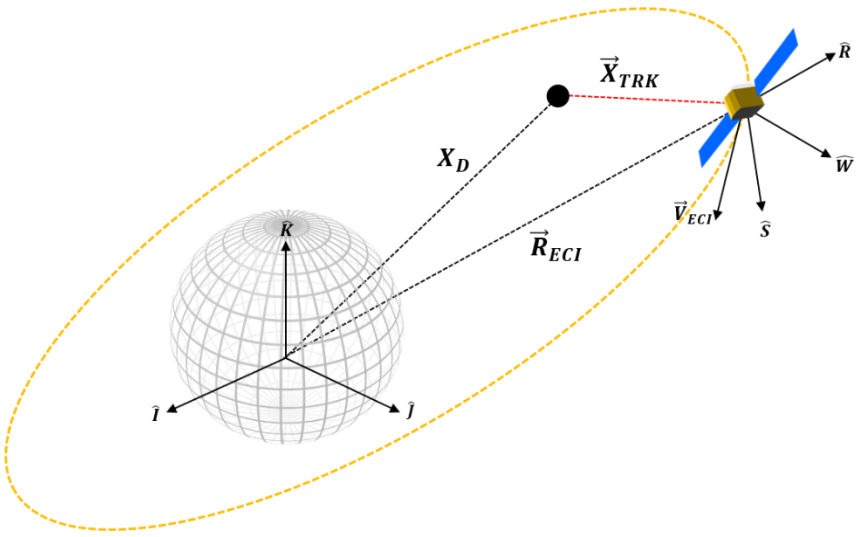

Figure 32: Reference geometry of the non-cooperative tracking and RSW coordinate system.

In this case, the RSW coordinate system is used for both navigation and tracking observations, where the MMW radar (TRK) and GNSS (NAV) system is assumed to be centered about the origin. The key symbols for this scenario are introduced in **Figure 33**.

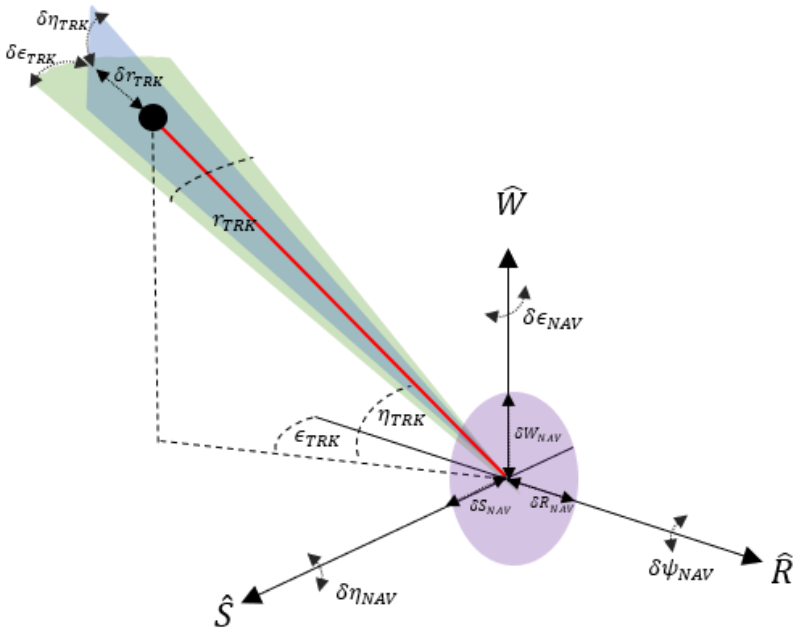

Figure 33: Space-based observation geometry and measurement deviations in RSW frame.

To quantify the total error about the RSO position, we reformulate the framework described in Section 2.2 as an Errors in-variable model following the Gauss–Helmert method [33,34]. In this case, we assume the attitude error of the spacecraft is zero ($\delta\epsilon_{NAV} = 0$, $\delta\eta_{NAV} = 0, \delta\psi_{NAV} = 0$). The generic Gauss–Helmert form consists in resolution of the following equation system:

$$\boldsymbol{F(X, l) = 0} \tag{97}$$

Where $\boldsymbol{X}$, $\hat{\boldsymbol{l}}$ are estimated parameters and observation vector respectively. The linearized form of the previous equation is:

$$\boldsymbol{A\delta + Br + w = 0} \tag{98}$$

Where $\boldsymbol{A} = \frac{\boldsymbol{\partial F}}{\boldsymbol{\partial \hat{X}}}$ and $\boldsymbol{B} = \frac{\boldsymbol{\partial F}}{\boldsymbol{\partial l}}$ are the matrix of partial derivates with respect to $\boldsymbol{X}$, $\boldsymbol{l}$ and $\mathbf{w}$ is the misclosure vector. $\boldsymbol{\delta}$ and $\boldsymbol{r}$, the parameter and observation correction vector respectively, are:

$$\begin{aligned} \hat{\boldsymbol{\delta}} &= -(\boldsymbol{A^T M A})^{-1}\boldsymbol{A^T M w} \\ \hat{\boldsymbol{r}} &= -\boldsymbol{C_r B^T M(A\delta + w)} \end{aligned} \tag{99}$$

Where $\boldsymbol{M} = (\boldsymbol{BC_rB^T})^{-1}$ and $\boldsymbol{C_r}$ is the covariance matrix of the observations. We obtain the covariance matrix of parameters:

$$C_{NAV+TRK} = (\boldsymbol{A^T M A})^{-1} \tag{100}$$

Equation (43) is then:

$$\boldsymbol{F(X, l) = X_D - M_{RSW\rightarrow ECI} X_{TRK} - R_{ECI} = 0} \tag{101}$$

Where:

$\boldsymbol{X_D} = \begin{bmatrix} X_D^{ECI} \\ Y_D^{ECI} \\ Z_D^{ECI} \end{bmatrix}$ and $\boldsymbol{R}_{ECI} = \begin{bmatrix} X_h^{ECI} \\ Y_h^{ECI} \\ Z_h^{ECI} \end{bmatrix}$ are the RSO and spacecraft position in ECI frame

$\boldsymbol{X}_{TRK} = \begin{bmatrix} -r_{TRK}cos(\epsilon_{TRK})cos(\eta_{TRK}) \\ r_{TRK}cos(\epsilon_{TRK})sin(\eta_{TRK}) \\ r_{TRK}sin(\epsilon_{TRK}) \end{bmatrix}$ is the nominal position of the target in RSW frame.

$\boldsymbol{l} = [r_{TRK}, \epsilon_{TRK}, \eta_{TRK}, x_{NAV}, y_{NAV}, z_{NAV}]^{\boldsymbol{T}}$ is vector of estimated observations, and

$$\boldsymbol{C_r} = \begin{bmatrix} \sigma_{r_{TRK}}^2 & & & & & \\ & \sigma_{\epsilon_{TRK}}^2 & & & & \\ & & \sigma_{\eta_{TRK}}^2 & & & \\ & & & {\sigma_{x_{NAV}}}^2 & \sigma_{xy_{NAV}} & \sigma_{xz_{NAV}} \\ & & & \sigma_{yx_{NAV}} & {\sigma_{y_{NAV}}}^2 & \sigma_{yz_{NAV}} \\ & & & \sigma_{zx_{NAV}} & \sigma_{zy_{NAV}} & {\sigma_{z_{NAV}}}^2 \end{bmatrix} = \begin{bmatrix} Q_{TRK_{SPH}} & \\ & Q_{TRK}{}_{CART}^{ECI} \end{bmatrix}$$

is the covariance matrix of observations.

The assumption is made that all navigation and tracking observations errors are independent, so covariance terms between the 2 observation sets in the matrix $\boldsymbol{C_r}$ are set to zero. However, covariance terms between navigation uncertainty exist due to the transformation from the RSW to ECI coordinate frame described by equation 45. With, $A_{(3\times3)} = \mathbb{1}$ the covariance matrix of observation is then computed by:

$$\boldsymbol{C}_{NAV+TRK\,(3\times3)} = (\boldsymbol{B}\boldsymbol{C_r}\boldsymbol{B^T}) \tag{102}$$

4.3 Space-Based Optical sensor scenario

Since the utilization of radar technology has been proposed but it has different type of limitation, optical sensor appears to be a viable solution for space debris surveillance. A mathematical framework will be described, and it will be able to quantify the position uncertainty of a tracked RSO from a formation of multiple space-based using passive optical sensors. The platforms, involved in this formation, detect and track common target by using the concept of multiple point of view observations solving the triangulation technique. The proposed RSO surveillance mission uses multiple space-based distributed in several Sun-synchronous orbits, located in order to allow for a complete worldwide coverage and multiple observation of space debris orbiting in LEO. It is imperative to develop a coordination architecture within at least two spacecrafts would be able to perform the tasks. Therefore, the basic tasks that can be carried on all or part of the team members include [67]:

- Detecting of the debris
- Tracking of the debris
- Identification of the neighboring satellites
- Gathering and updating information about detected debris

The system should address and be robust against some relevant issues related to the space environmental and working conditions, such as [67]:

- Non-optimal illumination conditions
- Sensor degradation
- False target detections
- Variability of the inter-satellite communication link
- Timing problem

For this thesis, a formation of two sensor platforms will be analyze. As the radar scenario, we focus on representing the uncertainty from the satellite reference frame (RSW) to a common reference frame. In this case, the RSW coordinate system is used for both navigation and tracking observations, where the GNSS system and the optical observation is assumed to be centered about the origin. The camera is rigidly attached to the body frame: no gimbal mechanisms are considered in this preliminary design. The camera optical axis is aligned with the satellite R axis and the image plane XY is parallel to the WS satellite body plane. The reference geometry and the key symbols for this scenario are introduced in **Figures 34** and **35**.

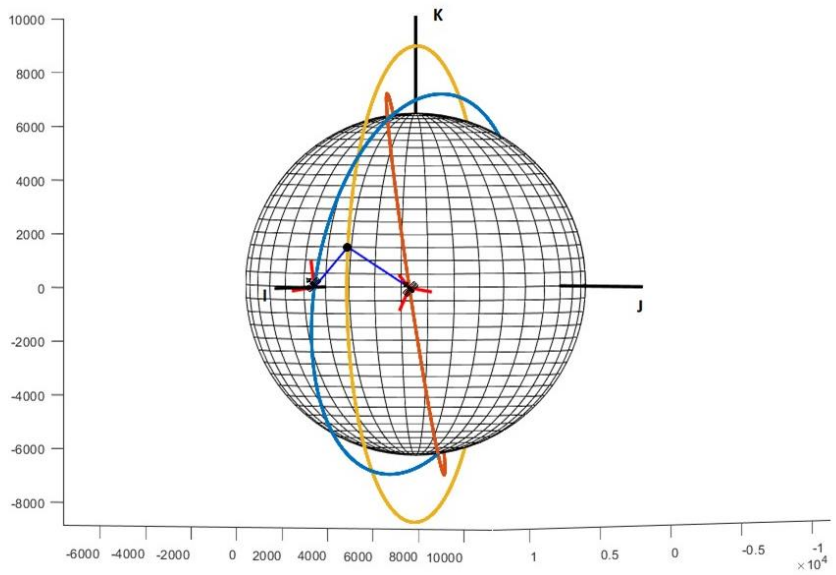

Figure 34: Reference geometry of the non-cooperative tracking and RSW coordinate system.

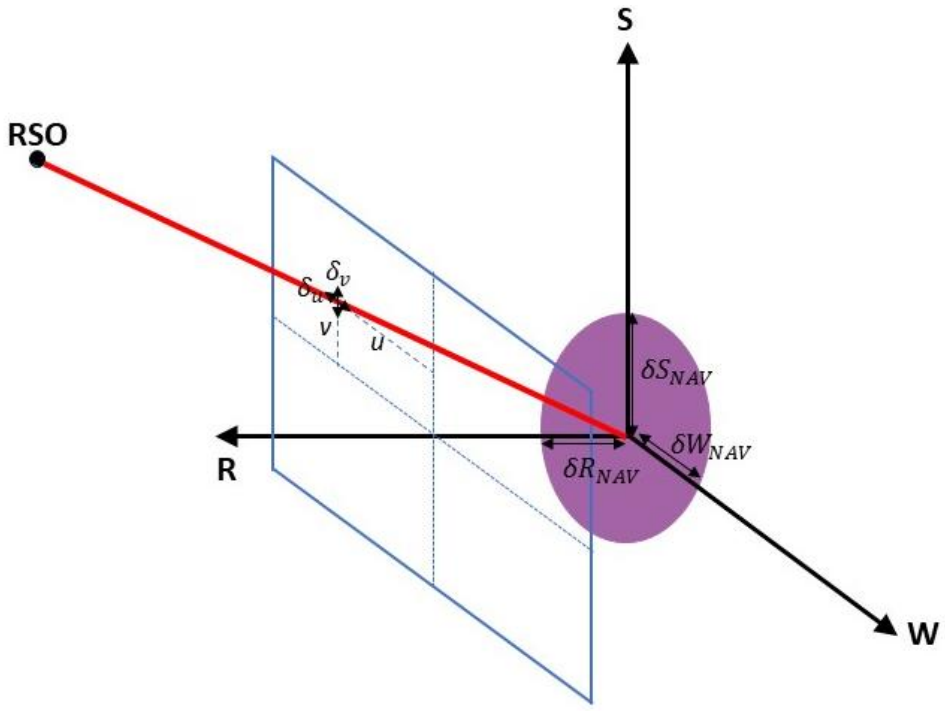

Figure 35: measurement deviations in RSW frame.

To quantify the total error about the RSO position, we need to use the framework described in **section 3.2**, following the Gauss-Helmert method. Firstly, it is necessary to express the two platforms position and the direction of the viewed target, the pointing angles, from each sensor into a common reference frame.

Then, we need to solve the following equation:

$$\boldsymbol{F}(\boldsymbol{X}, \boldsymbol{l}) = \boldsymbol{0} \tag{103}$$

Where $\boldsymbol{X}$, $\hat{\boldsymbol{l}}$ are estimated parameters and observation vector respectively.

That, in this case, can be written:

$$\begin{cases} x_t - \dfrac{x_2\, tan(\theta_1) - x_1\, tan(\theta_2) + (y_1 - y_2)tan(\theta_1)tan(\theta_2)}{tan(\theta_1) - tan(\theta_2)} = 0 \\ y_t - \dfrac{y_1\, tan(\theta_1) - y_2\, tan(\theta_2) + (x_2 - x_1)}{tan(\theta_1) - tan(\theta_2)} = 0 \\ z_t - \dfrac{r_1 tan(\varphi_1) + z_1 + r_2 tan(\varphi_2) + z_2}{2} = 0 \end{cases} \quad (104)$$

Where:

- (x_1, y_1, z_1) and (x_2, y_2, z_2) are the two platform positions in ECI reference frame
- (x_t, y_t, z_t) is the RSO position in ECI reference frame
- (θ_1, φ_1) and (θ_2, φ_2) are the azimuth and elevation angles of the RSO from each sensor platforms

Instead, the error analysis, described in **section 3.2**, requires transforming also the uncertainty position of the two sensors from RSW into ECI reference frame by using the equation 45:

$$Q_{NAV}{}_{CART}^{ECI} = M_{RSW \to ECI}\, Q_{NAV}{}_{CART}^{RSW} \cdot M_{RSW \to ECI}{}^{T} \quad (45)$$

Also in this case, we assume the attitude error of the spacecraft is zero ($\delta\epsilon_{NAV} = 0$, $\delta\eta_{NAV} = 0, \delta\psi_{NAV} = 0$).

For the sensor accuracy, the onboard camera provides information about the location of the object in the image plane $[\tilde{u}\ \tilde{v}]$. Such positioning includes the noise, so the equation become:

$$\begin{bmatrix} \tilde{u} \\ \tilde{v} \end{bmatrix} = \begin{bmatrix} u \\ v \end{bmatrix} + \begin{bmatrix} \delta_u \\ \delta_v \end{bmatrix} \quad (105)$$

Where δ_u and δ_v are the noise elements along the u and v axes of the image plane respectively

The noise elements can be modeled with a zero-mean Gaussian distribution and a covariance matrix given by:

$$\boldsymbol{C_{TRK}} = E([\delta_u\ \delta_v]^T[\delta_u\ \delta_v]) = \begin{bmatrix} \sigma_u^2 & 0 \\ 0 & \sigma_v^2 \end{bmatrix} \quad (106)$$

Where σ_u^2, σ_v^2 are the variances of the errors, expressed in pixel, along the two coordinate axes. We can now transform σ_u^2 and σ_v^2 into variances of error expressed in rad:

$$\begin{aligned} \sigma_\theta &= \frac{\sigma_u \rho_u}{2\, f} \\ \sigma_\varphi &= \frac{\sigma_v \rho_v}{2\, f} \end{aligned} \quad (107)$$

Where ρ_u and ρ_v are the width and the height of each pixel and *f* the focal length

So, the covariance matrix of the observation can be written:

$$\boldsymbol{C_r}=\begin{bmatrix} \sigma_{x_1}^2 & \sigma_{xy_1} & \sigma_{xz_1} & & & & & & & \\ \sigma_{xy_1} & \sigma_{y_1}^2 & \sigma_{yz_1} & & & & & & & \\ \sigma_{xz_1} & \sigma_{yz_1} & \sigma_{z_1}^2 & & & & & & & \\ & & & {\sigma_{\theta_1}}^2 & & & & & & \\ & & & & {\sigma_{\varphi_1}}^2 & & & & & \\ & & & & & \sigma_{x_2}^2 & \sigma_{xy_2} & \sigma_{xz_2} & & \\ & & & & & \sigma_{xy_2} & \sigma_{y_2}^2 & \sigma_{yz_2} & & \\ & & & & & \sigma_{xz_2} & \sigma_{yz_2} & \sigma_{z_2}^2 & & \\ & & & & & & & & {\sigma_{\theta_2}}^2 & \\ & & & & & & & & & {\sigma_{\varphi_2}}^2 \end{bmatrix} \quad (108)$$

The assumption is made that all navigation and tracking observations errors are independent, so covariance terms between the 2 observation sets in the matrix $\boldsymbol{C_r}$ are set to zero. However, covariance terms between navigation uncertainty exist due to the transformation from the RSW to ECI coordinate frame described by **equation 45**. With $A_{(3\times3)} = \mathbb{1}$, the covariance matrix of observation is then computed by:

$$\boldsymbol{C}_{NAV+TRK\,(3\times3)} = (\boldsymbol{B}\boldsymbol{C_r}\boldsymbol{B^T}) \quad (109)$$

Where: $\boldsymbol{B} = \frac{\boldsymbol{\partial F}}{\boldsymbol{\partial l}}$ is the matrix of the partial derivates respect $\boldsymbol{l}$

5. Results

5.1 Radar Results

The aim of both Radar scenarios was to demonstrate an effective framework for measurement uncertainty analysis while gaining a deeper understanding on the limits of a normally distributed representation of the uncertainty of the measurement models. In the first scenario, radar design parameters were selected based on ground-based radar tracking stations in the SSA SST network where in the second case radar parameters were selected from proposed spaceborne MMW Radar designs for larger orbiting platforms such as the ISS. As described in **Section 4.2**, the second case implements an error in variables model under a Gauss–Helmert formulation to combine both tracking the navigation measurements when determining the total position uncertainty of the tracked RSO. In doing so, navigation measurements are assumed to be provided by an on-board GNSS system where corresponding uncertainty values are taken from a LEO GPS accuracy experiment found in the literature [35]. **Table 11** outlines the specific radar parameter and nominal tracking measurements (azimuth and elevation) values for both cases and the spacecraft orbital parameters (at measurement epoch) and associated uncertainty values within the RSW frame. To reflect the advantages of spaceborne MMW radar <10 cm RSO size was selected for the simulation, as opposed to the larger debris sizes (>10 cm) which have been chosen for the ground station scenario.

Table 11. Ground and Space-based tracking scenario inputs.

Spacecraft Position	**a= 6829km**	**e =0.00001**	**i = 51.6°**	**ω = 90°**	**Ω = 90°**
Navigation Error					
Radial (R) $\sigma_{R_{NAV}}$			13.81m		
In-Track (S) $\sigma_{S_{NAV}}$			4.15m		
Cross-Track (W) $\sigma_{W_{NAV}}$			3.0m		
Nominal Tracking Angle	**Space-Based Radar**			**Ground-Based Radar**	
ϵ_{TRK}	45°			45°	
η_{TRK}	45°			45°	
Fixed Radar Parameters					
Frequency	95 GHz (W band)			442 MHz (UHF)	
Peak transmit power	1200 W			36 MW	
Beamwidth	0.2°			1.3°	
Aperture Dimension	1.0m			58.0 m	
Noise Figure	4.5 dB			4.5dB	
Radar pulse duration	1 μs			1 μs	
Transmit antenna Gain	58 dBi			48dBi	
Varied Parameters					
Debris Diameter	1, 3, 6 cm			10,20,30cm	
Range to Target r_{TRK}	1:60 km			1:850 km	

To test the covariance realism of the total position uncertainty the RSO the average Mahalanobis distance metric and Cramer–von Mises test statistic outlined in **Section 3.3** is computed. Adapting the test procedure outlined in [10] for a sensor level analysis, the following steps are performed for both cases:

- Define a range to target and debris size, calculate the performance of the radar system and fuse the tracking + navigation errors using the approach outline in **Section 3.1**
- Generate N Monte Carlo points based on the measurement model performance as described in **Section 3.3**. (10,000 points were chosen in the case of these simulations)
- Calculate the corresponding average Mahalanobis distance metric (AMD) and Cramer–von Mises (CVM) goodness of fit statistic.
- Repeat steps 1–3 for every range to target for each RSO size.
- Plot the averaged uncertainty metric (AMD) and the Cramer–von Mises test statistic versus range to target for each tracked RSO size
- Determine the range to target when the averaged metric and the Cramer-von Mises test statistic first pierce a pre-defined confidence level interval (**Table 10**) – and declare that the covariance realism has broken down under the corresponding sensor performance.

Figure 36 and **37** displays the results of the above uncertainty realism test procedure which can be interpreted as follows: The calculated degree of the CVM test and AMD metric are plotted for each range to target as well as the confidence interval for each. Until the first point of intersect from either realism test and the corresponding confidence interval, the uncertainty distribution can be assumed to represent the calculated RSO covariance matrix under the chosen level of confidence. In both the ground and space-based cases, a confidence level of 99% was chosen arbitrarily. Both figures demonstrate that for all tracked RSO sizes, the CVM test statistic with the corresponding confidence interval provides a more restrictive statistical measure, when compared against the first-moment AMD metric. This is not a surprising result as the CVM test statistic is determined from the empirical CDF measurement model, giving more indication on the actual shape, size and orientation of the distribution. In turn the CVM test can distinguish finer discrepancies between the empirical (CDF) and the theoretical uncertainty distribution (covariance) when compared to the AMD metric. **Table 12** outlines the difference in the range to target when between the CVM test statistic and AMD metric at the 99% confidence interval.

Figure 36. Covariance realism of theoretical uncertainty volume as a function of range for Ground-Based radar

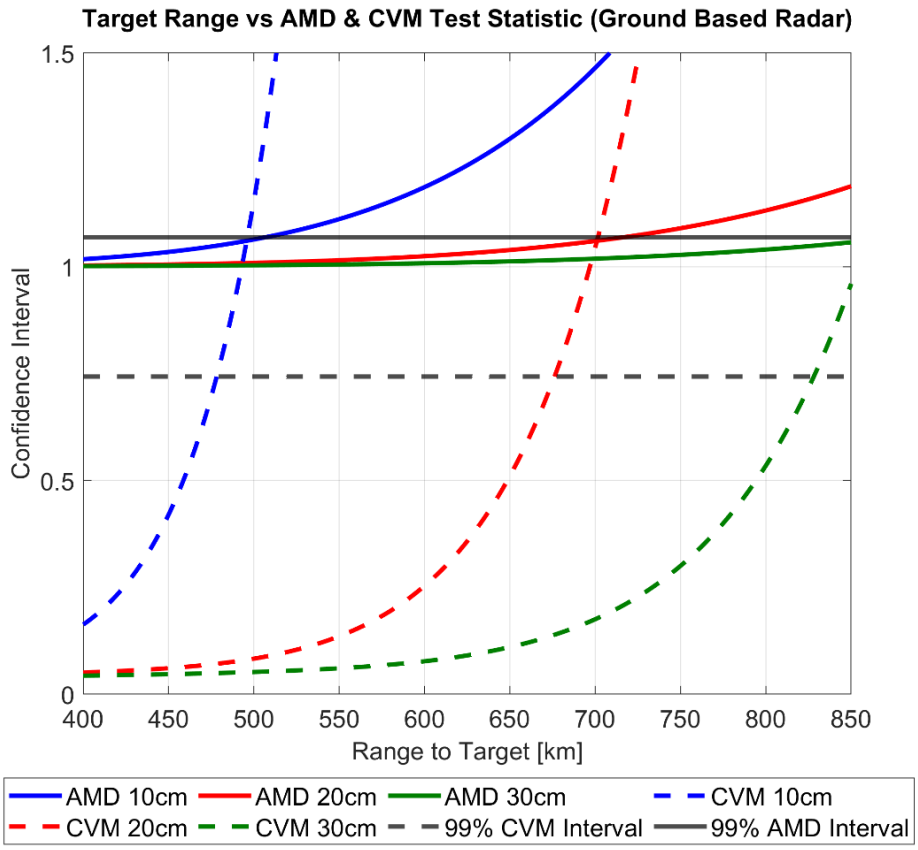

Figure 37. Covariance realism of theoretical uncertainty volume as a function of range for Space-Based Radar.

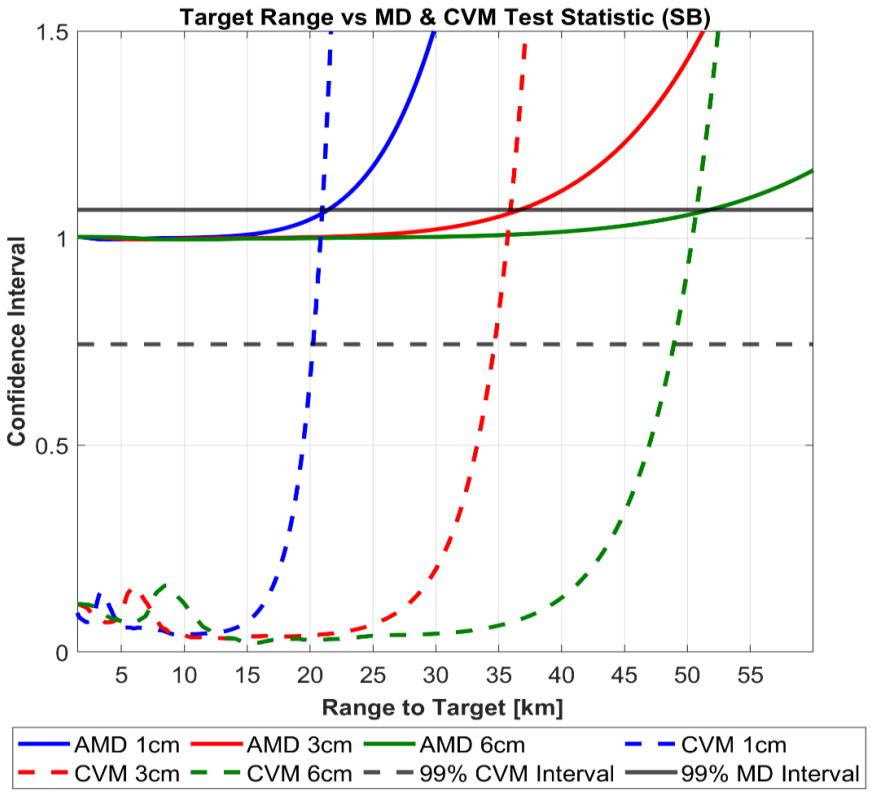

Table 12. Max Range-to-Target for 99% Average Mahalanobis Distance (AMD) and CVM Covariance Realism Test Statistic.

	Space-Based Tracking			**Ground-Based Tracking**		
RSO Size	**1cm**	**3 cm**	**6 cm**	10 cm	20 cm	30 cm
AMD range [km]	21.393	36.689	51.825	505.54	716.61	876.80
CVM range [km]	20.027	34.618	48.958	479.15	677.03	827.80
Δ range to target [km]	1.115	2.071	2.867	26.38	39.57	49

Due to the significant impact on the calculated SNR of the radar system, assessing the covariance realism in relation to the specific range to target and debris size provide a practical relationship to defining an acceptable magnitude of measurement errors. **Figures 38** and **39** illustrate this relationship for the ground and space-based case, where the magnitude of range and angular errors and corresponding 99% CVM interval are plotted against the range-to-target for each debris size.

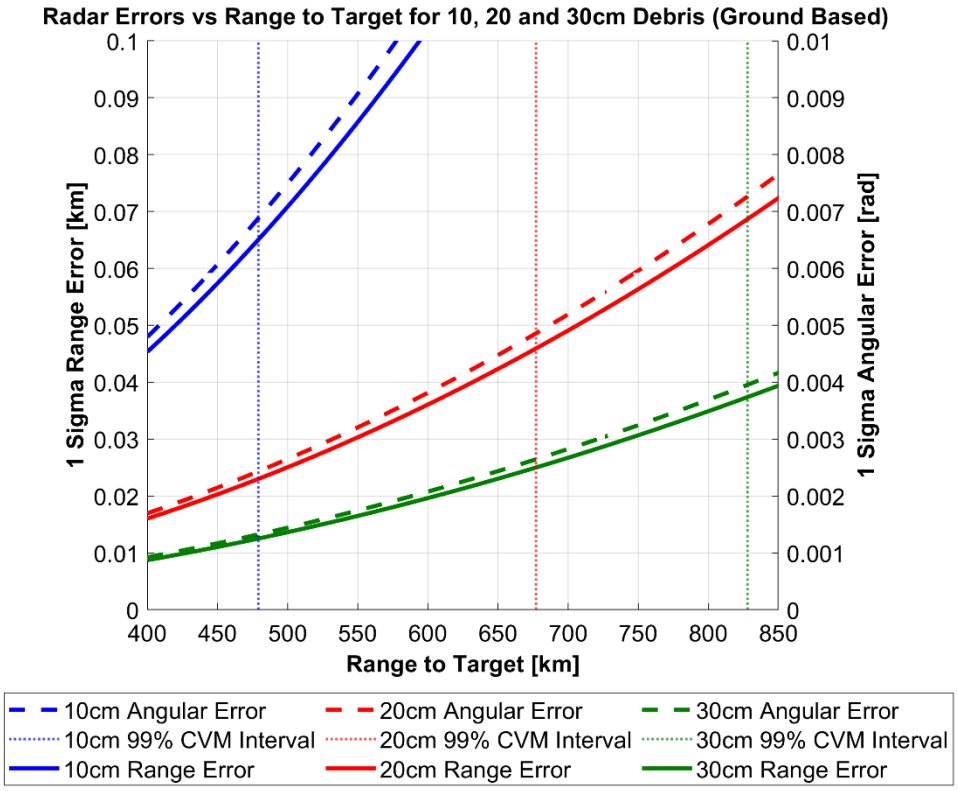

Figure 38. Ground Based Radar range and angular errors as a function of range to target

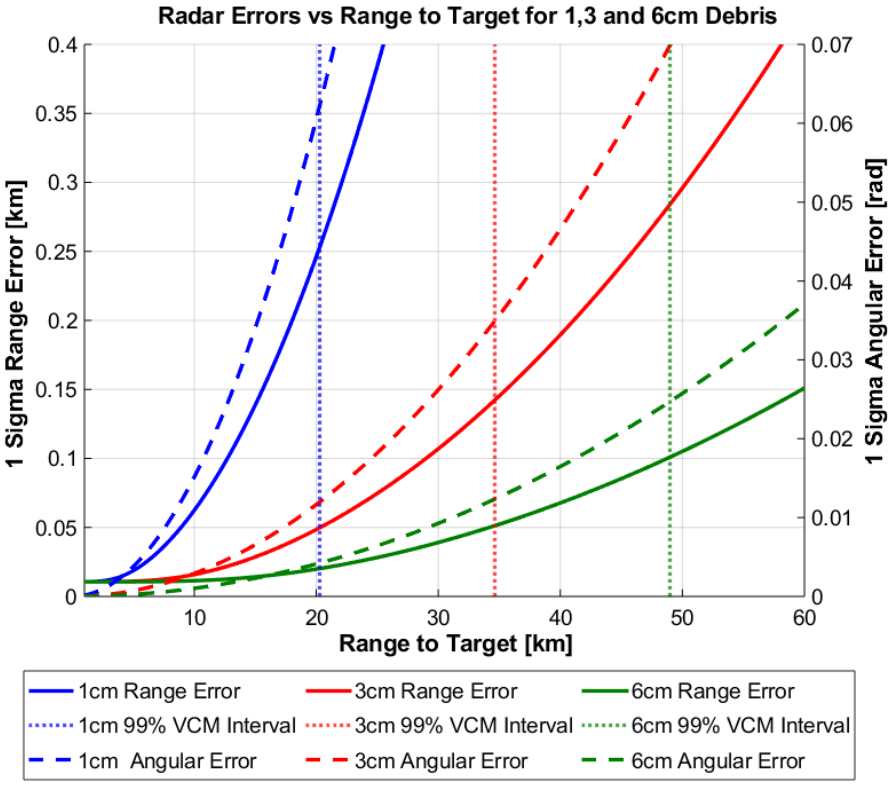

Figure 39. Space Based Radar range and angular errors as a function of range to target.

Mathematically, the confidence interval represents the point at which the original curvilinear distribution described by the radars spherical uncertainty can no longer be truthfully represented as rectilinear covariance within the cartesian ECI system. To illustrate this point further; **Figure 40a**) shows the generation of Monte Carlo points used to generate the empirical distribution for the 6cm RSO at the 99% CVM confidence interval for the 6cm debris size. The calculated Cartesian covariance matrix inflated to 3 sigma is then overlaid as an ellipsoid centered about the nominal RSO position. As expected, the corresponding contour map (**Figure 40b**), illustrates that the Monte Carlo points conform to a rectilinear Gaussian distribution and therefore the corresponding uncertainty can be represented in terms of covariance within the ECI cartesian frame. Conversely, **Figure 40c, d** illustrate the distribution corresponding to range to 6cm target of far-beyond the 99% CVM confidence interval. The distribution is now morphed from an ellipsoidal shape to a "bananoid", a curvilinear gaussian distribution inherent to the radar measurement uncertainty model. Although this demonstrates the extreme case, meaning practically that the radar would not be used under these conditions due to the large uncertainty of the measurements, the figures aims to show physically what it means when the distribution becomes non-gaussian at the sensor level (in the rectilinear sense) and therefore cannot be described in terms of cartesian covariance.

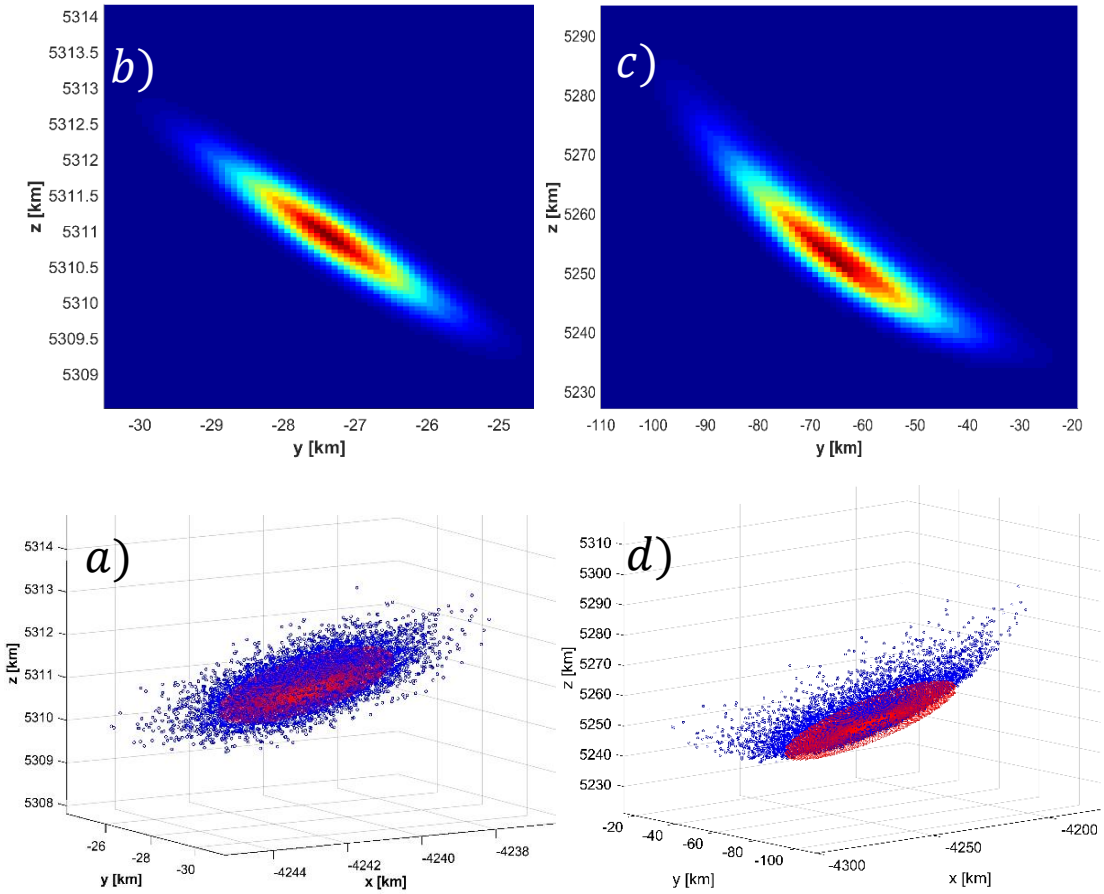

Figure 40. Monte Carlo generated distribution and corresponding contour maps for the 6cm debris. Clockwise from bottom left: (**a**) 99%CVM CI Monte Carlo distribution (**b**) 99%CVM Contour Map, (**c**) >>99% CVM Confidence Interval Contour Map (**d**) >>99% CVM Confidence interval Monte Carlo distribution.

As previously highlighted, the importance of quantifying uncertainty at the sensor level is to meet the required assumptions of covariance realism for SSA activities such as orbit determination and uncertainty propagation for RSO collision probability analysis and subsequent avoidance activities. In effect, covariance realism at the sensor level provides means of covariance "fidelity" to these processes. Previously published studies on covariance realism for orbital propagation demonstrate that the initial AMD and CVM metric should tend unity and (1/12k) respectively to demonstrate that a large enough Monte Carlo sample size of the initial covariance matrix (of RSO position uncertainty) has been taken. Nonetheless, the sensor level analysis performed in this thesis show that the initial covariance matrix used for these analyses may, in fact, vary in its actual realism/gaussianity if its intrinsic observation uncertainties have been mapped from its original coordinate system. For example, if an observation is taken under a certain tracking performance (in the case of this paper, RSO size and range-to-target), the subsequent covariance goodness of fit determined by the CVM test will lay somewhere along plot as shown in **Figures 36** and **37**. Analysis of the effect of varying gaussianity as inputs to typical SSA analysis (orbit determination, probability of collision) is beyond the scope of this paper and will be addressed in future research.

Turning attention now specifically to the second case of an SBSS platform. Using the Gauss–Helmert errors in variables framework a measurement model was produced that combines both navigation and tracking errors to generate a position uncertainty of the tracked RSO. We are interested in identifying the influence of the navigation error on the total position uncertainty and any effect on the covariance realism tests described previously. In doing so, plotting the range to target against the ratio between NAV+TRK (Q_{TOT}) and TRK (Q_{TRK}) uncertainty provides an indication of the total effect of the navigation error on the total uncertainty of the RSO. This is done by taking the eigenvalues of each respective covariance matrix (Q_{TOT}, Q_{TRK}) and summing them in an RSS manner, where the ratio between the two is then calculated.

$$TOT_{RSS} = \sqrt{\lambda_{1_{Q_{TOT}}} + \lambda_{2_{Q_{TOT}}} + \lambda_{3_{Q_{TOT}}}} \tag{110}$$

$$TRK_{RSS} = \sqrt{\lambda_{1_{Q_{TRK}}} + \lambda_{2_{Q_{TRK}}} + \lambda_{3_{Q_{TRK}}}} \tag{111}$$

From Figure 12a, it is clear the navigation error uncertainty has a strong influence on the total error uncertainty volume at close target ranges, however as the range increases the ratio between the two uncertainty volumes decreases asymptotically to 1. This result is expected as the navigation error is assumed fixed during observation however the calculated radar performance is dynamic and heavily dependent on the range to target. Not surprisingly, **Figure 41** demonstrates that navigation error has a significantly larger influence when a higher performance radar configuration is used, which in the case of the SNR dependent error corresponds to a larger size RSO being tracked. **Figure 41 a,b,c** graphically illustrates the influence of navigation uncertainty error on the total uncertainty size and orientation at the 10, 15, 20 km range to a 6cm target. At each range value, the navigation (NAV), tracking (TRK) and total (NAV+TRK) are represented as magenta, black and purple respectively. Regarding the effect of navigation uncertainty has the covariance realism, we can see that that the navigations uncertainty region of influence as defined by the ratio between TOT_{RSS} and TRK_{RSS} asymptotes to unity well before the range to target of the corresponding confidence interval. This indicates that under these specific simulation parameters the navigation error is not a limiting factor in maintaining gaussianity assumptions. However, on referring to **Figure 37**, it is shown that under close range where the navigation error is a dominant, oscillations of the CVM test occur for all debris sizes. Further research will address these findings and aim to address under what conditions could be detrimental to covariance realism.

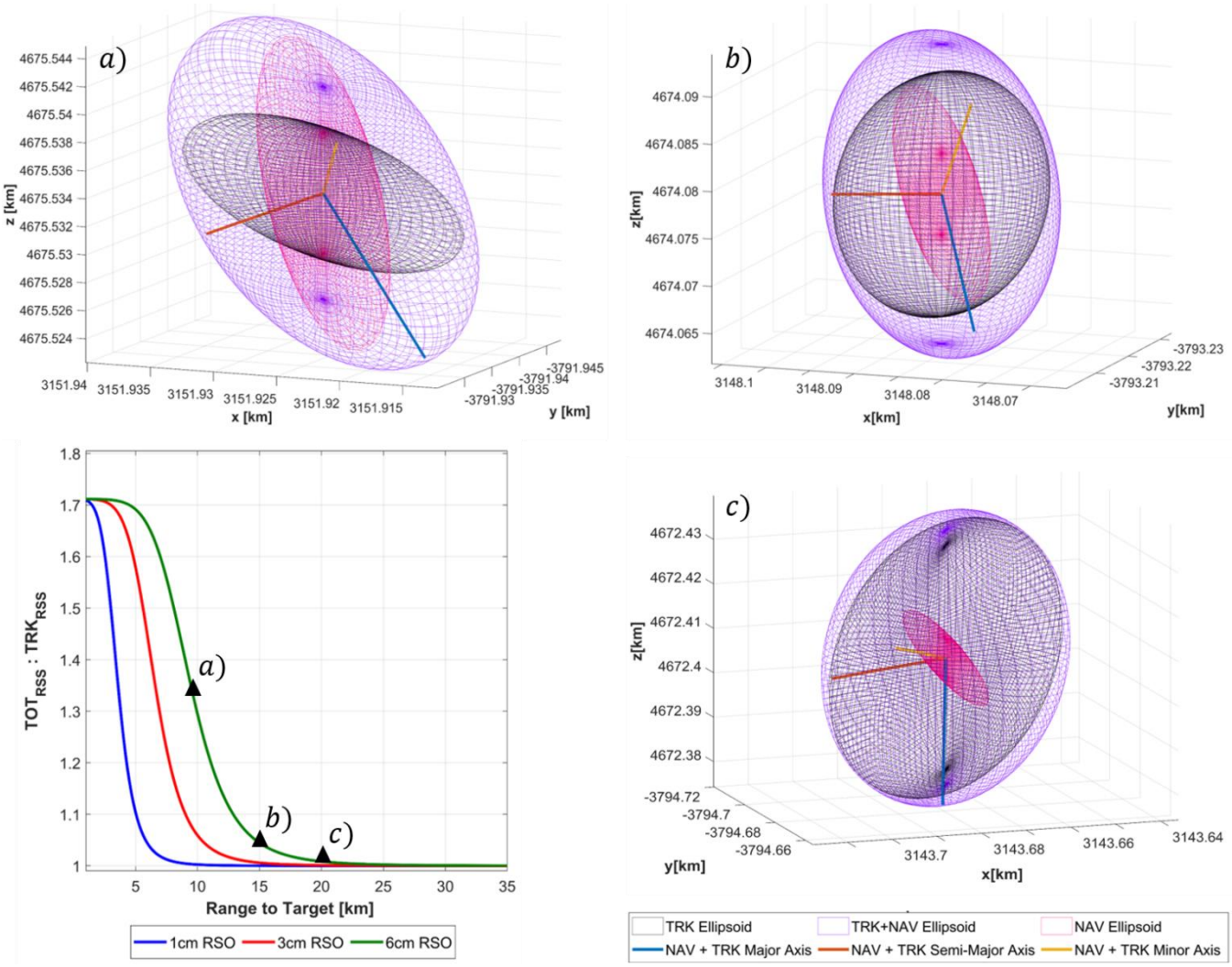

Figure 41: Effect of Navigation errors on total RSO uncertainty of tracked debris (clockwise from top right:). **a**) 10 km **b**) 15 km, **c**) 20 km range to target. In each figure the magenta, black and purple ellipsoids represent the Navigation, Tracking, and Total (NAV+TRK) uncertainty volumes respectively.

The aleatoric benefits of the presented framework and covariance realism studies are quite clear – by accurately modelling all prominent sources of error that contribute to RSO uncertainty a realistic uncertainty regarding the position of an RSO is determined (Parameter value uncertainty). Additionally, by addressing under what specific sensor performance RSO uncertainty (gaussian) assumptions maintain realism, Model-Based Uncertainty is also explicitly quantified providing both a top down and bottom up methodology to sensor performance requirements.

5.2 Optical Results

The aim of this scenario is to demonstrate an effective framework, by using passive optical sensor platforms, for measurement uncertainty analysis while gaining a deeper understanding on the limits of a normally distributed representation of the uncertainty of the measurement models. In this scenario, the passive optical sensor design parameters were selected based on a typical Star Tracker, device used for attitude determination. For the tracking error, we assume that all systematic errors in the device are taken into account while processing and they are negligible after the calibration. In this preliminary design, only the random error will be considered. As described in **section 4.3**, to combine both tracking and navigation measurements when determining the total position uncertainty of the tracked RSO, a model based on the Gauss-Helmert formulation has been implemented. As the radar scenario, navigation measurements are assumed to be provided by an on-board GNSS system. **Table 13** outlines the specific optical parameters of the device and the uncertainty spacecraft position values within the RSW frame.

Navigation Error	
Radial (R) $\boldsymbol{\sigma_{R_{NAV}}}$	12 m
In-Track (S) $\boldsymbol{\sigma_{S_{NAV}}}$	5.0 m
Cross-Track (W) $\boldsymbol{\sigma_{W_{NAV}}}$	5.0 m
Fixed Parameters	
Lens Diameter **D**	70 mm
Focal length $\boldsymbol{f}$	40 mm
CCD Pixel Size $\boldsymbol{\mu}$	5 μm
Albedo $\boldsymbol{\alpha}$	0.1
Quantum Efficiency **q**	0.4
Field of view **(FOV)**	5° x 5°
CCD array	1000 x 1000
Tracking Error (3σ)	
Noise Pixel ($\boldsymbol{\sigma_u}$, $\boldsymbol{\sigma_v}$)	66 μrad (1.1 pixel)

Table 13: Space-based tracking scenario inputs using optical sensor

For this scenario, we need to do some assumptions:

- The RSO is in the field of view (FOV) of both camera sensors during the tracking period
- The RSO has a visual magnitude value acceptable for the considered optical sensors during the tracking period
- No timing errors
- At this stage, the sizes of the RSO aren't considered

As the Radar scenario, to test the covariance realism of the total position uncertainty of the RSO the average Mahalanobis distance metric and Cramer–von Mises test statistic, outlined in **Section 3.3**, is computed. Adapting the test procedure outlined in [10] for a sensor level analysis, the following steps are performed for both cases:

- Define the orbital parameters of two SBSS and a RSO and decide a period of tracking, expressed in second.
- Calculate the performance of the optical system and fuse the tracking + navigation errors using the approach outline in **Section 3.2**
- Generate N Monte Carlo points based on the measurement model performance as described in **Section 3.3**. (10,000 points were chosen in the case of these simulations)
- Calculate the corresponding average Mahalanobis distance metric (AMD) and Cramer–von Mises (CVM) goodness of fit statistic.
- Repeat steps 2–4 for every tracking second.
- Plot the averaged uncertainty metric (AMD) and the Cramer–von Mises test statistic versus tracking time, corresponding on different position of three objects
- Determine the tracking time when the averaged metric and the Cramer-von Mises test statistic first pierce a pre-defined confidence level interval (**Table 10**) – and declare that the covariance realism has broken down under the corresponding sensor performance.

Considering for this scenario two Space-Based sensors and a RSO orbiting around the Earth, at this stage, we have decided to divide the analysis in two sub-case:

1. The first analysis has been done with two SBSS having a fixed position during their Sun-Synchronous orbit and the RSO orbiting in a known orbit
2. The second analysis has been done with the RSO having a fixed position and two SBSS following a Sun-Synchronous orbit.

5.2.1 First case

The first case wants to analyze how the orbital plane separation angle, defined as the angular difference of platforms orbital plane, influence the sensor performance and the RSO position uncertainty. The **table 14** shows the orbital parameters of the two sensor platforms that follow a Sun-synchronous trajectory. In this preliminary stage, we decided to fix their positions, near to an equatorial latitude. Instead the space object has a known orbit based on the concentration debris study, described on **figure 6** and **7**. Moreover, we decided to analyze the uncertainty position changing the RAAN **Ω** of the second sensor platform. Therefore, the two Space-Based will have an orbital plane separation angle of 20°, 30° and 45°.

Orbital Parameters	Sensor 1	Sensor 2	RSO
Semi-Major Axis, **a**	7171 Km	7171 Km	7621 Km
Eccentricity, **e**	0	0	0
Inclination, **i**	98.5621°	98.5621°	100.6535°
Right Ascension of Ascending Node (RAAN), **Ω**	0°	[20°, 30°, 45°]	[10°, 15°, 22.5°]
Argument of perigee, **ω**	0°	0°	0°
Starting true anomaly, $\boldsymbol{\nu_{on}}$	2°	2°	-15°
Ending true anomaly, $\boldsymbol{\nu_{off}}$	2°	2°	17.62°

Table 14: Input orbital parameters for 2 SBS platforms and RSO.

The **figure 42** shows which part of the RSO orbit the two sensors track. We decide to track the object for 600 seconds, corresponding to RSO delta true anomaly Δν of 32.62°. For simplicity, we put the RSO orbital plane in the middle of two sensors planes as shown in the figure.

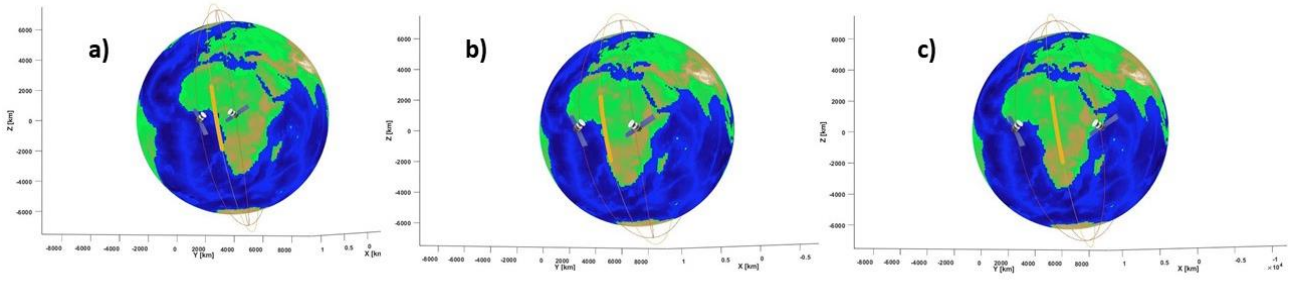

Figure 42: Scenario with RAAN separation: 20° (a), 30° (b), 45° (c)

The **figure 43** displays the results of the above uncertainty realism test procedure which can be interpreted as follows: The calculated degree of the CVM test and AMD metric are plotted for second of tracking. Until the first point of intersect from either realism test and the corresponding confidence interval, the uncertainty distribution can be assumed to represent the calculated RSO covariance matrix under the chosen level of confidence. A confidence level of 99% was chosen arbitrarily. The figure demonstrates that the CVM test statistic with the corresponding confidence interval provides a more restrictive statistical measure, when compared against the first-moment AMD metric. The **table 15** highlight the

difference of the tracking period available between the AMD metric and the CVM test. This is not a surprising result as the CVM test statistic is determined from the empirical CDF measurement model, giving more indication on the actual shape, size and orientation of the distribution. In turn the CVM test can distinguish finer discrepancies between the empirical (CDF) and the theoretical uncertainty distribution (covariance) when compared to the AMD metric

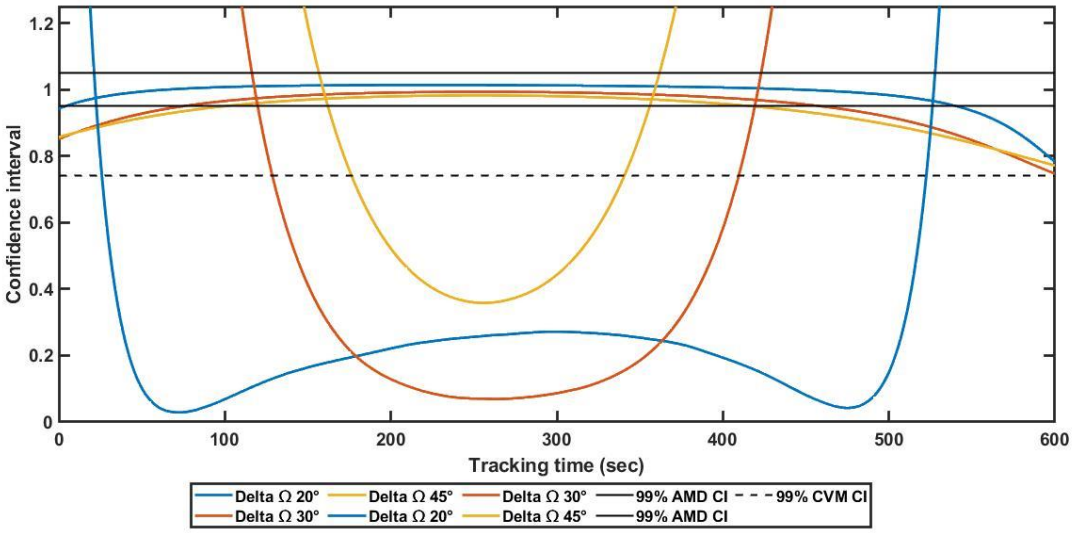

Figure 43: Covariance realism of theoretical uncertainty volume for Space-Based Optical Sensor

Orbital plane Separation angle (deg)	Tracking Period Available (sec)		Delta Tracking Time (sec)
	AMD Metric	*CVM Test*	
20°	537	496.7	40.3
30°	384	281	103
45°	317	165	152

Table 15: Tracking Time available for the three sub-case

The factors that influence these results can be mainly:

- the range to target, distance between the sensors and the object. For simplicity, we calculate the average range from the two sensors to the RSO, given by the equation:

$$Average\ Range = \frac{Range_1 + Range_2}{2} \tag{112}$$

- the separation angle, the angle measured from sensor one through the target object to sensor two.

The **figure 44** and **45** show the importance of the range and the separation angle for the RSO tracking by using optical sensors with the only-angles determination problem. It is clear that the Average Mahalanobis Distance metric and the Cramer von-Mises test values are acceptable, that means values inside of the interval determined by the 99% CVM Confidence Interval, when both average range and separation angle decrease their values. Due to the significant impact on the RSO relative position respect the two platforms, assessing the covariance

realism in relation to the specific range to target and separation angle provide a practical relationship to defining an acceptable magnitude of measurement errors.

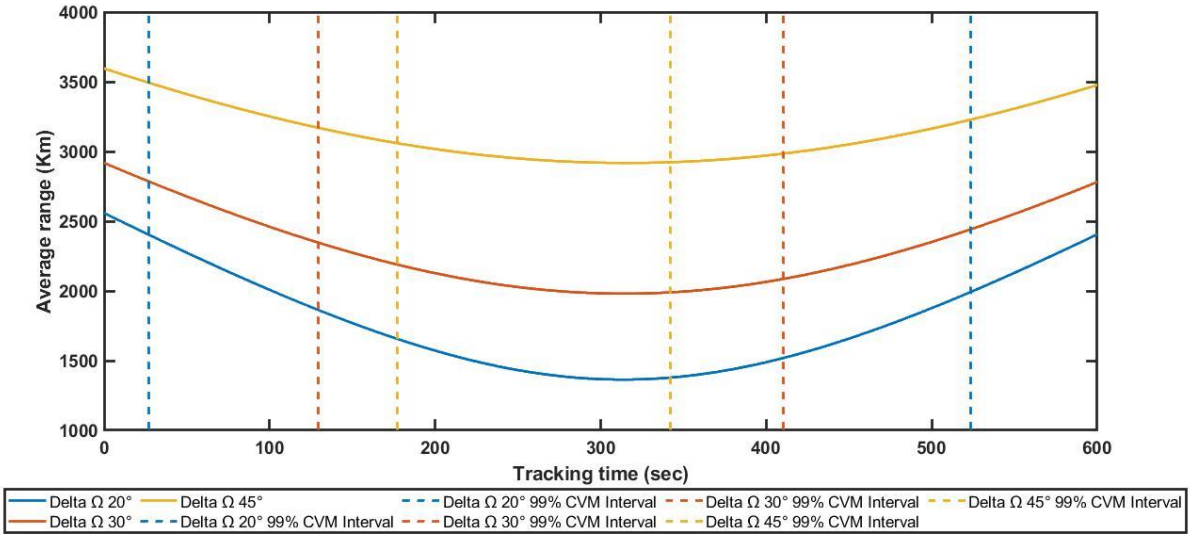

Figure 44: Average Distance from the sensor to RSO during tracking period

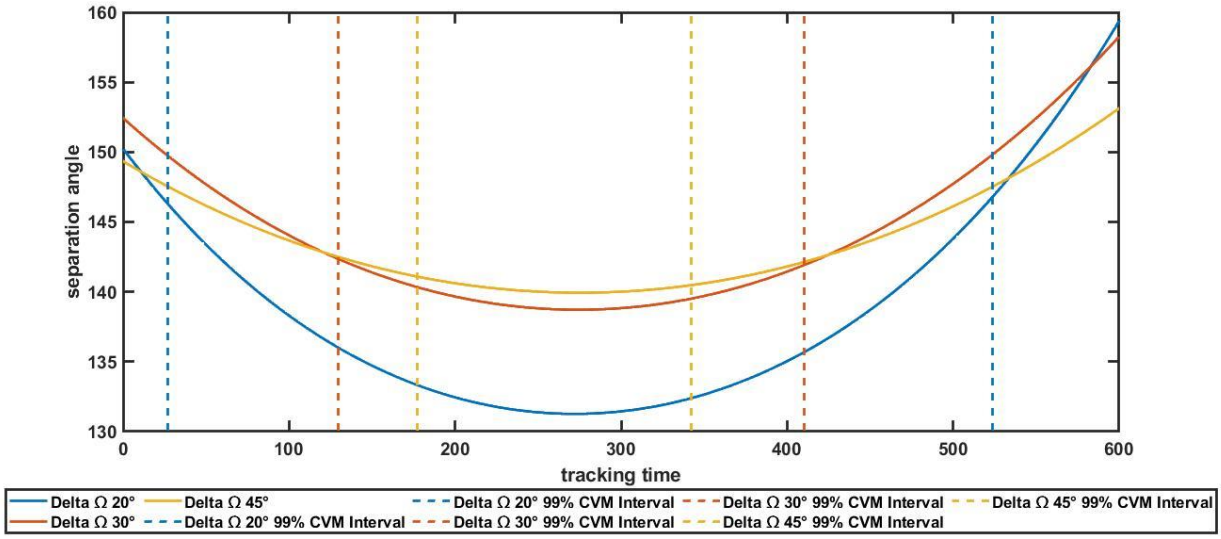

Figure 45: Separation angle during the tracking period

The **table 16** highlights the maximum values of separation angle and average range in which the ellipsoid generated by the covariance matrix can follow the Gaussian assumptions. It is evident that if the RAAN separation is bigger, the maximum separation angle value decreases.

RAAN Separation (deg)	Max Separation angle (deg)	Max Average Range (Km)
20°	146°	2408.7
30°	142°	2349
45°	141°	3061

Table 16: Maximum Separation angle and Maximum Average Range for 99% Average Mahalanobis Distance (AMD) and CVM Covariance Realism Test Statistic.

The last table confirms the results of the **table 15**, where we can outline that two optical sensor platforms with an orbital plane separation angle of 20° can represent the RSO uncertainty with an ellipsoid for 496 seconds against the 165 seconds of the third sub-case (45°).
The results underline a clear relationship between the separation angle and the covariance realism: angular values too high lead to have an ellipsoid that doesn't represent the Monte Carlo points generated by using a normal distribution for each measurement variables.
The considerations about the range to target are affected by the camera assumptions. A deeper analysis should be considered where the visual magnitude and the size of the RSO are two parameters.
Mathematically, the confidence interval represents the point at which the original distribution can no longer be truthfully represented as rectilinear covariance within the cartesian ECI system. The **figure 46** shows the generation of Monte Carlo points used to generate the empirical distribution for the RSO at the 99% CVM confidence interval. The calculated Cartesian covariance matrix inflated to 3 sigma is then overlaid as an ellipsoid centered about the nominal RSO position. As expected, the figure illustrates that the Monte Carlo points can represent the corresponding uncertainty in terms of covariance within the ECI cartesian frame

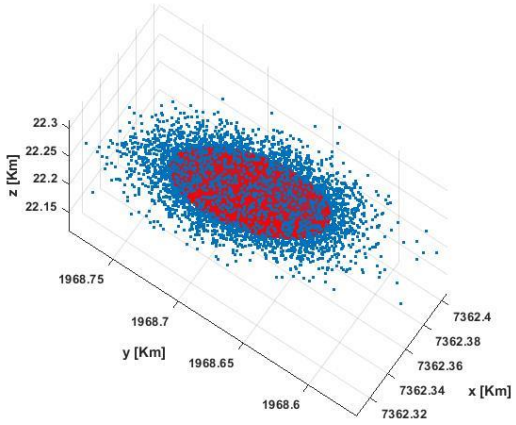

Figure 46: Montecarlo Generated distribution with 99% CVM CI and the relative ellipsoid

Conversely, the **figure 47** shows the generation of Monte Carlo points for the RSO outside the 99% CVM confidence interval. The calculated Cartesian covariance matrix inflated to 3 sigma is then overlaid as an ellipsoid centered about the nominal RSO position. It is interesting to note how the covariance matrix, represented by an ellipsoid, is not able to follow the orientation of the MC point distribution.

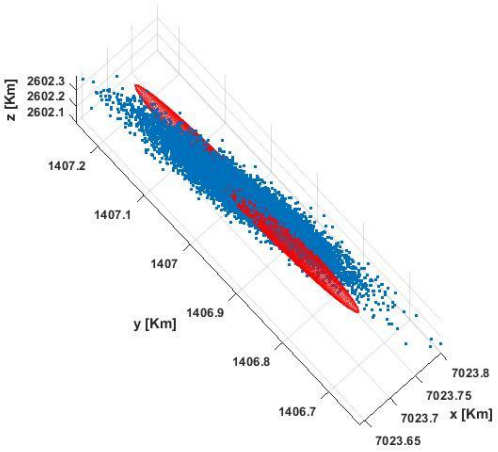

Figure 47: Montecarlo Generated distribution with 99% CVM CI and the relative ellipsoid

The stretched ellipsoid shown in **figure 47** is due to the increase of the separation angle and the range to target. This stretching of the shape has led the covariance matrix to lose information specially about the orientation and for this reason the discrepancy between the original distribution and the rectilinear covariance become evident.
Although this demonstrates the extreme case, meaning practically that the optical sensor would not be used under these conditions due to the high value of the separation angle, the figures aims to show physically what it means when the distribution becomes too stretched at the sensor level and therefore cannot be described in terms of cartesian covariance.

5.2.2 Second case

The second case would analyze how the altitude RSO orbit influence the sensor performance and then the quantification of the RSO uncertainty position.
The two Space-Based have a Sun-synchronous orbit. Orbiting in opposite direction and starting with a true anomaly of 160° and -20° respectively, they will cross the equatorial plane at the same moment. We decide to track the space debris for 700 seconds and thus the two SBSS will cover a $\Delta\nu$ of 41.70°. The RSO will have a fixed position with equatorial latitude. The **table 17** shows the orbital parameters of the two SBSS and the RSO. Moreover, for a deeper understanding, we change the altitude orbit of the RSO and thus the Semi-Major Axis, **a**. Therefore, the RSO orbit altitude will have 3 values: 850, 1000 and 1150 Km from the Earth surface.

Orbital Parameters	Sensor 1	Sensor 2	RSO
Semi-Major Axis, **a**	7171 Km	7171 Km	6371 + [850, 1000, 1150] Km
Eccentricity, **e**	0	0	0
Inclination, **i**	98.5621°	98.5621°	100°
Longitude of ascending node, **Ω**	180°	45°	22.5°
Argument of perigee, **ω**	0°	0°	0°
Starting true anomaly, $\boldsymbol{\nu_{on}}$	160°	-20°	0°
Ending true anomaly, $\boldsymbol{\nu_{off}}$	201.70°	21.70°	0°

Table 17: Input orbital parameters for 2 SBS Platforms and RSO

The **figure 48** shows a graphic representation of the scenario, where the black dot is the RSO position and the purple and green lines are respectively the orbits of the first and the second sensor platform. For simplicity, we decided to put the RSO position in the middle of two sensors planes.

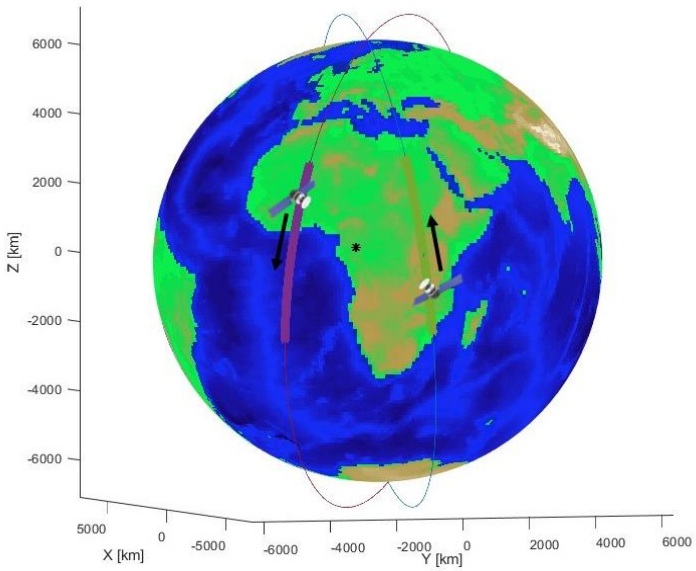

Figure 48: scenario with three RSO orbit altitudes: 850 Km, 1000 Km, 1150 Km

The **figure 49** displays the results of the above uncertainty realism test procedure which can be interpreted as follows: The calculated degree of the CVM test and AMD metric are plotted for each tracking second. Until the first point of intersect from either realism test and the corresponding confidence interval, the uncertainty distribution can be assumed to represent the calculated RSO covariance matrix under the chosen level of confidence. A confidence level of 99% was chosen arbitrarily. The figure demonstrates that the CVM test statistic with the corresponding confidence interval provides a more restrictive statistical measure, when compared against the first-moment AMD metric. The **table 18** highlight the difference of the tracking period available between the AMD metric and the CVM test. This is not a surprising result as the CVM test statistic is determined from the empirical CDF measurement model, giving more indication on the actual shape, size and orientation of the distribution. In turn the CVM test can distinguish finer discrepancies between the empirical (CDF) and the theoretical uncertainty distribution (covariance) when compared to the AMD metric

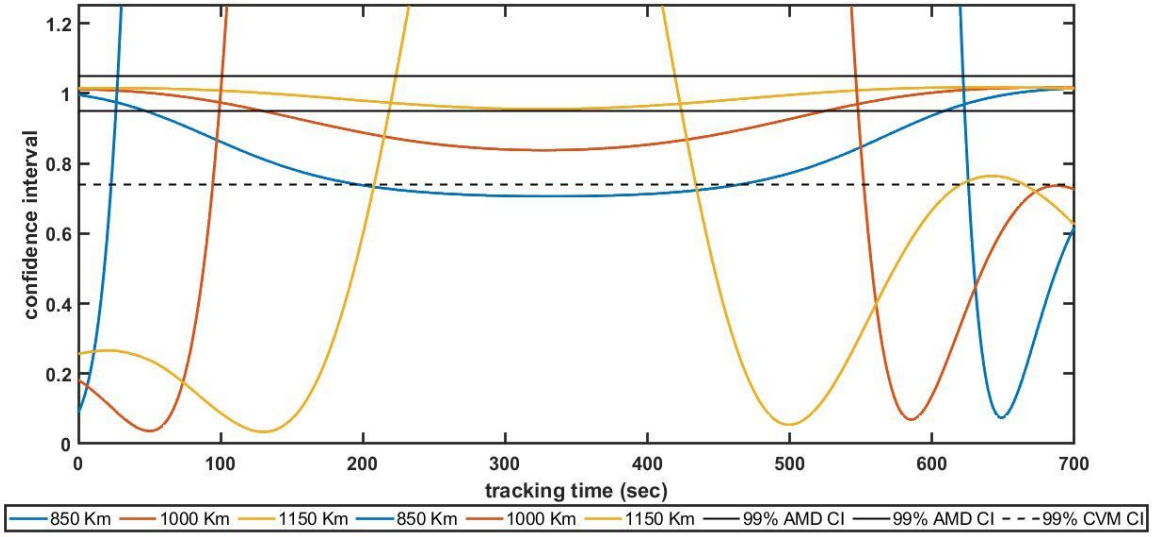

Figure 49: Covariance realism of theoretical uncertainty volume for Space-Based Optical Sensor

It is evident that for AMD metric the tracking period available is longer respect CVM test and this difference grows when the RSO orbit has a semi-major axis **a** bigger.

RSO Altitude (Km)	Tracking Period Available (sec)		Delta Tracking Period (sec)
	AMD Metric	*CVM Test*	
850	138	97.5	40.5
1000	304	242.5	61.5
1150	700	474.5	225.5

Table 18: Tracking Period available for 3 RSO altitude

As the previous case, the separation angle and the average range parameters, given by the **equation 112**, will be analyze. The **figures 50** and **51** underline the importance of these two factors that lead to restrict the field where the covariance matrix follows the Gaussian assumptions. It is clear that the Average Mahalanobis Distance metric and the Cramer von-

Mises test values become unacceptable, that means values inside of the interval determined by the 99% CVM Confidence Interval, when both average range and separation angle increase their values.

Figure 50: Average Distance between two sensors and the RSO during the tracking period

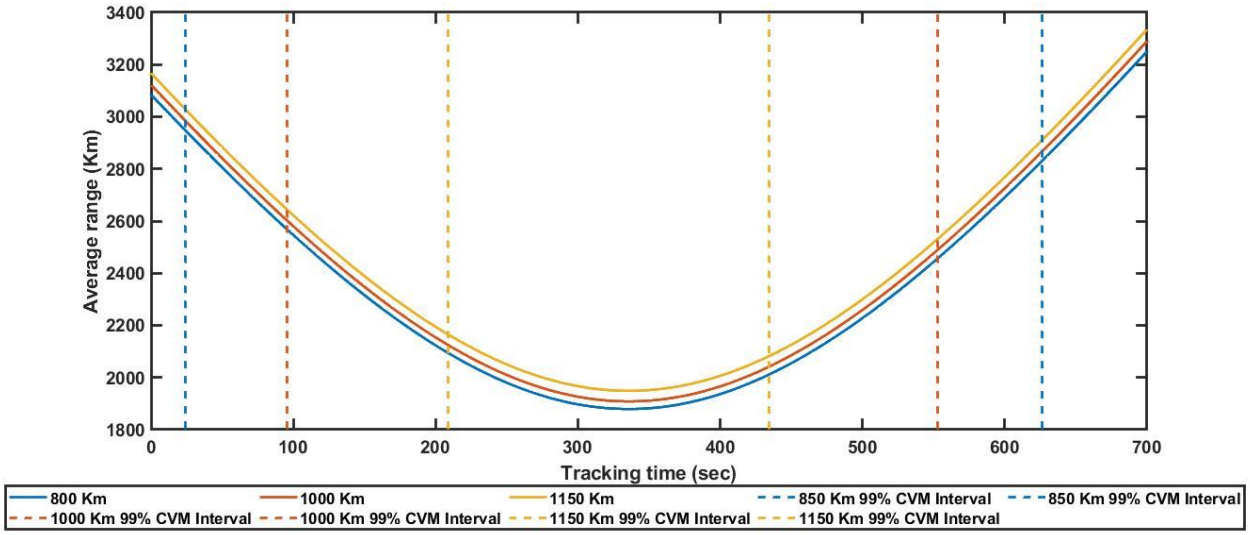

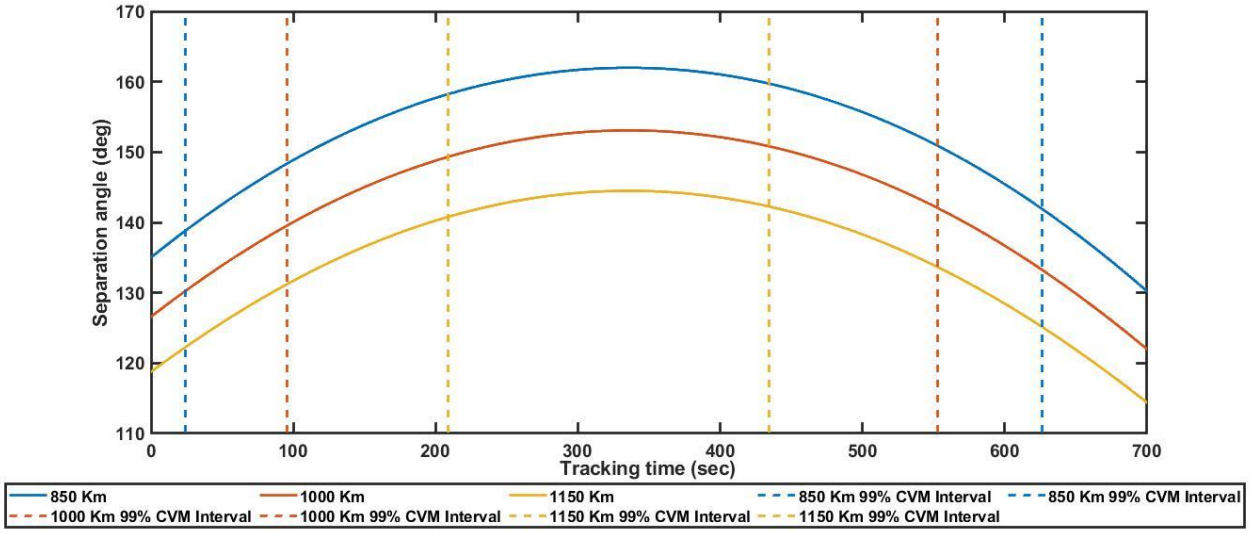

Figure 51: Separation angle during the tracking period

The **table 19** highlights the maximum values of separation angle and averaged range in which the ellipsoid generated by the covariance matrix can represent the RSO total uncertainty upholding the uncertainty realism assumptions. We can see that the maximum values of the separation angle for these three sub-cases are very similar, in fact the difference is only a few degrees. For the maximum average range, we outline a linear relationship with the RSO altitude but we can highlight the same consideration of the first case and a deeper analysis will be necessary.

RSO Altitude (Km)	Max Separation angle (deg)	Max Average Range (Km)
850	138.64°	2954
1000	139.36°	2607
1150	140.73°	2127

Table 19: Max Separation angle ad Average Range for 99% Average Mahalanobis Distance (AMD) and CVM Covariance Realism Test Statistic.

Mathematically, the confidence interval represents the point at which the original curvilinear distribution can no longer be truthfully represented as rectilinear covariance within the cartesian ECI system.

The **figure 52** shows the generation of Monte Carlo points used to generate the empirical distribution for the RSO at the 99% CVM confidence interval. The calculated Cartesian covariance matrix inflated to 3 sigma is then overlaid as an ellipsoid centered about the nominal RSO position. As expected, the figure illustrates that the Monte Carlo points can represent the corresponding uncertainty in terms of covariance within the ECI cartesian frame

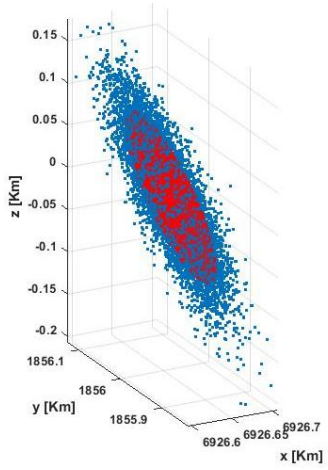

Figure 52: Montecarlo Generated distribution with 99% CVM CI and the relative ellipsoid

Conversely, the **figure 53** shows the generation of Monte Carlo points for the RSO outside the 99% CVM confidence interval. The calculated Cartesian covariance matrix inflated to 3 sigma is then overlaid as an ellipsoid centered about the nominal RSO position. It is interesting to note how the covariance matrix is not able to follow the orientation of the MC points.

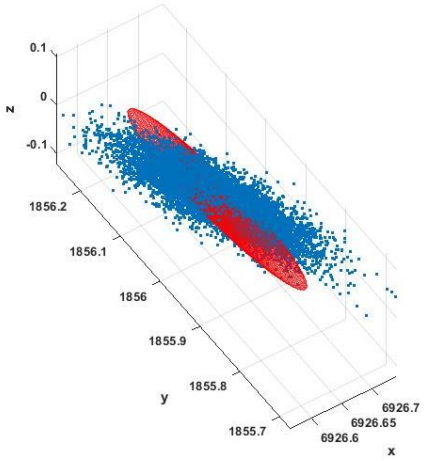

Figure 53: Montecarlo Generated distribution with 99% CVM CI and the relative ellipsoid

As the previous sub-case, the stretched ellipsoid shown in the figure is due to the increase of the separation angle and the range to target. This shape stretching has led the covariance matrix to lose information specially about the orientation and for this reason the discrepancy between the original distribution and the rectilinear covariance become evident.
As the previous sub-case, this means practically that the optical sensor would not be used under these conditions due to the high values of the separation angle and range to target leading the distribution to become too stretched.

6 Conclusions and Future Research

Ground and space-based surveillance platforms will form a necessary aspect in the categorization and maintenance of resident space object databases, required for timely and effective SSA operation within a future Space Traffic Management (STM) system. Nonetheless, for this to be a viable and useful asset, it is necessary that a sensor focused approach is taken when determining position uncertainty of Resident Space Objects (RSO). Through a representative case study of a Ground-Based and Space-Based by using both radar and passive optical sensors, this thesis aimed to demonstrate an error model that captures both the platform navigation and tracking sensor errors in determining RSO position uncertainty. Practically, the results show that sensor performance must be determined under different tracking conditions to uphold uncertainty realism assumptions and support key SSA decision-making processes.
The results of the research highlighted different type of limitations due to the nature of the sensor itself:

- the limitation of the radar system regards the curvilinear distribution described by the spherical uncertainty of the radar: when the range to target grows the distribution morphs from an ellipsoidal shape to a "bananoid" and becomes non-gaussian when mapping to a cartesian system. Therefore, the corresponding uncertainty cannot be represented in terms of covariance matrix (cartesian normal distribution)
- the passive optical system has the limitation of the separation angle: when the two sensor platforms form with the RSO a high separation angle, the generated ellipsoid starts to have a stretched shape and it cannot provide the information of the empirical distributions about the orientation, the shape and the size

Future research will focus on building a more rigorous description of RSO uncertainty through the inclusion of velocity measurement errors and associated uncertainty. This is a necessary to fully define the uncertainty of the RSO.
Further, deeper analysis of the constellation space-based optical platforms will be necessary to optimize the constellation in regarding to effectively reducing the uncertainty of RSO.
Uncertainty propagation is a key aspect of the SSA evolutions. A linear propagation method such as Linear Covariance (LinCov) analysis, that linearized the orbital dynamics, has been developed to estimate the propagation of RSO error over time. Thus, it is will be useful to analyze the complete covariance matrix (6x6), that includes the position and the velocity uncertainty, to fully understand how uncertainty grows and when covariance assumptions break down over the propagation period.
The addition of cooperative RSO scenario case studies also prove necessary due to the continuous increase of collision warnings involving operational spacecraft. This will require the modelling of RSO equipped with TSPI enabling systems such as GNSS and data sharing capabilities equivalent to Automatic Dependent Surveillance Broadcast (ASD-B) system

References

1. Hilton, S.; Sabatini, R.; Gardi, A.; Ogawa, H.; Teofilatto, P. Space traffic management: towards safe and unsegregated space transport operations. *Prog. Aerosp. Sci.* **2019**, *105*, 98–125.
2. Holzinger, M.; Jah, M. *Challenges and Potential in Space Domain Awareness*; American Institute of Aeronautics and Astronautics: Reston, VA, USA, 2018.
3. Sciré, G.; Santoni, F.; Piergentili, F. Analysis of orbit determination for space based optical space surveillance system. *Adv. Space Res.* **2015**, *56*, 421–428.
4. Hu, Y.-p.; Huang, J.-y.; Chen, L. Space-based visible observation strategy for beyond-LEO objects based on an equatorial LEO satellite with multi-sensors. *Adv. Space Res.* **2017**, *59*, 1751–1762.
5. Flohrer, T.; Krag, H.; Klinkrad, H.; Schildknecht, T. Feasibility of performing space surveillance tasks with a proposed space-based optical architecture. *Adv. Space Res.* **2011**, *47*, 1029–1042.
6. Davis, M. Technology challenges in affordable space-based radar. In Proceedings of the Record of the IEEE 2000 International Radar Conference [Cat. No. 00CH37037], Alexandria, VA, USA, 12–12 May 2000.
7. Davis, M. Space based radar moving target detection challenges. In Proceedings of the RADAR 2002, Edinburgh, UK, 15–17 October 2002.
8. Du, J.; Chen, J.; Li, B.; Sang, J. Tentative design of SBSS constellations for LEO debris catalog maintenance. *Acta Astronaut.* **2019**, *155*, 379–388.
9. Horwood, J.T.; Aristoff, J.M.; Singh, N.; Poore, A.B.; Hejduk, M.D. Beyond covariance realism: a new metric for uncertainty realism. In *Signal and Data Processing of Small Targets 2014*. International Society for Optics and Photonics: San Francisco, CA, USA, 2014.
10. Poore, A.B.; Aristoff, J.M.; Horwood, J.T.; Armellin, R.; Cerven, W.T.; Cheng, Y.; Cox, C.M.; Erwin, R.S.; Frisbee, J.H.; Hejduk, M.D.; et al. *Covariance and uncertainty realism in space surveillance and tracking*; Numerica Corporation Fort Collins United States: Fort Collins, CO, USA, 2016.
11. Luo, Y.-z.; Yang, Z. A review of uncertainty propagation in orbital mechanics. *Prog. Aerosp. Sci.* **2017**, *89*, 23–39.
12. Ramírez-Torres, M.; Ferreras, M.; Hernández, C.; García-de-la-Cueva, C.; Barba, M.; Perez-Palomino, G.; Encinar, J.A.; Sierra-Castañer, M.; Grajal, J.; Vázquez-Roy, J.L.; et al. Technological developments for a space-borne orbital debris radar at 94 GHz. In Proceedings of the 2018 IEEE Radar Conference (RadarConf18), Oklahoma City, OK, USA, 23–27 April 2018.
13. Delande, E.; Houssineau, J.; Jah, M. A New Representation of Uncertainty for Data Fusion in SSA Detection and Tracking Problems. In Proceedings of the 2018 21st International Conference on Information Fusion (FUSION), Cambridge, UK, 10–13 July 2018.
14. Delande, E.; Houssineau, J.; Jah, M. Physics and human-based information fusion for improved resident space object tracking. *Adv. Space Res.* **2018**, *62*, 1800–1812.
15. Pongsakornsathien, N.; Lim, Y.; Gardi, A.; Hilton, S.; Planke, L.; Sabatini, R.; Kistan, T.; Ezer, N. Sensor Networks for Aerospace Human-Machine Systems. *Sensors* **2019**, *19*, 3465.
16. Lim, Y.; Gardi, A.; Sabatini, R.; Ramasamy, S.; Kistan, T.; Ezer, N.; Vince, J.; Bolia, R. Avionics Human-Machine Interfaces and Interactions for Manned and Unmanned Aircraft. *Prog. Aerosp. Sci.* **2018**, *102*, 1–46.
17. Lim, Y.; Bassien-Capsa, V.; Ramasamy, S.; Liu, J.; Sabatini, R. Commercial airline single-pilot operations: System design and pathways to certification. *IEEE Aerosp. Electron. Syst. Mag.* **2017**, *32*, 4–21.
18. Liu, J.; Gardi, A.; Ramasamy, S.; Lim, Y.; Sabatini, R. Cognitive pilot-aircraft interface for single-pilot operations. *Knowl.-Based Syst.* **2016**, *112*, 37–53.
19. Liu, J.; Gardi, A.; Ramasamy, S.; Lim, Y.; Sabatini, R. Cognitive Human-Machine Interfaces and Interactions for Unmanned Aircraft. *J. Intell. Robot. Syst.* **2018**, *91*, 755–774.
20. Aleva, D.; McCracken, J. Jspoc cognitive task analysis. In Proceedings of the Advanced Maui Optical and Space Surveillance Technologies Conference, Wailea, Maui, HI, USA, 1–4 September 2009; AIR FORCE RESEARCH LAB WRIGHT-PATTERSON AFB, Dayton, OH, USA, 2009.
21. Ianni, J.D. Human-system interfaces for space cognitive awareness. In Proceedings of the Advanced Maui Optical and Space Surveillance Technologies Conference, Wailea, Maui, HI, USA, 17–19 September 2008; 711TH HUMAN EFFECTIVENESS DIRECTORATE WRIGHT-PATTERSON AFB, Dayton, OH, USA, 2008.
22. Andris,D. J.; Dev M.; Karen M. F.; Marcus J.H.; Moses W.C. *SSA Decision Support System Development and Evaluation Using Cognitive Systems Engineering*; CEC: Peabody, MA, USA, 2018.

23. Jenkins, M.; Catto, M.G.; Bird, M.L. Increased Space Situational Awareness through Augmented Reality Enhanced Common Operating Pictures. In Proceedings of the Advanced Maui Optical and Space Surveillance Technologies Conference, Wailea, Maui, HI, USA, 11–14 September 2018.
24. Ianni, J.D.; Aleva, D.L.; Ellis, S.A. Overview of human-centric space situational awareness science and technology. In Proceedings of the Advanced Maui Optical and Space Surveillance Technologies Conference, Wailea, Maui, Maui, HI, USA, 11–14 September 2012; 711TH HUMAN PERFORMANCE WING OF AIR FORCE RESEARCH LAB BASED AT Wright-Patterson AFB: Dayton, OH, USA, 2012.
25. Parasuraman, R.; Sheridan, T.B.; Wickens, C.D. A model for types and levels of human interaction with automation. *IEEE Trans. Syst. Man Cybern. Part A Syst. Hum.* **2000**, *30*, 286–297.
26. Stenbit, J.P.; Wells, L.; Alberts, D. *NATO Code of Best Practice for C2 Assessment*; OASD: Washington, DC, USA, 2002.
27. Barton, D.K. *Radar System Performance Modeling*; Artech House: Norwood, MA, USA, 2005; pp. 23–25.
28. Vallado, D.A. *Fundamentals of Astrodynamics and Applications*; Springer Science & Business Media: Berlin, Germany, 2001; Volume 12.
29. Woffinden, D.; Robinson, S.; Williams, J.; Putnam, Z.R. Linear Covariance Analysis Techniques to Generate Navigation and Sensor Requirements for the Safe and Precise Landing Integrated Capabilities Evolution (SPLICE) Project. In *AIAA Scitech 2019 Forum*; AIAA: San Diego, CA, USA, 2019.
30. Mahalanobis, P.C. *On the Generalized Distance in Statistics*; National Institute of Science of India: Bengaluru, India, 1936.
31. Chiaradia, A.P.M.; Kuga, H.K.; Prado, A.F.B.D.A. Comparison between two methods to calculate the transition matrix of orbit motion. In *Mathematical Problems in Engineering*; Hindawi Publishing Corporation: London, UK, 2012.
32. Chan, F.K. *Spacecraft Collision Probability*; Aerospace Press: El Segundo, CA, USA, 2008.
33. Vanicek, P.; Krakiwsky, E.J. *Geodesy: The Concepts*; Elsevier: Amsterdam, The Netherlands, 2015.
34. Mezian, M.; Vallet, B.; Soheilian, B.; Paparoditis, N. Uncertainty propagation for terrestrial mobile laser scanner. *Int. Arch. Photogramm. Remote Sens. Sp. Inf. Sci.* **2016**. *41*, 331–335.
35. Hauschild, A.; Markgraf, M.; Montenbruck, O.J.I.G. GPS receiver performance on board a LEO satellite. *Inside Gnss* **2014**, *9*, 47–57.
36. Liou, J.-C. (2016), The Orbital Debris Problem, Space Tech Conference.
37. Newman, L. K. (2016), NASA Conjunction Assessment Risk Analysis Approach, NASA robotic CARA.
38. G.D. Arndt,P.Fink,W.B.Warren,A space station-based orbital debris tracking system, Adv.SpaceRes.13 (8) (1993) 65–68.
39. M.Gruntman, Passive optical detection of submillimeter and millimeter size space debris in low Earth orbit, ActaAstronaut.105 (1) (2014) 156–170.
40. I.Ettouati, D.Mortari, T.Pollock, Space surveillance with star trackers. PartI: Simulations, 16th AAS/AIAA Space Flight Mechanics Meeting, Tampa, Florida, 2006, AAS06–231.
41. Allan, R. R., and G. E. Cook (1964), The Long-Period Motion of the Plane of a Distant Circular Orbit, Proceedings of the Royal Society of London Series A, 280,
42. Lee, B.-S., and B.-Y. K. Yoola Hwang, Hae-Yeon Kim (2012), Geo satellite collision avoidance maneuver strategy against inclined gso satellite.
43. Council, N. R., et al. (2011), Limiting future collision risk to spacecraft: An assess-ment of nasa's meteoroid and orbital debris programs.
44. Stoll, E., B. D'Souza, B. B. Virgili, K. Merz, and H. Krag (2013), Operational collision avoidance of small satellite missions, in Aerospace Conference, 2013 IEEE,
45. Aida, S., M. Kirschner, and F. Meissner (2015), Collision risk assessment and mitigation strategy for the GSoC geo satellites.
46. J. Utzmann and A. Wagner, "SBSS Demonstrator: a Space-based Telescope for Space Surveillance and Tracking," ed.
47. L. Felicetti, M.R. Emami, A multi-spacecraft formation approach to space debris surveillance, Acta Astronautica 127 (2016) 491–504.
48. X. Vanwijck, T. Flohrer, Possible Contribution of Space-based Assets for Space Situational Awareness vol. 4, (01 2008), pp. 2466–2472.
49. M. Gruntman, Passive optical detection of submillimeter and millimeter size space debris in low Earth orbit, Acta Astronautica 105 (1) (2014) 156–170.
50. J. Utzmann, et al., Space-based Space Surveillance and Tracking Demonstrator: Mission and System Design, (2014).
51. Tim Flohrer, Holger Krag, Space Surveillance and Tracking in ESA's SSA programme
52. Y.-z. Luo, Z. Yang, A review of uncertainty propagation in orbital mechanics, Prog.Aero. Sci. 89 (2017) 23–39.

53. S. Ramasamy, R. Sabatini, and A. Gardi, "A unified analytical framework for aircraft separation assurance and UAS sense-and-avoid," Journal of Intelligent & Robotic Systems, pp. 1-20.
54. Y. Sun, M. Kumar, Uncertainty propagation in orbital mechanics via tensor decomposition, Celestial Mechanics and Dynamical Astronomy 124 (3) (2016) 269–294.
55. A. Gelb, Applied Optimal Estimation, MIT press, 1974.
56. A. Gelb, R.S. Warren, Direct statistical analysis of nonlinear systems: CADET, AIAA Journal 11 (5) (1973) 689–694.
57. S.V. Kuzin, A.S. Ulyanov, S.V. Shestov, S.A. Bogachev, G.F. Karabadzhak, Space Object Observation Using Optical Sensors within the SPIRIT/CORONAS-F and TESIS/CORONAS-Photon Experiments
58. T.C.O. Brown, M. Gleason, M. Hallax, A. Long, E. Rivera, D. Finkleman, T. Hitchens, M. Jah, D. Koplow, R. Sedwick, Orbital Traffic Management Study: Final Report, (2016).
59. P.B. Larsen, Space traffic management standards, Journal of Air Law and Commerce 83 (2) (2018) 359.
60. I.-A.S.D.C. Committee, IADC-02-01 Revision, IADC Space Debris Mitigation Guidelines vol. 1, (2007).
61. D.J. Kessler, N.L. Johnson, J.C. Liou, M. Matney, The kessler syndrome: implications to future space operations, Advances in the Astronautical Sciences 137 (8) (2010).
62. D.J. Kessler, Orbital debris environment for spacecraft in low earth orbit, Journal of spacecraft and rockets 28 (3) (1991) 347–351.
63. Stefan Thorsteinson, Space Surveillance from a microsatellite, metric observation processing from NEOSSat
64. Shuang Wang, Yunhai Geng and Rongyu Jin, A Novel Error Model of Optical Systems and an On-Orbit Calibration Method for Star Sensors
65. John N. Sanders-Reed Impact of tracking system knowledge on multi-sensor 3D triangulation
66. Howard Curtis, Orbital Mechanics for Engineering Students, Elsevier Aerospace Engineering Series
67. L.Felicetti, M. Reza Emami, Spacecraft formation for debris surveillance
68. Brown, D.C. Decentering Distortion of Lens. Photogramm. Eng. Remote Sens. **1966**, 32, 444–462.
69. Michael Schlegel, Predicting the Accuracy of Optical Tracking Systems
70. M. Tuchin, A. Biryukov, M. Nikckiforov, M. Prokhorov, A. Zakharov, On Random and Systematic Errors of a Star Tracker
71. Francesco Villa, Feasibility study of an innovative surveillance system for space debris observations in LEO based on optical telescopes
72. S. Hilton, F. Cairola, A. Gardi, R. Sabatini, N. Pongsakornsathien, N. Ezer, Uncertainty Quantification for Space Situational Awareness and Traffic Management. MDPI Sensors. October 2019
73. S. Hilton, F. Cairola, A. Gardi, R. Sabatini, A Sensor-Centric Approach to Space Traffic Management. 2019 IEEE 6th International Workshop on Metrology for AeroSpace (MetroAeroSpace). June 2019